Robust optimization in 4D treatment planning for carbon ion therapy of lung tumors

Robuste Optimierung in der 4D Bestrahlungsplanung für die Kohlenstofftherapie von Lungentumoren
Zur Erlangung des Grades eines Doktors der Naturwissenschaften (Dr. rer. nat.)
genehmigte Dissertation von Moritz Ernst Wolf, M.Sc. Physik aus Dieburg, Deutschland
Darmstadt, Januar 2019 — D 17
Fachbereich Physik

1. Gutachten: Prof. Dr. Marco Durante
2. Gutachten: Prof. Dr. Christoph Bert

TECHNISCHE
UNIVERSITÄT
DARMSTADT

Robust optimization in 4D treatment planning for carbon ion therapy of lung tumors
Robuste Optimierung in der 4D Bestrahlungsplanung für die Kohlenstofftherapie von Lungentumoren

Genehmigte Dissertation von Moritz Ernst Wolf, M.Sc. Physik aus Dieburg, Deutschland

1. Gutachten: Prof. Dr. Marco Durante
2. Gutachten: Prof. Dr. Christoph Bert

Tag der Einreichung: 13. November 2018
Tag der Prüfung: 17. December 2018

Darmstadt — D 17

Bitte zitieren Sie dieses Dokument als:
URN: urn:nbn:de:tuda-tuprints-83540
URL: http://tuprints.ulb.tu-darmstadt.de/8354

Dedicated to my father Norbert

Abstract

Particle therapy (PT) with scanned carbon ions has been shown to improve the treatment of stage IV lung cancer patients through reduced dose exposure of critical organs. In order to maximize this effect, the application of intensity modulated particle therapy (IMPT) is needed. However, PT is particularly susceptible to internal dose gradients due to its range dependence. This challenge is exacerbated in the presence of organ motion. Both, motion and internal dose gradients, can be addressed by dedicated robust 4D optimization strategies. In addition, as IMPT needs congruent target volumes, only robust 4D optimization can incorporate field-specific range uncertainties and motion-induced range changes. Hence, a 'worst-case' method was implemented into GSI's in-house treatment planning system TRiP4D and adapted for different 4D optimization strategies, accounting for setup and range uncertainties.

The uncertainty scenarios of robust optimization increase the required computer memory, especially when also motion states are explicitly considered, as for robust 4D ITV optimization. Several strategies to reduce problem size and to increase the computation speed were implemented and tested, such as splitting the optimization matrix by dose contribution or randomized voxel subsampling.

Plan robustness was tested by performing robustness analysis, where dose distributions were calculated for a variety of uncertainty scenarios. By creating the superposition of patient setup errors with particle range changes, uncertainty scenarios beyond the ones already used in the optimization were tested. In a patient study with 8 complex lung cancer patients, it was possible to increase plan robustness in the majority of patients using robust optimization.

For conventional optimization, especially the dose volume exposure of the smaller airways (SA) became a limiting factor. Using the same 4D ITV planning strategy but with robust optimization enabled the OAR constraint for the SA to be fulfilled in 98.8 % of the cases, up from 79.8 % for conventional optimization. It is to note, that this increase in robustness could mean sacrificing target coverage in some patients.

Furthermore, a robust implementation of conformal 4D optimization was developed, based on a library of treatment plans for each motion phase of a 4DCT. The reduction of irradiated volume considerably improved OAR exposure, but increased the need for robust optimization even further in order to maintain robustness against deviations of the delivered dose distribution from the planned dose distribution.

For a lung cancer patient with large tumor motion, the robust conformal 4D optimization method could be shown to generate treatment plans with increased robustness against range and setup errors. As a result of the increased robustness, target coverage could be increased and dose exposure to the OARs could be decreased at the same time.

In conclusion, both robust optimization methods for 4D treatment planning in PT yield promising results, generating new options for robust, safe intensity modulated particle therapy and thus beneficial treatment plans for lung cancer patients.

Zusammenfassung

Die Partikeltherapie (PT) mit gescannten Kohlenstoffionen könnte die Behandlung von Patienten mit Lungenkrebs im Stadium IV verbessern, indem die Dosisbelastung kritischer Organe reduziert wird. Vorzugsweise wird hierbei die intensitätsmodulierten Partikeltherapie (IMPT) eingesetzt. PT ist aber wegen ihrer Reichweitenabhängigkeit besonders anfällig für interne Dosisgradienten, insbesondere wenn sich die betroffenen Organe bewegen.

Sowohl bewegungsinduzierte als auch interne Dosisgradienten können durch entsprechend robuste 4D-Optimierungsstrategien kontrolliert werden. Da IMPT kongruente Zielvolumina benötigt, können nur mittels robuster 4D-Optimierung feldspezifische Reichweitenunsicherheiten und bewegungsinduzierte Reichweitenänderungen simultan berücksichtigt werden. Daher wurde in das GSI-eigene Bestrahlungsplanungssystem TRiP4D eine "Worst-Case"-Methode, welche Fehler in der Patientenpositionierung und Reichweitenunsicherheiten berücksichtigen kann, implementiert und an verschiedene 4D-Optimierungsstrategien angepasst. Die Unsicherheitsszenarien der robusten Optimierung erhöhen den Bedarf an Arbeitsspeicher, insbesondere wenn auch Bewegungszustände explizit berücksichtigt werden, wie bei der robusten 4D ITV-Optimierung. Mehrere Strategien zur Reduzierung von Problemgröße und Rechenzeit wurden implementiert und getestet, wie z.B. das Aufteilen der Optimierungsmatrix nach Dosisbeitrag oder randomisierte Reduzierung der in der Optimierung verwendeten Voxel.

Die Pläne wurden einer Robustheitsanalyse unterzogen, bei der Dosisverteilungen für eine Vielzahl von Unsicherheitsszenarien berechnet wurden. Durch die Überlagerung von Positionierungs- und Reichweitenfehlern wurden Szenarien getestet, die über die bereits in der Optimierung verwendeten hinausgehen. In einer Studie mit 8 komplexen Lungenkrebspatienten konnte die Planrobustheit bei der Mehrheit der Patienten durch robuste Optimierung erhöht werden. Für die konventionelle Optimierung war insbesondere die Volumendosis der kleineren Atemwege ein limitierender Faktor. Mittels robuster 4D ITV-Optimierung konnte die Vorgabe für die kleineren Atemwege in 98.8 % der Fälle erfüllt werden, gegenüber 79.8 % bei konventioneller Optimierung. Diese verstärkte Robustheit führte bei einigen Patienten zu einem Verlust der Zielabdeckung.

Weiterhin wurde eine robuste Implementierung der konformen 4D-Optimierung entwickelt, die auf einer Bibliothek von Behandlungsplänen für jede Phase eines 4DCTs basiert. Dieses Verfahren reduziert das bestrahlte Volumen erheblich, erhöht aber auch die Notwendigkeit einer robusten Optimierung, um weiterhin die Robustheit gegenüber Abweichungen der abgestrahlten von der geplanten Dosisverteilung gewährleisten zu können. Für einen Lungenkrebspatienten mit großer Tumorbewegung konnte mittels robuster konformer 4D-Optimierung die Zielabdeckung deutlich erhöht und gleichzeitig die Dosisbelastung kritischer Organe reduziert werden.

Zusammenfassend lässt sich sagen, dass beide robusten Optimierungsmethoden für PT mit 4D-Behandlungsplanung vielversprechende Ergebnisse liefern und neue Optionen für eine robuste, sichere intensitätsmodulierte Partikeltherapie und damit vorteilhafte Behandlungspläne für Lungenkrebspatienten schaffen.

Contents

List of Abbreviations

4DCT	time resolved computed tomography
4DTP	4D treatment planning
AP	anterior-posterior
BED	biological effective dose
BEV	beam's eye view
CNAO	National Center of Oncological Hadrontherapy, Pavia, Italy
CT	computed tomography
CTV	clinical target volume
$D_{50\%}$	minimum dose delivered to 50% of volume
$D_{99\%}$	minimum dose delivered to 99% of volume
D_{Max}	maximum dose delivered to a single voxel
DIR	deformable image registration
DIC	dynamic intensity control
DNA	deoxyribonucleic acid
DS	dose spread
DSim	dose delivery simulation
DSB	double strand breaks
DVH	dose volume histogram
FC	Champalimaud Center for the Unknown
FDC	field dose correlation
FWHM	full width at half maximum
GSI	GSI Helmholtzzentrum für Schwerionenforschung GmbH
GTV	gross tumor volume
HC	hard constraint
HI	homogeneity index
HIMAC	Heavy Ion Medical Accelerator
HIT	Heidelberg Ion-Beam Therapy Center
HU	Hounsfield unit
HLUT	Hounsfield unit lookup table
ICRU	International Commission on Radiation Units and Measurements
IES	iso-energy slice
IMPT	intensity modulated particle therapy
IMRT	intensity modulated radiotherapy
ITV	internal target volume
LBL	Lawrence Berkeley Laboratory
LEM	local effect model
LET	linear energy transfer
LR	left-right
MDW	maximum dose weight
MFO	multiple field optimization
MIT	Marburg Ion-Beam Therapy Center
NIRS	National Institute of Radiological Sciences, Chiba, Japan
NSCLC	non-small cell lung cancer
OAR	organs at risk
PMMA	polymethyl methacrylate
PSI	Paul Scherrer Institut
PTV	planning target volume
RA	robustness analysis
RST	raster grid
RBE	relative biological effectiveness
SA	smaller airways
SI	superior-inferior
SBRT	stereo-tactic body radiation therapy
SFUD	single field uniform dose
SCLC	small cell lung cancer
SOBP	spread out Bragg peak
SSB	single strand break
TCS	treatment control system
TPS	treatment planning system
TP	treatment planning
VMAT	volumetric modulated arc therapy
WEPL	water equivalent path length

Motivation

As reported in a recent German national cancer report “Krebs in Deutschland”, about 19 300 women and 34 500 men were diagnosed with lung cancer in 2013–2014. Mortality rates for the same period were reported to be 15 524 for women and 29 560 for men [Kaatsch et al., 2017]. At a 5-year survival rate of 15 % for males and 20 % for females, lung cancer prognosis remains unfavorable (data collected in Germany between 2013–2014 [Kaatsch et al., 2017]). More than half of these patients are not detected until later stages, most commonly at stage IV, with non-small cell lung cancer (NSCLC) [Ramalingam and Belani, 2008; Iyengar et al., 2014]. Since the rapidly growing and early metastasizing small cell lung cancer (SCLC) is primarily treated chemotherapeutically [Kumar et al., 2004; Renz-Polster and Krautzig, 2008], the focus of this study is on NSCLC.

Several studies have shown that a dose escalation can significantly improve local tumor control rates, in particular for NSCLC [Rosenzweig et al., 2005; Kong et al., 2005]. The occurrence of radiation-induced normal tissue complications also depends significantly on the doses delivered to organs at risk (OAR). For example, the probability for radiation side effects, such as acute esophagus toxicity increases significantly depending on the esophagus volume receiving more than 35 Gy [Belderbos et al., 2005]. The choice of the radiotherapy protocol used also effects treatment outcome, where in particular the use of stereo-tactic body radiation therapy (SBRT) has shown promising results for the treatment of early stage NSCLC [Baumann et al., 2001; Fakiris et al., 2009; Grutters et al., 2010; Greco et al., 2011]. In the majority of photon treatments, a high number of irradiation fields is necessary to provide sufficient target coverage of deep seated tumors, while keeping normal tissue toxicity in the entrance channels on an acceptable level. Considering that the absorbed photon dose is exponentially decreasing with penetration depth, this comes at the cost of larger volume of surrounding tissue exposed with dose.

Ion therapy provides a promising solution for reducing doses to surrounding tissue. For these high-dose applications, the beneficial depth dose profile of ion beams delivers low doses along the radiological path and the majority of dose at the desired penetration depth. This is possible due to the “inverse” depth dose profile with its distinctive Bragg peak, produced by fast charged particles decelerated in matter. Anderle et al. have performed an in-silico comparative study for SBRT versus rescanned 4D optimized carbon ion therapy showing promising results [Anderle et al., 2016, 2018]. For the majority of patients, the target coverage was similar compared to SBRT while the OAR dose exposure was significantly reduced.

Compared to photons, scanned delivery of ion beams is much more sensitive to patient motion [Bert et al., 2008]. The interference of the respiratory motion and the scanning of the pencil beam can lead to interplay patterns, generating hot and cold spots within the planned dose distribution of the tumor volume. The treatment of moving lung tumors with ion beams is, in particular, susceptible to motion induced errors in delivery. One of the major issues is the large difference in density between the solid lung tumor and the surrounding lung tissue with lower density, which could result in significant volumes of dose delivered to healthy lung tissue, if the tumor is missed. To avoid high doses to normal tissue, especially if a treatment aims for high single fractionated target doses, motion mitigation strategies must be implemented to ensure accurate dose delivery.

In addition to dose deteriorations induced by respiratory motion, further decrease of dose coverage can be caused by imprecise patient positioning or range uncertainties. The latter two can lead to a mismatch of internal dose gradients between treatment fields, in particular when intensity modulated particle therapy (IMPT) is used. For the treatment of static targets with protons, robust optimization approaches have been successfully developed to incorporate these uncertainties in patient positioning and particle ranges during treatment planning [Unkelbach et al., 2007, 2009; Pflugfelder et al., 2008; Fredriksson et al., 2011; Liu et al., 2012]. The majority of robust approaches include 9 scenarios into the optimization: besides a nominal case, typically two range uncertainty scenarios are introduced, accounting for under- and overshoots of the particles, next to 6 scenarios considering shifts of the patient's iso center. Eventually, the resulting treatment plan is optimal for several scenarios at the same time. However, this could mean a deliberate decrease of plan quality for the nominal case.

In this study, the topic of robust optimization is investigated for treatment planning for moving targets with carbon ions. Basically, the presented robust methods are an adaption of 3D robust optimization for the use in time resolved plan optimization strategies, e.g. 4D optimization [Graeff, 2014]. This optimization method makes use of the information about temporal changes in patient anatomy provided by a 4D computed tomography (CT). The implementation of the robust 3D optimization algorithm into the in-house treatment planning system is described in chapter 2.

The robust 4D treatment planning is tested on a set of 8 complex lung cancer patients with multiple targets, which have been investigated by Anderle et al. using 4D optimization with rescanning [Anderle et al., 2018]. The resulting robust plans are then compared with the carbon plans from Anderle et al.. To provide a high degree of comparability, the planning study presented in this thesis uses the same planning parameters like in the study of Anderle et al., e.g. number of treatment fields, couch and gantry angles, etc. The major quantities under consideration are target dose coverage and OAR dose exposure. In contrast to [Anderle et al., 2018], these quantities are not only investigated for the nominal case but for a variety of uncertainty scenarios, which are summarized in a robustness analysis. This analysis gives deep insight about the plan quality under influence of different patient geometry between the stage of planning and treatment. The major part of this thesis is dedicated to the investigation of this robust 4D ITV method due to its high clinical relevance. The primary hypothesis of the presented study is, that using robust optimization further increases OAR sparing while keeping sufficient target coverage in the majority of considered uncertainty scenarios. As the implementation at centers like Heidelberg or Marburg would require primarily changes to the treatment planning software, the described method could be potentially used in a clinical environment in the near future.

Finally, a conformal 4D optimized treatment plan is presented for a selected patient. The conformal 4D optimization creates a library of treatment plans for each motion phase of a 4DCT, minimizing the normal tissue dose since only small safety margins are necessary for sufficient dose coverage. Though, a fast real-time motion detection and a dedicated treatment control system is necessary for synchronization of the treatment delivery to the respiratory motion of the patient. So far, this system has been only tested experimentally in promising dosimetric experiments at GSI. However, this system has the potential to improve carbon ion treatment in particular in combination with robustly optimized treatment plans.

1 Introduction - Research background and fundamentals

Contents

This chapter gives an introduction into the research background of this thesis. At first, an overview about lung cancer in general is given in section 1.1.1. Section 1.2 briefly presents the history of radiotherapy. In more detail, the mechanics behind the dose deposition of ionizing radiation are stated in section 1.3, followed by a description of the biological effects caused by radiation. Section 1.5 described the most common accelerators for particle therapy and the difference between passive and active delivery of treatment. Section 1.6 describes the fundamentals for treatment planning for scanned ions, also looking at patient motion (section 1.6.4), its implications (section 1.6.6) and mitigation strategies (section 1.6.7). Also the topic of 4D treatment planning (section 1.6.8) and image registration (section 1.6.9) is addressed.

With the information presented here, the reader should be equipped with sufficient knowledge for understanding the concepts and results in this work.

1.1 Lung cancer

As defined in [Renz-Polster and Krautzig, 2008] lung cancer, also called bronchial carcinoma, is a malignant lung tumor originating from the bronchial epithelium. Currently, about 19 300 women and 34 500 men are diagnosed with lung cancer annually. Further, current annual mortality rates stand at 15 524 women and 29 560 men [Kaatsch et al., 2017, p. 56–59]. at the beginning of the 20th century, the bronchial carcinoma was considered one of the rarest forms of cancer. Today it is the most frequent malign tumor: Lung cancers represent about 25 % of all cancer deaths. Currently, men are inflicted with bronchial carcinoma more frequently than women. However, since 1999, incidence rates are rising in Germany's female population (see figure 1.1). This can be correlated to the recently rising numbers of female smokers [Renz-Polster and Krautzig, 2008].

At a relative 5-year survival rate of 15 % for males and 20 % for females, lung cancer prognosis remains to be unfavorable (data collected in Germany between 2013–2014 [Kaatsch et al., 2017]).

1.1.1 Risk factors

The greatest risk factor for lung cancer is tobacco smoke [Kaatsch et al., 2017]. For males 90 % and for females at least 60 % of lung cancer diagnoses can be traced back to active and regular smoking. Also inhalation of second hand smoke increases the risk for lung cancer.

In the USA, the capita cigarette consumption from the beginning of the 20th century to the mid 2000's coincides with the male lung cancer incidence rates [MMWR, 2005; AACR, 2012]. The two graphs in figure 1.2 show a lag of about 20 to 30 years between the rise of the cigarette consumption and the cancer incidents. Following widespread US policy action against raising numbers of smokers within the population, such as banning tobacco advertisements from broadcast in 1971 [Warner and Goldenhar, 1989], it took almost 20 years for the lung cancer rates to begin to decline.

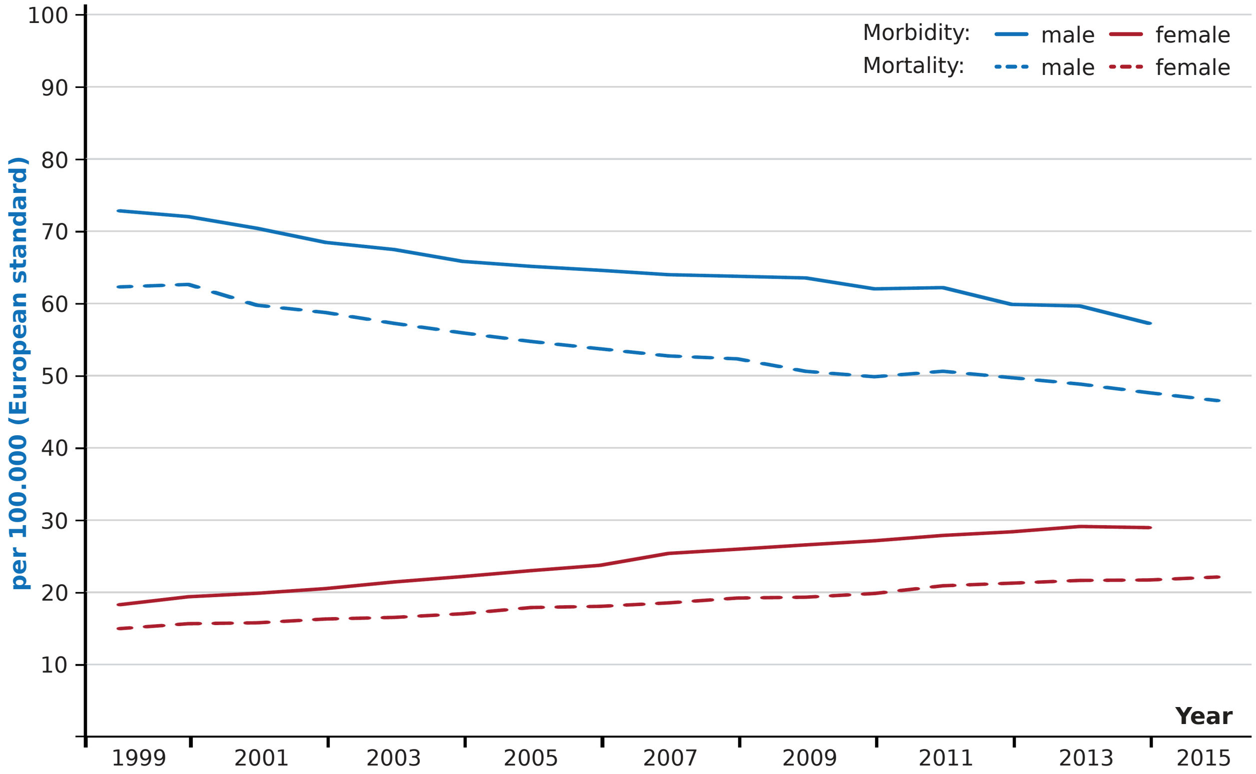

Figure 1.1.: Age standardized morbidity and mortality by gender for Germany 1999–2014/2015. Figure adapted from [Kaatsch et al., 2017].

The effects of common pollution are also contributing to the overall lung cancer risk, although they are less relevant compared to tobacco smoke. Nonetheless, about 15 % of patients suffering from bronchial carcinoma are non-smokers. Cancerogenic substances like asbestos, polycyclic aromatic hydrocarbons, quartz and nickel dust have caused about 9 % to 15 % of lung cancer incidents in Germany [Kaatsch et al., 2017]. The exposure to radioactive substances such as natural radon gas also increases the risk for lung cancer [Renz-Polster and Krautzig, 2008]. This is especially hazardous in basement levels of buildings in areas with naturally high radon concentrations. Ongoing investigations are studying the influence of pollution with fine dust like particles with grain sizes smaller $10\,\mu$m. Such particles originate from transportation vehicles (combustion of diesel fuel, particles from tire and brake wear), power plants, heating systems and industrial production. Due to their small size, the particles can sediment on the mucosal tissue of the bronchial apparatus or even in the alveoli causing local inflammation. Over time, this can lead to bronchitis or chronic coughing which encourages the development of bronchial carcinoma [Renz-Polster and Krautzig, 2008].

1.1.2 Non-small cell lung cancer (NSCLC)

Since the rapidly growing and early metastasizing small cell lung cancer (SCLC) is primarily treated with chemotherapy only [Kumar et al., 2004; Renz-Polster and Krautzig, 2008], the focus of this study is on non-small cell lung cancer (NSCLC), which is primarily treated by surgery and subsequent chemotherapy and radiotherapy, if the tumor is inoperable. NSCLC divides in four main stages I–IV with subdivisions

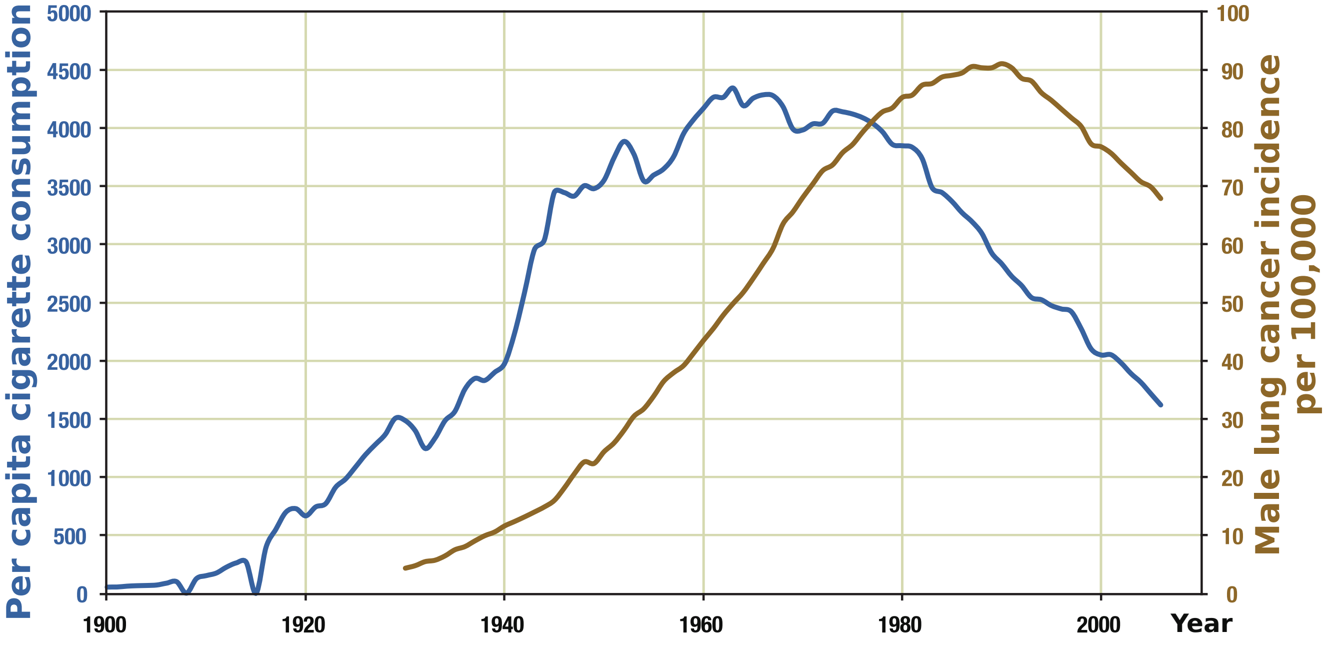

Figure 1.2.: Correlation between per capita cigarette consumption and male lung cancer incidents from 1900–1999. Figure adapted from [AACR, 2012], cigarette consumption data from [MMWR, 2005].

(Ia/b, IIa/b, IIIa/b/c and IVa/b) [Goldstraw et al., 2016]. Table 1.1 showing the 5-year survival rates by staging, emphasizes the poor prognosis for NSCLC, especially for stages III and IV. The categorization depends on the size and number of lung tumors, the affection of lymph nodes as well as the occurrence of metastasis outside of the lung (TNM staging).

Table 1.1.: 5-year survival rates of NSCLC patients by staging from worldwide data between 1999–2010 [ACS, 2017; Goldstraw et al., 2016].

Clinical stage	5-year survival in [%]
Ia1	92
Ia2	83
Ia3	77
Ib	68
IIa	60
IIb	53
IIIa	36
IIIb	26
IIIc	13
IVa	10
IVb	1

Figure 1.3 is an example of NSCLC stages Ia/b and IV. Stage Ia and Ib are primarily distinguished by lesion size, whereas IV is distinguished by occurrence of metastases, lesions in the lining of lung or heart or lesions in both lungs. In this thesis, the term of stage IV will primarily refer to the occurrence of lesions in both lungs, which will be called multiple targets further on.

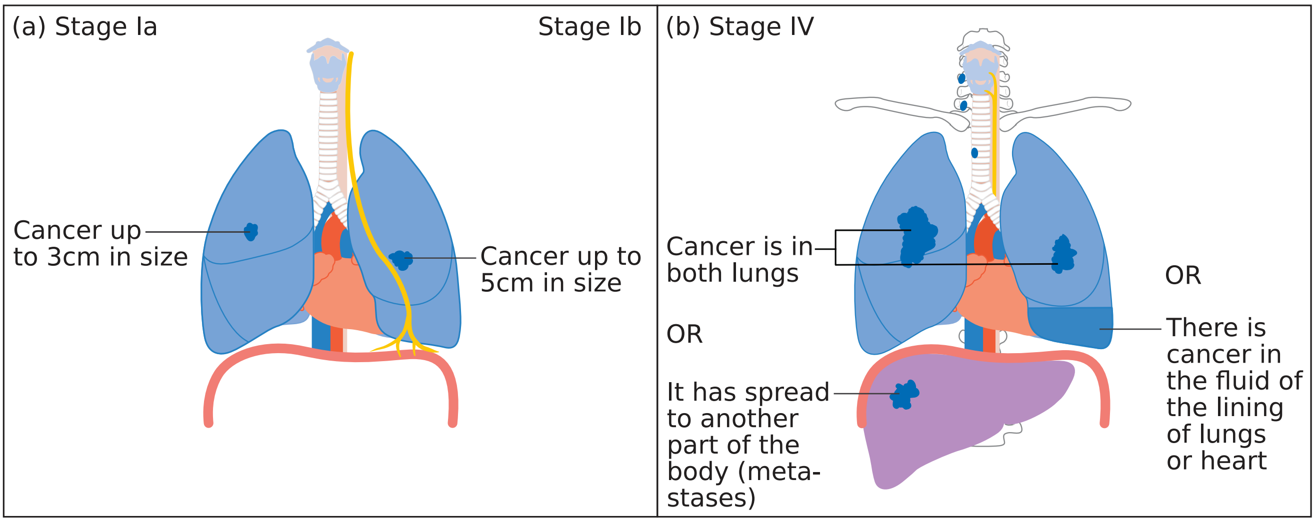

Figure 1.3.: Panel (a) shows stage Ia and Ib which are primarily distinguished by lesion size; panel (b) depicts stage IV which is distinguished by occurrence of metastases, lesions in the lining of lung/heart or lesions in both lungs. In this thesis, the usage of stage IV refers primarily to the latter description. Figure adapted from [CRUK, 2015].

Commonly the tissue affected by the tumor is surgically resected, either by removing segments or whole lobes of the lung, and in some cases resecting the complete lung on one side of the thorax [Renz-Polster and Krautzig, 2008]. Postoperative chemotherapy is often used, as data has shown it to increase the 5 year survival rate from 40 % to about 45 % [Renz-Polster and Krautzig, 2008]. In cases where the tumor is inoperable due to being in close proximity to or even infiltrating critical organs (e.g. esophagus or the heart), radiotherapy may be selected as a final treatment option. Commonly, a fractionated dose of 60 Gy is used for curative or palliative treatment [Renz-Polster and Krautzig, 2008]. As an example of how NSCLC can look like, figure 1.4 shows a NSCLC lesion, specifically a squamous-cell bronchial carcinoma. This cancer type is often related to smoking [Kenfield et al., 2008].

1.2 Radiotherapy – historical overview

The history of radiotherapy is basically beginning with W. C. Roentgen discovering X-rays in November 1895 [Röntgen, 1898]. After the discovery of the so called Roentgen radiation diagnostic applications like radiographs quickly developed. These devices were used on battlefields to find bullets or broken bones in wounded soldiers. There are also reported cases of the treatments of eczema or lupus with X-rays [Connell and Hellman, 2009], including the Austrian physician Leopold Freund treating the birth mark of a five year old girl with X-rays [Freund, 1897]. Further, only 7 months after Roentgen's discovery, X-rays were used by the French physician Victor Despeignes to treat a cancer patient with gastric carcinoma who eventually benefited from radiotherapy [Sgantzos et al., 2014].

Limited by the available low X-ray energies and hence low penetration depths, most of the tumors could not be treated without the infliction of normal tissue damage, such as skin burns [Connell and Hellman, 2009]. The discovery of natural radioactivity, so called γ rays, by Antoine-Henri Becquerel in 1901, as well as the discovery of radium by Marie and Pierre Curie improved the understanding of

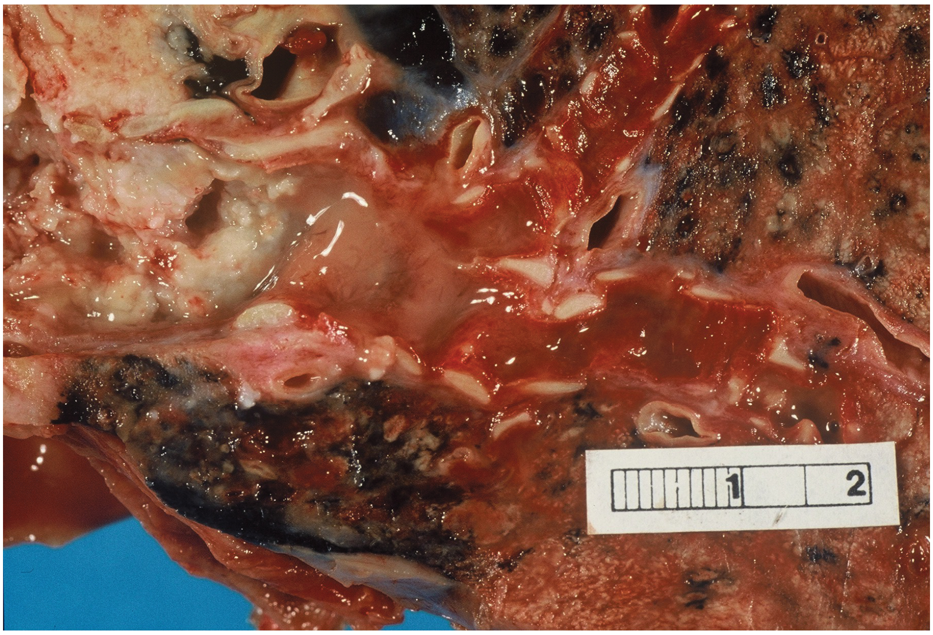

Figure 1.4.: Image of a squamous-cell bronchial carcinoma. The tumor (white tissue in the upper left corner) is obstructing the bronchus. Beyond the tumor, the bronchus is inflamed and contains mucus. The black and dark gray areas indicate, that the patient is a smoker. Image courtesy John Hayman [Hayman, 2007].

radioactivity, made radiation with higher energies available. At the same time, awareness of the risks of ionizing radiation began to rise.

To reach deeper seated tumors, physicians and physicists worked improved the X-ray tubes by increasing the available energies. In 1913, American physicist William Coolidge invented the hot-cathode X-ray tube which produced X-rays with energies up to 200 keV [Coolidge, 1913]. Over the next few decades, the X-ray tube was successively improved and higher energies became available through devices such as the cascade tube which enabled energies up to 700 keV [Connell and Hellman, 2009]. New opportunities were enabled by Donald Kerst's invention of the electron accelerator in 1940 [Kerst, 1940] and the development of the U.S. version of the synchrotron by McMillan at Los Alamos Laboratory [McMillan, 1945]. This led to the development of compact linear accelerators mounted on 360° gantries, which could deliver γ rays with energies of several MeV. These were the predecessors of modern photon therapy technologies like intensity modulated radiotherapy (IMRT), SBRT or volumetric modulated arc therapy (VMAT) which originated in the mid nineties [Connell and Hellman, 2009].

Although a depth dose curve of charged particles was described by W. H. Bragg back in 1903 for α-particles in air [Bragg and Kleeman, 1904], it took until 1946 for the potential of charged particles in radiation therapy to be seen. R. Wilson proposed the use of fast protons to treat deep seated tumors due to their beneficial depth dose profile compared to photons and predicted "that precision exposures of well-defined small volumes within the body will soon be feasible" [Wilson, 1946]. When, in 1948 the synchrocyclotron became available for experiments at Lawrence Berkeley Laboratory (LBL), Berkeley (USA), Tobias et al. investigated the physical and radiobiological properties of the proton beam [Tobias and Todd, 1967]. Patient treatment started in 1954 with protons first and with helium beam later [Schardt et al., 2010]. The use of heavier ions e.g. ^{20}Ne started in 1975 at the Bevalac facility at LBL with particle energies up to 670 MeV/u. In particle therapy the term "heavy ion" is used for every ion heavier than a proton although only light ions up to neon are actually used in therapy. Until the closure of the Bevalac facility in 1992, 443 patients have been treated with ^{20}Ne ions delivered by passive beam shaping systems.

In 1994 at National Institute of Radiological Sciences, Chiba, Japan (NIRS), a research program dedicated to carbon ions was launched. Based on the developments at Berkeley, the treatment delivery system at the Heavy Ion Medical Accelerator (HIMAC) used a similar approach with passive beam shaping [Hirao et al., 1992]. At around the same time, a project for the development of spot scanning for protons was started at Paul Scherrer Institut (PSI) [Pedroni et al., 1995] and raster scanning for carbon ions was developed at GSI Helmholtzzentrum für Schwerionenforschung GmbH (GSI) [Haberer et al., 1993]. The goal of these therapy projects was to increase the conformity and the homogeneity of the delivered dose distribution while increasing normal tissue sparing. These developments also eliminated the neef for patient specific components such as compensators and collimators.

Following pilot studies done in Germany, Heidelberg Ion-Beam Therapy Center (HIT) started treating patients in 2009, and Marburg Ion-Beam Therapy Center (MIT) in 2015. Both centers have been using protons and carbon ions. In Europe, two more ion centers are in operation: National Center of Oncological Hadrontherapy, Pavia, Italy (CNAO) since 2011, and MedAustron in Vienna, Austria since late 2016.

1.3 Ionizing radiation

In radiotherapy, the absorbed dose is one of the most important quantities. As reported in the 50th report of the International Commission on Radiation Units and Measurements (ICRU), the absorbed dose is defined as the mean energy $\mathrm{d}E$ deposited by ionizing radiation in a mass element $\mathrm{d}m$ [ICRU, 1993]. The absorbed dose is also called physical dose and is stated in the SI-unit Gray [Gy]. Introducing the mass density ρ the dose becomes proportional to the quotient of mean energy $\mathrm{d}E$ and volume element $\mathrm{d}V$ (see equation 1.1).

$$D = \frac{\mathrm{d}E}{\mathrm{d}m} = \frac{1}{\rho}\frac{\mathrm{d}E}{\mathrm{d}V} \quad [1\,\mathrm{Gy} = 1\,\mathrm{J/kg}]. \tag{1.1}$$

The dose absorbed in matter is generated by two kinds of ionizing radiation: directly ionizing radiation e.g. charged particles, like electrons or ions and indirectly ionizing radiation, like high energy photons or neutrons. The different mechanisms behind the energy deposition are described for photons and and ions in the following.

1.3.1 Photons

When photons interact with tissue, there are three major attenuation processes depending on the initial energy: The photo electric effect, Compton scattering and pair production [Meschede, 2015, p. 838–

839]. The attenuation $I(x)$ of the initial photon intensity I_0 is described by the absorption law introduced by Lambert-Beer:

$$I(x) = I_0 \cdot \exp(-\mu x), \tag{1.2}$$

where x is the penetration depth and μ the material specific attenuation coefficient. Figure 1.5 shows the depth dose curves for photon irradiation on a water phantom for three radiation sources: X-rays from a cathode ray tube at 120 keV, gamma radiation from a ^{60}Co source at about 1.25 MeV) and photons from a linear accelerator at 18 MeV. The exponential decay is present for all three energy ranges, but it is more pronounced for the X-rays. For the two higher energies, there is a buildup effect, which pushes the initial dose maximum further into the tissue by some centimeters, before the exponential decay becomes dominant. This initial buildup effect can be traced back to secondary Compton electrons which mainly scatter in forward direction until they reach an equilibrium between dose deposition and creation of further secondary electrons [Schardt et al., 2010]. This smaller dose deposition in the entry channel makes the use of high energy photons (several MeV) more favorable, and is, therefor, common practice in modern photon therapy. However, due to the exponential decrease of the deposited dose, photon therapy typically requires several treatment fields to not exceed normal tissue constraints.

1.3.2 Ions

As the depth dose profile is inverse compared to photons, ion therapy is commonly used to treat deep seated tumors, which typically requires particle ranges up to 30 cm. This corresponds to particle energies of up to 220 MeV/u for protons and 430 MeV/u for carbon ions [Schardt et al., 2010]. To reach these energies, particle velocities of about $\beta \equiv v/c = 0.7$ are required. The mechanism behind the energy deposition of charged particles are mainly inelastic collisions with orbital electrons of the target atoms. The Bethe-Bloch equation describes the energy loss of the charged particles $\mathrm{d}E$ per unit path length $\mathrm{d}x$, also known as “stopping power” [Bethe, 1930; Bloch, 1933]

$$-\frac{\mathrm{d}E}{\mathrm{d}x} = 4\pi \frac{e^4 Z_p^2}{m_e v^2} \cdot \frac{N_A Z_t \rho_t}{A_t} \left[\ln \frac{2 m_e v^2}{\langle I \rangle} - \ln\left(1-\beta^2\right) - \beta^2 \right]. \tag{1.3}$$

Z_t and Z_p denote the charge of the target and of the projectile, m_e and e are the electron mass and the elementary charge, v is the velocity of the projectile, N_A is the Avogadro number, ρ_t and A_t are the density and the atomic mass of the target material and $\langle I \rangle$ is the mean ionization energy of the target atoms, which is about 80 eV for liquid water [Schardt et al., 2010]. By increasing the initial kinetic energy of the charged particles, the sharp dose maximum with its characteristic steep distal fall-off, the so called Bragg peak, is shifted deeper into the irradiated tissue. This is illustrated in figure 1.5 for carbon ions with energies of 250 MeV/u and 300 MeV/u.

Using the stopping power presented in equation 1.3, the expression for the dose from equation 1.1 can be written as

$$D[\mathrm{Gy}] = 1.6 \cdot 10^{-9} \cdot \underbrace{\frac{\mathrm{d}E}{\mathrm{d}x}\left[\frac{\mathrm{keV}}{\mu\mathrm{m}}\right]}_{\sim\mathrm{LET}} \cdot \left[\rho\left[\frac{\mathrm{g}}{\mathrm{cm}^3}\right]\right]^{-1} \cdot F\left[\mathrm{cm}^{-2}\right]. \tag{1.4}$$

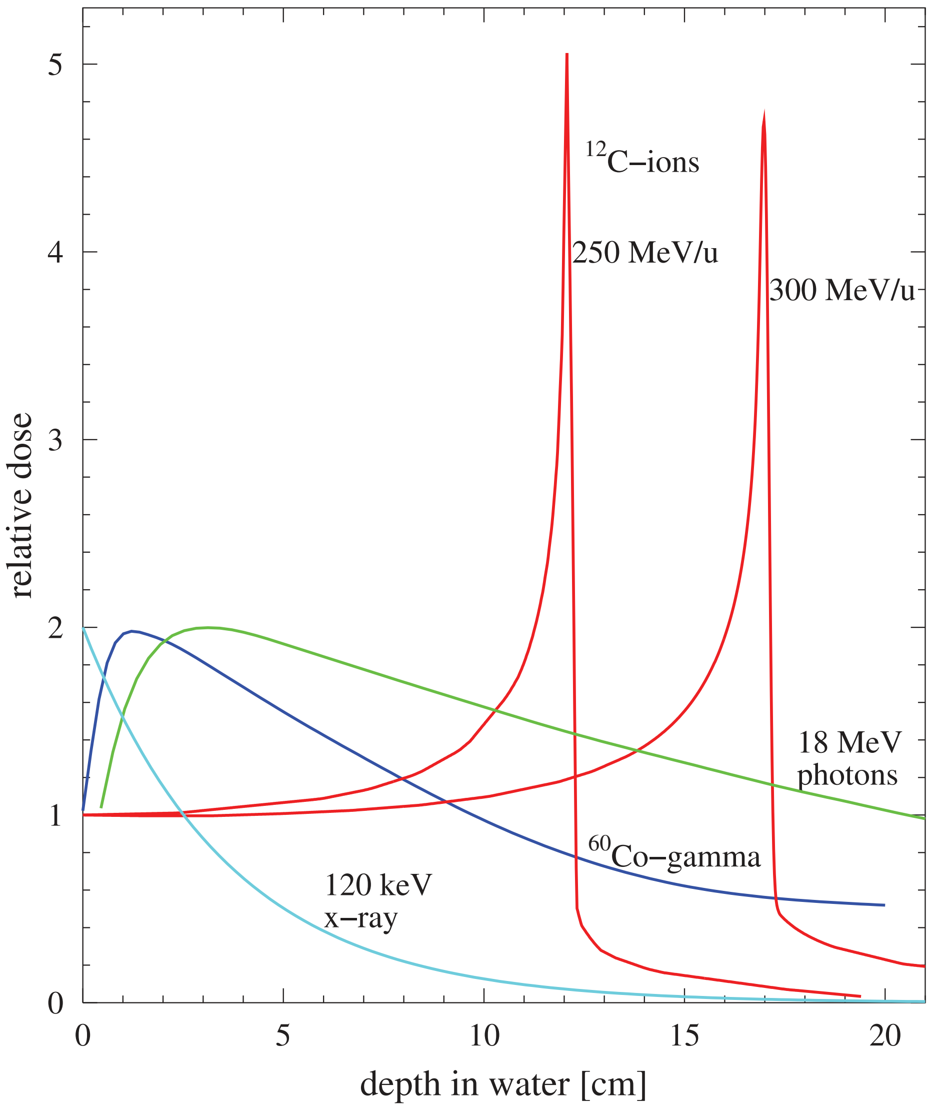

Figure 1.5.: Relative dose over depth in water in cm. The depth dose curve is shown for X-rays with 120 keV (cyan line), gamma rays with 1.1732 MeV and 1.3325 MeV from ^{60}Co (blue line), 18 MeV photons from a linear accelerator (green line) and carbon ions with 250 MeV/u and 300 MeV/u (red lines). Figure from [Schardt et al., 2010].

This formulation is valid for parallel beams with a particle flux F. In the context of radiobiology, a similar quantity related to the stopping power is used: linear energy transfer (LET). LET is by convention denoted in keV/μm, which refers to the energy deposited in the stopping medium by the slowing-down particle [Schardt et al., 2010]. The LET is an important measure to assess the radio biological efficacy of the ionizing radiation. It is especially used for the calculation of the relative biological effectiveness (RBE), which is described in further detail in section 1.4.1.

1.3.2.1 Range straggling

The Bethe-Bloch equation describes the stopping power for a single particle. However, delivering clinically relevant doses require thousands of particles to be slowed down within the tissue. As energy loss by inelastic Coulomb scattering has statistical fluctuations, this results in a broadening of the Bragg peak and a degradation of the peak-to-entrance dose ratio. In the limit of many collisions, the law of large numbers is valid and these statistical fluctuations can be described with a Gaussian distribution [Bohr, 1940; Ahlen, 1980].

From this distribution, the relative straggling ratio

$$\frac{\sigma_R}{R} \propto \frac{1}{\sqrt{M}} \tag{1.5}$$

can be derived, where σ_R is the straggling width, R is the mean range M is the particle mass [Schardt et al., 2010]. Accordingly, this ratio becomes smaller for heavier ions. For example, carbon ions have a factor 3.5 smaller relative range straggling than protons. However, in clinical treatment, the profile of a Bragg is broader, which is primarily caused by the non-heterogeneity of the tissue of the patient, especially when compared to initial measurements in water.

It can be advantageous to exploit this effect to reduce treatment duration. By deliberately extending the longitudinal beam broadening, the number of particle energies necessary to cover a tumor volume is reduced. Further detail is given in section 1.5.2, where the use of a passive range modulator build from polymethyl methacrylate (PMMA) is described for the raster scanning method [Weber and Kraft, 1999].

1.3.2.2 Lateral scattering

As particles traverse through tissue, they experience small lateral deflections. These are mainly caused by elastic Coulomb scattering interactions with the target nuclei, whereas scattering due to collisions with the electron shell of the target atoms are much less significant and can be neglected. The analytical description of this lateral beam broadening by Molière [1948] is in good empirical agreement, as measured e.g. for protons by Gottschalk et al. [1993]. Since laterally scattered particles can be further scattered, the beam spread becomes larger with increasing penetration depth. Furthermore, the beam spread is dependent on the material composition of the target. For a given thickness, targets consisting of heavier elements cause greater lateral spreading of the incident ion beam [Schardt et al., 2010].

Similarly, heavier ions produce less lateral spread than protons [Weber and Kraft, 2009]. For a given range of about 16 cm in water, the angular spread of protons is more than three times larger than for carbons [Schardt et al., 2010]. The consideration of lateral scattering is also important for OAR sparing during treatment planning, since sharp penumbras of the particle beams are necessary to reduce the irradiation of surrounding tissue.

1.3.2.3 Nuclear fragmentation

Compared to the stopping power generated by Coulomb interactions of the projectiles with the electron shell of the target atoms, the contribution of nuclear interactions to the overall stopping power is much smaller. Nonetheless, for high energetic particles with long ranges, nuclear interactions (such as target or projectile fragmentation) contribute significantly to the dose deposited in the irradiated tissue. For all ions heavier than protons, target fragmentation has the highest dose contributions.

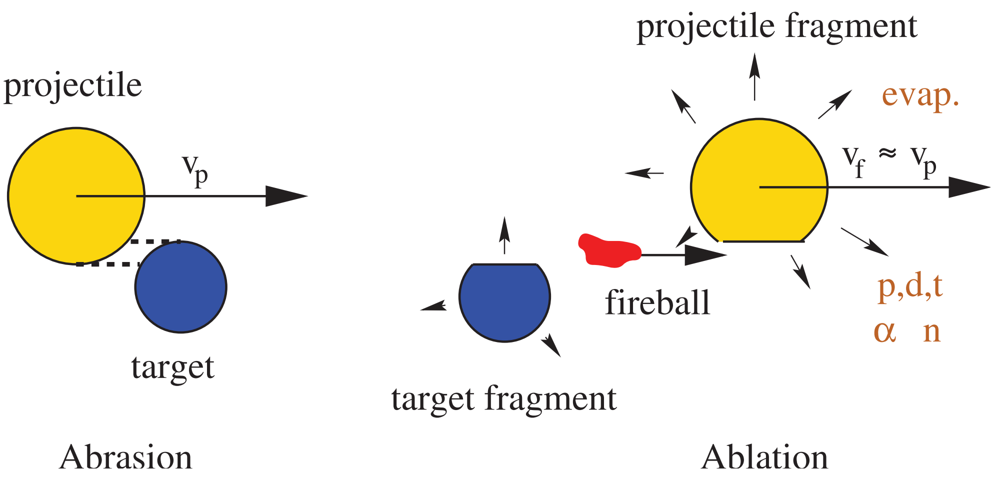

Figure 1.6.: Schematic illustration of the abrasion-ablation model of peripheral collisions of high energy ions as described in Serber [1947]. Figure from [Schardt et al., 2010].

For geometrical reasons, peripheral collisions are the most frequent nuclear reactions occurring along the stopping path of the ions [Schardt et al., 2010]. The peripheral collision is a two-step process which is well described with the abrasion-ablation model by Serber [Serber, 1947]. This process is schematically illustrated in figure 1.6. During abrasion, the projectile abrades the partial overlap of the target nuclei due to their geometrical cross sections and creates a reaction zone, the so called fireball. In the second step, the ablation, the remaining projectile and target fragments deexcite by evaporation of a nucleus or clusters. Detailed studies of these nuclear fragmentation reactions have been performed by Goldhaber and Heckman [1978]; Hüfner [1985]; Lynch [1987].

For radiotherapy with high energy ion beams, fragmentation is important for two reasons: (i) The nuclear reactions cause a loss of primary ions and produce a buildup of lower-Z fragments. The relevance of these effects increases with increasing penetration depth. (ii) The secondary projectile-like fragments travel at almost the same speed as the primary ions. Due to having about the same energy and smaller mass than the primary ions, the fragments have a longer range than the primary ions [Schardt et al., 2010]. This causes the dose tail behind the steep dose fall-off of the Bragg peak which is present for all ions heavier than protons (see figure 1.5).

For carbon ions stopped in water, hydrogen and helium fragments are most abundantly produced [Haettner et al., 2006]. Fragments heavier than boron are slowed down shortly after the Bragg peak. Lighter fragments such as hydrogen and helium are the predominant ions in the dose tail [Schardt et al., 2010]. For heavier ions the dose tail becomes more pronounced, until the depth profile of the deposited dose becomes unfavorable for therapy. The distal dose fall-off becomes less sharp and the advantages for a conformal dose deposition are lost [Kraft, 2000]. For this reason, ions heavier than neon are commonly not used in ion therapy.

For the treatment of deep seated tumors, higher penetration depths are needed. However, the impact of the fragmented ion species on the deposited dose increases with higher penetration depth. Especially the relative biological effectiveness (RBE) differs for different ion species. Hence, accounting for fragmentation during treatment planning is in particular important for the calculation and optimization of the biological dose. This is done by generating dedicated base data tables, e.g. particle spectra for different depths in water. These tables are gained from analyzing fragmentation measurements, which has been done at several centers [Maccabee and Ritter, 1974; Schimmerling et al., 1989; Llacer et al., 1990; Schall et al., 1996; Haettner et al., 2006].

1.3.2.4 Track structure

From the microscopic point of view, the inhomogeneous spatial dose distribution generated by ions (shown in figure 1.7) differs from the homogeneous dose distribution created by high energy photons (see section 1.4). Ions lose their energy through electrical interactions with the Coulomb potentials of target atoms or molecules. In this process, secondary electrons or so called δ-electrons are emitted. Further on, these δ-electrons are frequently scattered within the target material, depositing energy in a radial dose distribution around the ion track. This localized energy distribution of particles results in a larger biological effect which is described in section 1.4.

The dominant ionization process through Coulomb interactions can be described by the binary-encounter approximation which assumes that the projectile collides with a quasi-free electron [Kraft and Krämer, 1993]. For electrons with energies below 50 eV, electron excitations are the dominant process, while ionization is the major process for higher energies, creating further electrons which again contribute to the deposited dose. The ionization cross section for electrons reaches its maximum at about 100 eV which corresponds to a mean free path length of a few nm. This increases the probability of two ionization events occurring within 2 nm, which corresponds to distance of the two strands of the DNA double helix [Schardt et al., 2010] (see figure 1.7).

The δ-electron track structures strongly depend on particle species and kinetic energy. Figure 1.7 shows the highly inhomogeneous energy distribution for protons and carbon ions with energies of 0.2 MeV/u, 1 MeV/u and 10 MeV/u. As the particles are slowed down and their energy decreases, the number of liberated secondary electrons increases. Compared to protons, the density of secondary electrons is higher for carbon ions. The radial dose distribution, which approximately follows an $1/r^2$ dependence, can be well described by analytical models [Chatterjee and Schaefer, 1976; Katz and Cucinotta, 1999] and Monte Carlo simulations [Paretzke, 1986; Krämer, 1995]. It has also been confirmed in experimental studies [Varma et al., 1977].

1.4 Radiobiology

The goal of radiotherapy is to irradiate the tumor, while minimizing normal tissue complications. In order to achieve this, it is important to understand the radio-biological mechanisms behind radiological damage.

In the energy regimes relevant for therapy, the energy of photons is predominantly transferred via photo electric effect and Compton scattering. Due to the small cross sections of these processes, the number of ionization events per incident photon within the cell volume is also small [Schardt et al., 2010]. Hence, only few electrons are emitted from the target atom or molecule in the primary interaction with the photon, which requires many photons to achieve a clinical dose. Due to the numerous random interactions, the deposited doses are approximately continuous, creating a homogeneous dose, often referred to as “dose bath”.

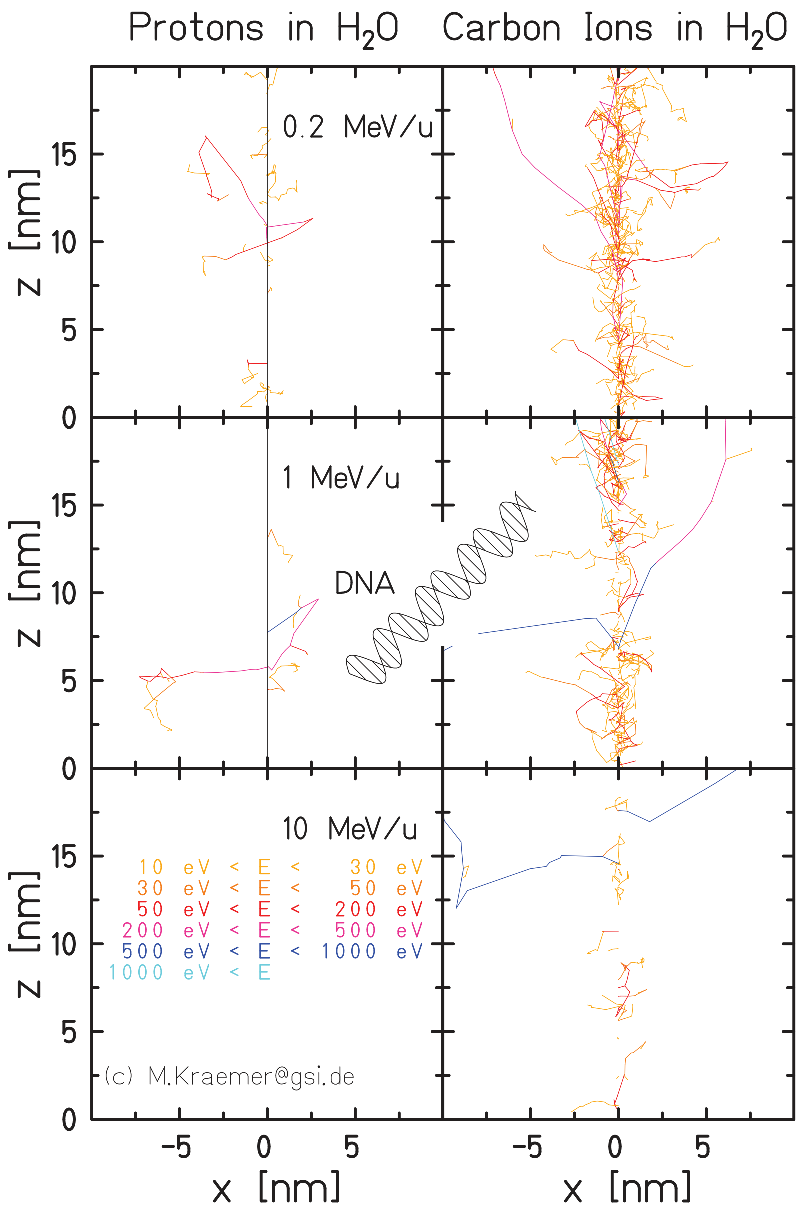

Figure 1.7.: Track structure of secondary electrons for protons and carbon ions in water with 3 different energies (0.2 MeV/u, 1 MeV/u and 10 MeV/u) simulated with Monte Carlo code 'TRAX'. The schematic figure of the DNA double helix is in scale. Figure from [Krämer and Durante, 2010].

Assuming that the deoxyribonucleic acid (DNA) molecule is the most sensitive target in a cell nucleus, the radial dose distribution of an ion track creates more DNA damage than the homogeneous dose deposited by photons. For carbon ion tracks, as depicted in figure 1.3.2.4, the area with the highest deposited dose is on the order of some nanometers.

Typically, there are two pathways through which the radiation damage is propagated: A *direct* hit of the DNA by the ion itself or a liberated secondary electron, or an *indirect* hit created by radiation induced free radicals like hydroxyl (OH) from hydrolysis [Hall and Giaccia, 2012]. These radicals can travel for a few nanometers and are able also able to damage the DNA. Both sorts of interaction are illustrated in figure 1.8(a).

The most common forms of damage are single strand breaks SSB and double strand breaks DSB of the DNA molecule (as illustrated in figure 1.8(b)). single strand break (SSB) are easier to repair for the cell, whereas double strand breaks (DSB) destroys the double helix of the DNA, which makes the repair process more difficult and increases the susceptibility to errors during repair. This eventually leads to cell inactivation in most cases. Therefor, the DSB is considered as the most hazardous damage for a cell. Since more complex DNA damage does impair the cell's repair capabilities, the radiation damage induced by heavy ions is larger than for photons [Nikjoo et al., 1999].

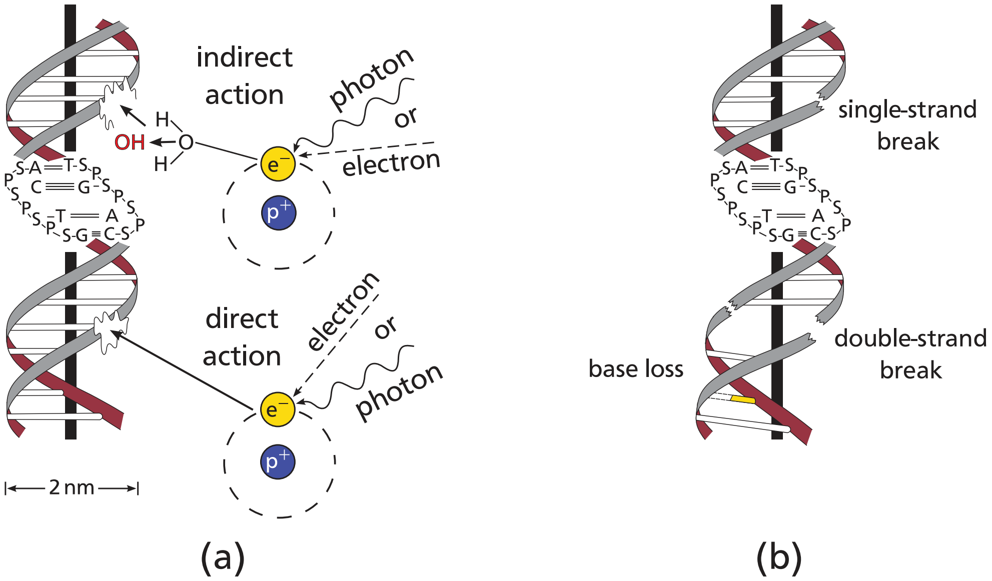

Figure 1.8.: Schematic of interaction of ionizing radiation with DNA double helix. (a) differentiation between direct and indirect interaction of radiation with DNA. (b) classification between single (SSB), double strand break (DSB) and base loss of DNA. Figure adapted from [Hall and Giaccia, 2012].

In-vitro cell survival experiments are the most common way to analyze the damage caused by ionizing radiation, as for example described by Puck and Marcus [1956]. After irradiation with photons or ions, cell proliferation was analyzed over the course of two weeks. Cells which have built a colony with more than 50 daughter cells were counted as survivors. After normalization to the number of initial cells, the fraction of surviving cells (S) is parametrized with the linear-quadratic (LQ) model

$$S(D) = \exp\left(-\alpha D - \beta D^2\right) \tag{1.6}$$

where D is the absorbed dose and the experimentally determined parameters α and β [Hall and Giaccia, 2012, p. 39]. Schematic cell survival curves are shown in figure 1.9, where the survival fraction of irradiated cells is depicted over the absorbed dose in Gy. The α/β ratio determines the shoulder of the depicted cell survival curves. Compared to photons, the α/β ratio is typically higher for high LET radiation like heavy ions. This results in a steeper, more linear shape of the survival curve for heavy ions (dashed red line). This strong influence on the shape of the survival curve makes theα/β ratio an important quantity in radiation therapy [Fowler, 1989].

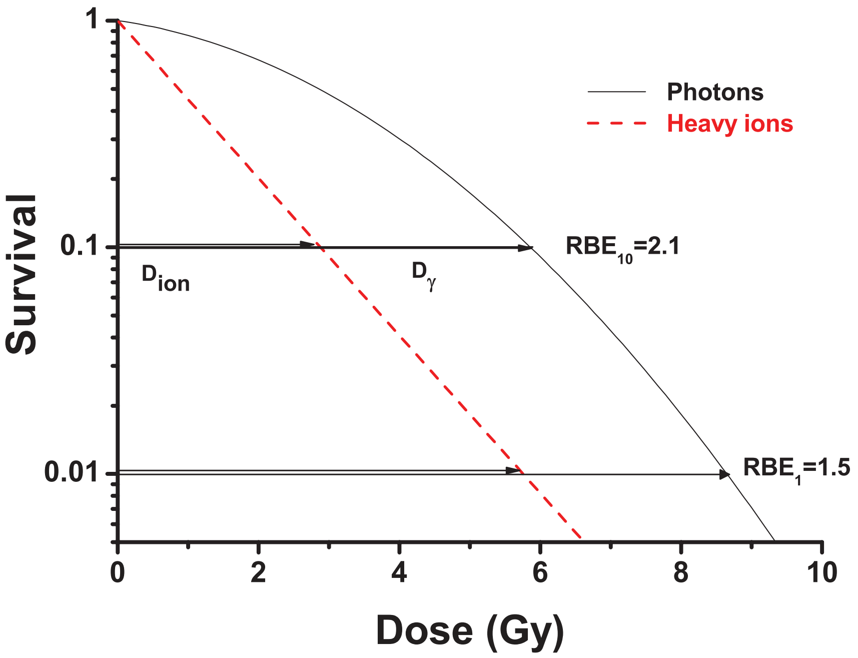

Figure 1.9.: Schematic illustration of relative cell survival depicted over absorbed dose in Gy. Relative biological effectiveness (RBE) values given for 1 % and 10 % survival rate. Figure from [Schardt et al., 2010].

1.4.1 Relative biological effectiveness

The previous section described, how the damage to the DNA is caused by δ-electrons for both charged particles and photon irradiation. Both modalities differ in their pattern of the microscopic dose, where heavy ions show a higher radiobiological effect due to their higher LET. Since most knowledge about the biological efficacy of radiation is gained from X-ray experiments, the concept of a relative biological effectiveness (RBE) represents an elegant way to compare the biological effects of heavy ion radiation versus photon radiation for a given biological endpoint. The RBE is defined as

$$\mathrm{RBE}_{\text{iso-effect}} = \frac{D_{\mathrm{ref}}}{D_{\mathrm{ion}}}, \tag{1.7}$$

where D_{ion} is the absorbed ion dose and D_{ref} is the absorbed reference dose, typically X-rays. In figure 1.9 the RBE is stated for the 1 % and 10 % survival rates. Due to the linear shape of the survival curve for heavy ions versus the more parabolic shape for photons, the RBE becomes larger for lower doses.

For heavy ions, the RBE depends on the biological endpoint, the dose, the LET, the tissue type and the composition of the radiation field, which makes it a complex quantity to calculate. Hence, the RBE values vary for different locations within the patient. To estimate the RBE value, different models have been developed and validated. The aim of the carbon ion pilot project at GSI was to enable the optimization of a homogeneous biological dose for patient treatment, for which the local effect model (LEM) has been developed [Scholz et al., 1997; Krämer and Scholz, 2000, 2006]. Since its introduction, the LEM has also received some revisions [Elsaesser and Scholz, 2007; Friedrich et al., 2012]. The LEM is used routinely at clinics in HIT and MIT within the proprietary treatment planning system (TPS) “Syngo” by Siemens. LEM has also been licensed for implementation in the commercially available TPS “RayStation” [RaySearch, 2013].

In the heavy ion community, the concept of considering variable RBE in treatment planning is widely accepted. However, in proton therapy a fixed RBE value of 1.1 is still commonly used. The topic of a variable proton RBE remains under heavy discussion [Underwood et al., 2017; Paganetti, 2018].

1.5 Accelerators & treatment delivery

In particle therapy, synchrotron or cyclotron accelerators are used to generate ions within the therapeutic energy regime. In facilities which use heavy ions like HIT, MIT, CNAO or MedAustron synchrotron accelerators are used. These accelerators are capable of accelerating both protons and carbon ions. Facilities using protons only, predominantly rely on cyclotron accelerators in order to reduce space consumption, which is significantly less compared to a synchrotron accelerator with diameters from about 25 m to 30 m versus approximately 3 m for typical cyclotrons.

Comparing synchrotrons and cyclotrons, there is also a major difference in the way particle energies are generated. Cyclotrons are limited by construction in the maximum deliverable particle energy. By design, this limitation is set to the maximum energy necessary to generate a range of 30 cm in water. This corresponds to an energy of 220 MeV/u [Schardt et al., 2010]. To reach lower energies, a degrader consisting of an absorbing material like PMMA is used. The cyclotron is capable of producing a continuous beam. If a degrader wheel with decreasing material thickness is used, fast energy changes are possible.

This is in contrast to synchrotrons, where ion bunches of about 10^6 to 10^9 particles are accelerated to the requested energy. In addition to their ability to accelerate heavier ions, synchrotrons are capable of generating higher particle energies, depending on the size of the accelerator and is magnetic stiffness. However, as each ion bunch is accelerated separately, the time to change the particle energy is not instantaneous, requiring a few seconds. Nonetheless, in the latest revision of the HIMAC synchrotron, there has been a significant drop in the time necessary to change particle energy. The introduced multiple-energy operation mode enabled energy transition times of 10 ms/step to 50 ms/step for corresponding energy intervals of 1 MeV/u to 7 MeV/u [Mizushima et al., 2017]. Recent developments in the construction of superconducting cyclotrons will enable the acceleration of helium or carbon ions with cyclotrons in the near future [Jongen et al., 2010; Kang et al., 2012].

In the context of radiotherapy, the purpose of the delivery system is the transportation of the ion beam into the patient, to cover the planning target volume accurately and homogeneously with the planned dose distribution [Schardt et al., 2010]. For the interested reader, an overview of the variety of possible solutions in treatment delivery can be found in Chu et al. [1993]. In the following sections, the two most common approaches are presented: passive scattering and active scanning.

1.5.1 Passive scattering

In treatment delivery with passive scattering, a narrow and mono-energetic ion beam is shaped to create a conformal and homogeneous dose distribution. Figure 1.10 schematically shows the required components. The process of the beam shaping can is divided into two parts, handling the lateral and longitudinal shape of the dose distribution.

First, a pencil beam with a full width at half maximum (FWHM) of some millimeters is laterally broadened from being irradiated onto a scattering system. This is usually done through a double scattering system consisting of two metal targets from which the second one has a T-shaped geometrical cross section. The scattering system broadens the beam diameter to be larger than the lateral cross section of the tumor to irradiate. A brass collimator is used to reduce the penumbra of the lateral beam profile to a sharp gradient. Additionally, the collimator has the lateral shape of the largest lateral extension of the patient specific tumor volume in beam's eye view (BEV). The beam shaping modifications can be seen in the upper row of figure 1.10.

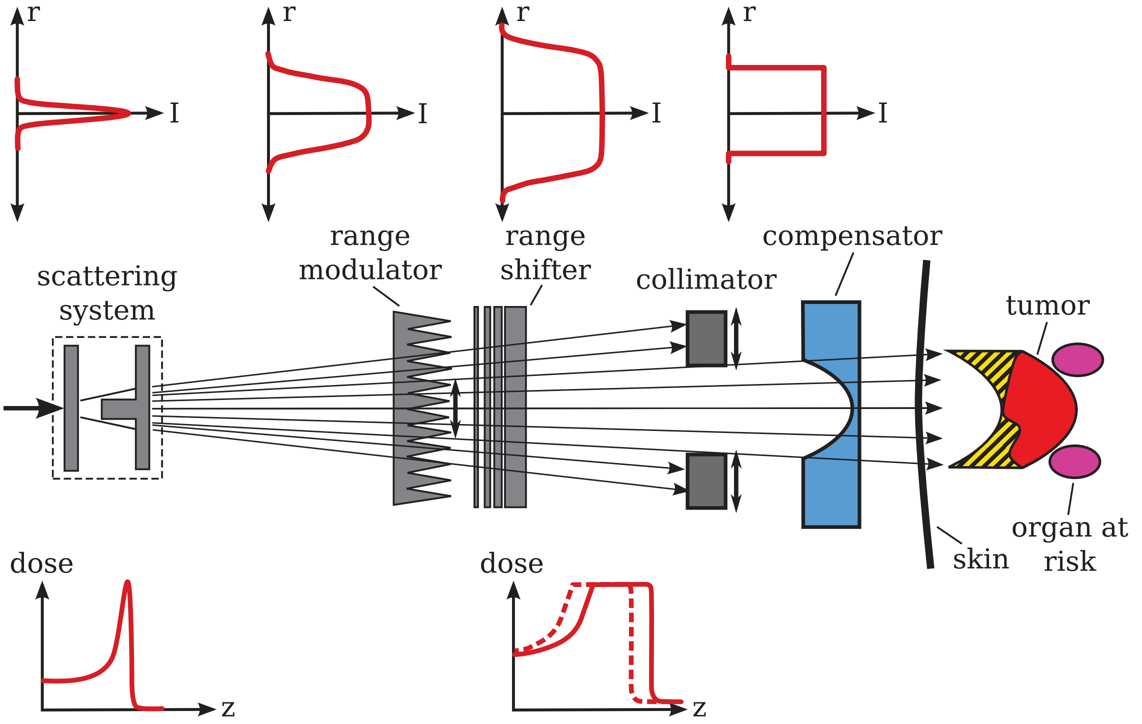

Figure 1.10.: Schematic of passive delivery of ion beams. The scattering system and the collimator are used to shape the beam profile laterally. The range modulator, the range shifter and the compensator are used to adapt the longitudinally dose distribution from a pristine Bragg curve to a SOBP. The compensator is especially important to form the distal areas of the dose distribution enabling the sparing of OARs. Figure from [Schardt et al., 2010].

The second part of the beam shaping modifications affects the depth dose distribution. Initially, there is a quasi mono-energetic pristine Bragg curve. A ripple filter is used as a range modulator to broaden the longitudinal dose profile to a flat and homogeneous dose distribution. Further, a range shifter consisting of PMMA plates of different thicknesses is used to reach more shallow tissue areas by reducing particle range. Since tumors typically are spherically shaped, a compensator, machined from PMMA, can be used, to conform the distal part of the treatment volume. A compensator can also be applied for sparing OARs in close proximity of the distal end of the target volume. However, it is important to note, that distal dose shaping merely shifts parts of the dose distribution, which can also mean an increase of normal tissue dose (see hatched area in figure 1.10). It is important to note that the collimator and compensator are patient and field specific, and have to be built individually for each patient.

The approach was pioneered at Havard, especially the design of the range modulators and compensators, as well as the optimization of range-compensated scattering systems [Koehler et al., 1975, 1977; Gottschalk and Wagner, 1989].

1.5.2 Active scanning

Active scanning offers some distinctive advantages compared to passive scattering. First, no patient or field specific components are necessary. The dose distribution is tailored to the patient within the TPS only. Second, the ability to change the intensity of each grid spot within the tumor volume enables the use of intensity modulated particle therapy (IMPT) with two or more irradiation fields, and thereby superior OAR sparing. The IMPT technique was first developed for protons at PSI in the early nineties [Lomax, 1999], but quickly transferred to the use for heavy ions at GSI.

Active scanning differs considerably from passive scattering, although both methods initially use narrow pencil beams with Gaussian shaped transversal profile. To cover the entire tumor volume using active scanning, the tumor is divided into iso-energy slices (IESs) along the BEV axis. The irradiation of these slices can be achieved by varying the particle beam energy, thereby changing the depth of the Bragg peak. To cover the lateral extent of the IESs with dose, each of these IES is divided into a two dimensional grid of typically 2 mm sized grid spots (see illustration in figure 1.11). Each of these grid spots represents a position that a pencil beam spot will be delivered to during treatment. Two scanning magnets are used to laterally scan the pencil beam to each of these spot positions on the grid: The first magnet is used for horizontal, the second magnet for vertical scanning. A described method is called “raster scanning” and has been developed at GSI. The required control system which is monitoring the position, energy and intensity of the ion beam at any time during treatment has been developed by Haberer et al. [1993]. Pioneering work for other scanning methods was done at National Institute of Radiological Sciences, Chiba, Japan [Kanai et al., 1983] and Paul Scherrer Institut[Pedroni et al., 1995].

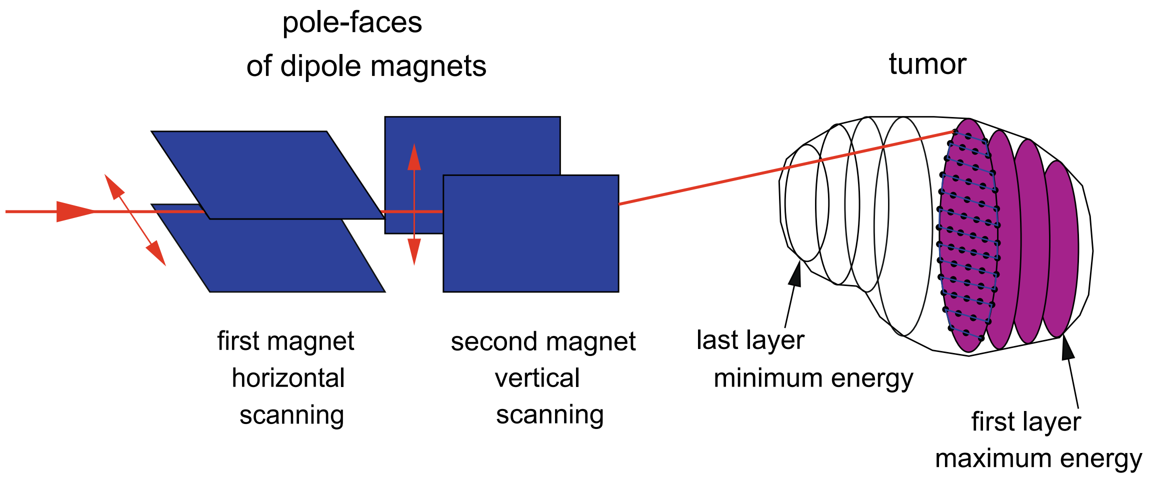

Figure 1.11.: Schematic of active delivery of carbon ions. The raster scanning method uses two magnet for vertical and horizontal deflection of the ion beam over the iso-energy slice (IES). The depth of the IES is controlled by ion energy. Figure from [Schardt et al., 2010].

In order to achieve a homogeneous dose over an IES, the FWHM of the Gaussian beam profile is chosen with respect to the raster grid spacing Δs (see figure 1.12(a)). Empirically, the beam spot size is usually set to $\text{FWHM} = 3 \times \Delta s$ provide a sufficient overlap.

Commonly, the narrow longitudinal dose profile of a pristine carbon Bragg peak is broadened to cover a depth of 2 mm to 3 mm. This can be achieved by using a ripple filter as developed by Weber and Kraft [1999]. A ripple filter consists of triangular grooves machined into a sheet of PMMA, creating a SOBP, as seen in figure 1.12(b). Typically, the IESs are addressed in descending order, starting with the most distal one (highest particle energy). Due to the dose already deposited in the proximal IESs by beams traversing to deeper IESs, the intensity of the more proximal IESs must be reduced to create a flat and homogeneous integral dose.

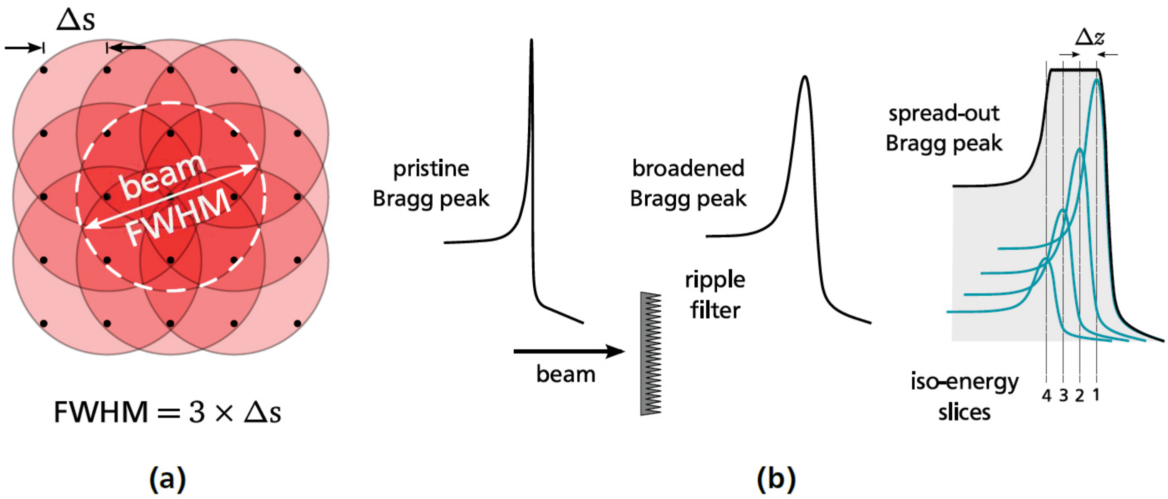

Figure 1.12.: Schematic view of lateral and longitudinal dose shaping. (a) lateral overlap of Gaussian pencil beams and (b) pristine Bragg peak broadened by a PMMA ripple filter to create spread out Bragg peak (SOBP). Figure from [Richter, 2012].

1.6 Treatment planning

This section provides an overview of the aspects of treatment planning: First, a brief description of the pencil beam dose algorithm used in TRiP98 is presented in section 1.6.1, followed by the description of the basic cost function used in treatment plan optimization (see section 1.6.3). A description of internal organ motion (see section 1.6.4), their implications (see section 1.6.6) and how to mitigate these effects (see section 1.6.7) are then described. Furthermore, the topic of 4D treatment planning is addressed (section 1.6.8), including methods like image registration to process time resolved image data for treatment planning (section 1.6.9).

1.6.1 Physical dose calculation

The beam model used for the calculation of the physical dose is based on a pencil beam algorithm, which has been developed at GSI during the carbon ion pilot project. The partial dose deposited in position $\vec{r}$ by an pencil beam with energy E_{beam} located in position $\vec{r_0}$ is described by [Krämer et al., 2000]:

$$D(E_{\text{beam}}, \vec{r})[\text{Gy}] = 1.6 \cdot 10^{-8} \cdot \underbrace{d(E_{\text{beam}}, z) \left[\frac{\text{MeV}}{\text{g cm}^{-2}}\right]}_{\text{depth contribution}} \cdot \underbrace{\frac{1}{2\pi\sigma^2 [\text{mm}^2]} \cdot \exp\left(-\frac{r^2}{2\sigma^2}\right)}_{\text{lateral contribution}} \cdot N, \tag{1.8}$$

where $r = \sqrt{(x - x_0)^2 + (y - y_0)^2}$ is the lateral distance from the beam center, σ the beam width of the symmetrical Gaussian beam profile and N is the total number of particles. The energy loss distribution $d(E_{\text{beam}}, z)$ of a given initial beam energy E_{beam} as a function of the penetration depth z can be derived from the Bethe-Bloch equation and is modeled for treatment planning (TP) by the YIELD transportation model (see [Krämer et al., 2000]). Apart from the single particle energy loss, the YIELD model also describes energy straggling and projectile fragmentation processes, which is necessary to match experimentally determined dose distributions measured in water [Krämer et al., 2000].

Treatment planning at GSI is, as in most other facilities, based on CT imaging of the patient's internal anatomy. Hence, the dose calculation is performed on a voxel-wise basis. A CT voxel is the three dimensional representation of an pixel, describing a small unit of volume. In modern CT images, the edge length of a voxel is typically between 1 mm and 2.5 mm.

A typical treatment plan consists of thousands of pencil beams with several energies and a spread of lateral positions. Hence, the dose in a single voxel i consists of the contributions from many pencil beams. These contributions include pencil beams which terminate within the voxel i, depositing a majority of their energy at the voxel location, pencil beams j aiming at more distal location, which are traversing through the location of voxel i and contributions of lateral scattering by neighboring beam spots j. The dose contributions from all pencil beams j to voxel i are stored in a correlation matrix c_{ij} which results from the beam model presented in equation (1.8). Hence, the total dose of a single CT voxel with index i is given as the sum over all contributing pencil beams

$$D^i_{\text{phys}}(\vec{N})[\text{Gy}] = \sum_j c_{ij} N_j = \vec{c_i}^{\,T} \cdot \vec{N}. \tag{1.9}$$

The dose D^i_{phys} can also be described as the scalar product of the *i-th* line of the correlation matrix $\vec{c_i}^{\,T}$ with the particle vector $\vec{N}$, containing the particle numbers N_j of each pencil beam.

1.6.2 Biological dose calculation

As described in section 1.4.1, the biological effect of ions is larger than of an equivalent photon dose. This higher biological efficacy due to the microscopic track structure is described by the RBE value. In previous projects at GSI, homogeneous biological dose optimization and biological dose calculation was implemented into TRiP98, based on the local effect model (LEM). The biological dose for a voxel i is defined as

$$D^i_{\text{bio}}(\vec{N}) = D^i_{\text{phys}}(\vec{N}) \cdot \text{RBE}^i(\vec{N}), \tag{1.10}$$

with the physical dose D^i_{phys} (see equation (1.9)), the relative biological effectiveness, RBE^i, and the particle vector, $\vec{N}$, containing the number of particles N_j to be irradiated for each pencil beam [Krämer et al., 2000; Krämer and Scholz, 2006]. Since the RBE is depending on many different quantities, such as particle energy, particle spectra, tissue type, biological endpoint, LET, it varies for different locations within the patient.

Using the low dose approximation as described by Krämer and Scholz [2006], the biological dose can be analytically expressed as

$$D^i_{\text{bio}}(\vec{N}) = \sqrt{\frac{\alpha_i \cdot \left(\vec{c}_i^{\,\text{T}} \cdot \vec{N}\right) + \beta_i \cdot \left(\vec{c}_i^{\,\text{T}} \cdot \vec{N}\right)^2}{\beta_x} + \left(\frac{\alpha_x}{2\beta_x}\right)^2} - \frac{\alpha_x}{2\beta_x}, \tag{1.11}$$

where α_x and β_x are the alpha and beta values of the photon survival curve, α_i and β_i the alpha and beta values calculated for each voxel i from using the LEM [Elsaesser and Scholz, 2006; Krämer and Scholz, 2006]. Unlike the physical dose, the biological dose also depends quadratically on the particle vector $\vec{N}$. This behavior becomes important for the next chapter, which addresses the treatment plan optimization.

1.6.3 Plan optimization

The aim of plan optimization during treatment planning is to determine the optimal machine parameters of the delivery system which generates the desired dose distribution within the patient, providing a sufficient dose coverage for the tumor volume and acceptable OAR sparing. Namely, these machine parameters are particle beam energy E_{beam}, lateral pencil beam position $\vec{r}_0$ and the associated particle number N. Since beam energy and lateral position are predetermined by the location of the target volume within the patient, the particle number N_j of each pencil beam remains as primary variable in the plan optimization. Typically, the number of voxels and pencil beam spots are several ten-thousands.

The optimization is performed by minimizing a cost function. Following the approach of IMPT [Lomax, 1999], the cost function of a planning target volume (PTV) optimization is stated as the quadratic sum over the difference between the calculated and the prescribed dose:

$$F_{\text{PTV}}(\vec{N}) = \sum_{i \in \text{PTV}} w_{\text{PTV}} \cdot \left(D^i_{\text{act.}}(\vec{N}) - D_{\text{presc.}}\right)^2 + \sum_{j \in \text{OARs}} w_{\text{OARs}} \cdot \Theta\left(D^j_{\text{act.}}(\vec{N}) - D_{\text{limit}}\right) \cdot \left(D^j_{\text{act.}}(\vec{N}) - D_{\text{limit}}\right)^2, \tag{1.12}$$

where w_{PTV} and w_{OARs} are weighting factors, allowing to influence the optimization result. $D^i_{\text{act.}}(\vec{N})$ is the actual dose of voxel i, which can be the physical or biological dose. $D_{\text{presc.}}$ is the dose to the tumor as prescribed by a physician and D_{limit} is the dose limit of an OAR which should ideally not be exceeded. $\Theta(D_{\text{act.}} - D_{\text{limit}})$ is the Heaviside function which is unity if $D_{\text{act.}} > D_{\text{limit}}$ and zero if $D_{\text{act.}} < D_{\text{limit}}$. By using the Heaviside function, under dosage is neglected in organs at risk (OAR).

With equation (1.12), the optimization problem can be formulated as:

$$\min \quad F_{\mathrm{PTV}}(\vec{N})\,, \tag{1.13}$$

$$\text{s. t.} \quad N_j \geq N_{\min}\ \forall\ j = 1, \ldots, p\,, \tag{1.14}$$

where p denotes the index of the last pencil beam of the raster grid [Horcicka et al., 2012]. The constraint in equation (1.14) is due to the detector system used in the dose delivery system. A minimum particle number, $N_{\min}$, is necessary per pencil beam spot for the treatment control system (TCS) to measure position and energy of the corresponding pencil beam. At GSI, the default value of $N_{\min}$ is set to 5000.

As the biological dose in equation 1.11 depends quadratically on N_j, the cost function for a biological dose optimization depends quadratically on N_j likewise. Due to this nonlinearity the cost function cannot be minimized using linear solvers. Hence, a conjugate gradient algorithm has been implemented in TRiP98 [Krämer et al., 2000; Horcicka et al., 2012].

1.6.4 Patient motion in radiotherapy

Patient motion can generate huge deviations from the planned dose distribution. In radiotherapy, both under- or over dosage can occur in the targeted volume, as well as accidental exposure of critical organs to detrimental levels of radiation. There are different types of motion which will be briefly described in the following section. Further information on methods to handle patient motion in radiotherapy can be found in the review by Langen and Jones [2001].

Typically, three main types of patient motions are distinguished: patient positioning, interfractional motion and intrafractional motion. In this thesis the focus is on respiratory motion in context with the treatment of lung cancer.

- **Patient positioning:** The position of the patient can vary between the image acquisition for treatment planning (in particle therapy typically a CT) and the treatment plan delivery. A shift occurring in the internal patient anatomy during planning and delivery could result in changes to tumor shape or position, including range changes due to different configurations of skin and fat tissue in the entry path of the particle beam. To minimize the extent of this effects, immobilization is commonly used, often accompanied with additional safety margins added to the clinical target volume (CTV) in the treatment planning phase (see section 1.6.10). Additionally, treatment centers use dedicated treatment protocols, e.g. with pre-treatment position verification using orthogonal X-ray projections or in-room CTs.

- **Interfractional motion:** Interfractional motion occurs between treatment sessions of fractionated treatment protocols, due to changes in patient anatomy. The time scale of these changes is hours or days. For lung cancer patients, this could mean tumor shrinkage or changes in lung tissue density from scarring of inflammation [Mori et al., 2009]. Furthermore, changes in the patient's breathing pattern as well as a baseline shifts of the tumor motion amplitude can occur, deteriorating the planned dose distribution [Sonke et al., 2008]. The effects of interfractional motion can be reduced by reimaging and replanning the remaining treatment.

- **Intrafractional motion:** Intrafractional motion occurrs on the smallest time scale. The motion is primarily caused by respiration or the heart beat and is on the order of seconds. Peristaltic movement of the bowel is also classified as intrafractional and occurs on the order of minutes. The amplitude of the tumor motion caused by respiration is typically on the order of mm up to a few cm [Shirato et al., 2004]. The major direction of the respiratory tumor motion is in superior-inferior (SI) direction [Seppenwoolde et al., 2002; Britton et al., 2007; Liu et al., 2007].

1.6.5 Time resolved computed tomography (4DCT)

Patient motion, especially intrafractional motion caused by respiration, can be observed with a time resolved computed tomography (4DCT). To generate a 4DCT image set, several 3DCT images of a free breathing patient are recorded, while also the respiratory motion signal is continuously recorded, using devices such as a stereoscopic camera or the ANZAI belt. During post processing, dedicated protocols are used to assign the recorded CT images to specific motion phases of the respiratory cycle. Although those CT scans are recorded over several respiratory cycles, the final 4DCT image set shows a single averaged respiration cycle only.

For 4DCTs of the lung, usually a division into 10 motion states with equal phase duration is used. The period of a respiratory cycle is the duration between two consecutive maxima or minima of the motion curve, for example between two consecutive end inhale states of the lung, as shown in figure 1.13. The typical duration of a respiratory cycle is in the range of 3 s to 5 s. In this thesis, the expressions motion phase and motion state are used synonymously.

1.6.6 Consequences of patient motion

The impact of respiratory motion on the planned dose distribution can be especially detrimental, as the scanning motion of the pencil beam occurs on a similar time scale as the period of the respiratory motion. The interference between these two movements can lead to so called interplay effects and cause hot or cold spots in den delivered dose distribution. All targets within the thorax region of a patient are affected by the respiratory motion of the lungs, and their movement during treatment can impede the delivered dose distribution.

The effects of interplay have been studied by Bert et al. [2008], for example in 2D dose measurements where a moving film dosimeter was irradiated with a homogeneous dose distribution, using scanned carbon ions. Figure 1.14 shows the resulting interplay patterns due to different motion directions. The scanning motion is horizontal in all three panels, the target motion is sinusoidal. Panel (a) shows the stationary case without any target motion. A homogeneous dose distribution is generated, depicted by the uniform blackening of the film. Panel (b) shows the interplay pattern for a vertical target motion. The zigzag shaped lines with overdose are typical for the case of orthogonal motion directions. In panel (c) the motion direction is collinear with the scanning motion. This situation usually leads to “compression” of the dose along the motion axis, here, creating cold spots on the left and right side of the target area.

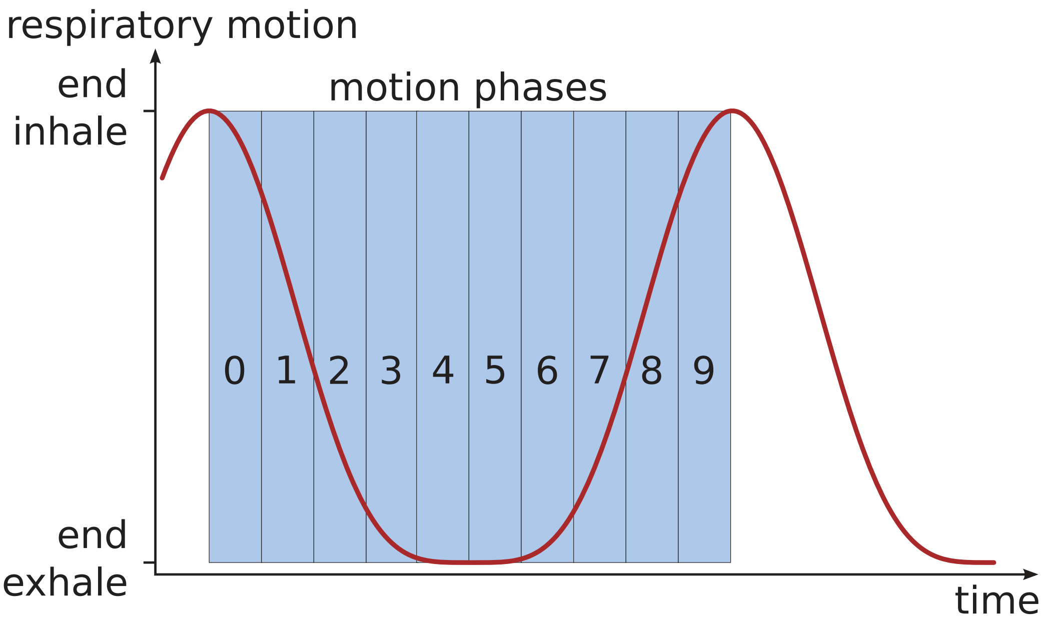

Figure 1.13.: Schematic illustration of a respiratory motion curve plotted over time. The respiratory motion period between two consecutive maxima (*end inhale* states of the lung) is typically divided in 10 motion phases of equal duration. As described by the Lujan function, the *end exhale* state of the lung is most stable in its position [Lujan et al., 1999].

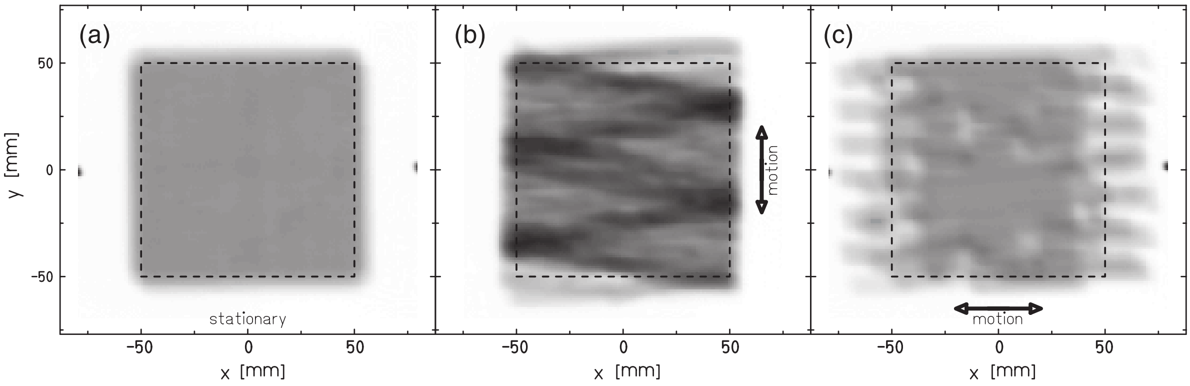

Figure 1.14.: Dose measurement with film material on static and moving targets with horizontal scanning direction. (a) is the stationary case with no target movement. (b) shows the interference dose pattern caused by interplay between the horizontal scanning and the vertical target motion, creating primarily hot spots. (c) is the interplay pattern caused by a target motion collinear to the scanning motion, creating cold spots. Figure from [Bert et al., 2008].

In case of lung cancer patients, the impact of the respiratory motion can be even more pronounced due to the density gradient between solid tumor and lung tissue. If, during respiratory motion, inaccuracy in pencil beam delivery results in tumor miss, a significant range overshoot occurs, potentially harming critical structures behind the tumor in BEV.

1.6.7 Motion mitigation

In this section, different motion mitigation techniques are presented, focusing on rescanning, gating and tracking. However, there are many other methods, like abdominal compression or active breath control, which are not presented in this thesis.

1.6.7.1 Rescanning

Rescanning, also called repainting, is a technique only used for scanned beam delivery and is based on the concept of statistical averaging [Phillips et al., 1992]. Two major strategies exist: *volumetric* rescanning and *slice-by-slice* rescanning. For both methods, the particle numbers of each beam spot in an IES are divided by the number N of desired rescans. For volumetric rescanning, the entire tumor volume is irradiated N times, while for slice-by-slice rescanning, each IES is irradiated N times. Since interplay patterns depend on amplitude, period and starting phase of the respiratory motion, the basic assumption is, that the exact same interplay pattern is unlikely to be generated in consecutive breathing cycles. Hence, the superposition of N different interplay patterns will homogenize the dose distribution. Figure 1.15 shows the effects of increasing the number of rescans on the dose homogeneity of a 2D dose measurements using film material. The maximum number of rescans is limited by the detector system used in the dose delivery system. At GSI, as described in section 1.6.3, at least 5000 particles are required for the detector system to measure a beam spot's energy and lateral position.

Several different rescanning strategies have been proposed and tested to address the inherent limitations of rescanning. *Random-delay rescanning* introduces a random time delay between applied rescans to avoid potential unfavorable temporal correlations between the scanning and respiratory motion [Seco et al., 2009; Rietzel and Bert, 2010]. During *Breath-sampled rescanning* [Seco et al., 2009] and *phase-controlled rescanning* [Furukawa et al., 2010] the rescans are equally distributed over the breathing cycle to reduce the number of rescans and increase the robustness. Phase-controlled rescanning is in clinical use at NIRS in combination with beam gating [Ebner et al., 2017].

Compared to beam gating or beam tracking, online motion detection is generally not required for rescanning. However, to ensure that the tumor remains within the volume at any motion state within the respiratory cycle, it is necessary to increase the treatment volume. This can result in significant increases of OAR or normal tissue doses, representing the major disadvantage of rescanning.

1.6.7.2 Gating

The premise behind gating is to deliver the beam only when the moving target enters a predfined *gating window* [Minohara et al., 2000; Lu et al., 2006]. For respiratory motion, the end-exhale portion of the motion phase is typically chosen, as it is the most stable in its position [Lujan et al., 1999]. Motion monitoring is necessary for gating to signal the control system for when the target is within the gating window. When the signal is sent, the control system allows the treatment delivery. There is an additional challenge for synchrotrons, which do not operate in a continuous mode. Instead, synchrotrons deliver pulsed irradiation in spill cycles. So, the target may be within the gating window, while the synchrotron

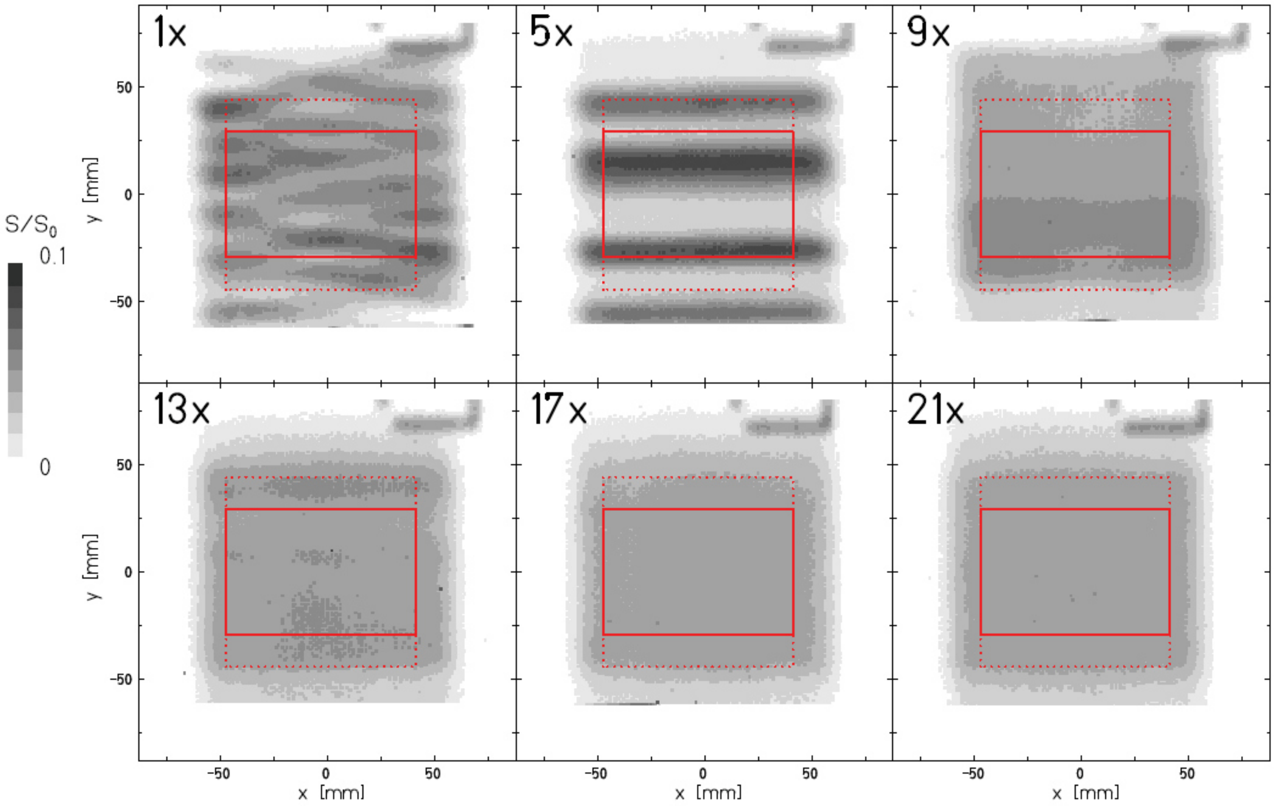

Figure 1.15.: Dose measurement with film material on a vertically moving target with horizontal scanning direction. The interference between target and scanning motion causes an interplay pattern with characteristic hot and cold spots. Increasing number of rescans mitigates the interplay pattern by super position of different interplay patterns. This can be described as "statistical averaging". Figure from [Bert et al., 2009].

is between spills, further reducing the "effective gating window", or the time the delivery system can treat the tumor. Figure 1.16 shows an exemplary motion monitoring signal depicted over time with a chosen gating window, showing the resulting extracted beam intensity, determined by the temporal overlap with the beam availability of the synchrotron cycle.

It has been shown that optimization of the synchrotron cycle is possible and can considerably reduces increases in treatment time [Tsunashima et al., 2008]. The use of knock-out extraction with RF cavities, has enabled the extraction of multiple beam gates per synchrotron pulse, which further decreases treatment time with the beam gating method. This strategy has been clinically implemented at several facilities, including at HIT [Heeg et al., 2004]. Nevertheless, a non-negligible residual motion of the target can still persist. Depending on the chosen temporal size of the gating window, it can be in the order of several millimeters, yet causing interplay.

Beam gating and fast rescanning can also be combined as done at NIRS for a small number of liver and lung patients [Ebner et al., 2017]. This was made possible through the latest revision of the HIMAC accelerator, providing fast and markerless pencil beam rescanning and fast changes of particle energy [Mizushima et al., 2017].

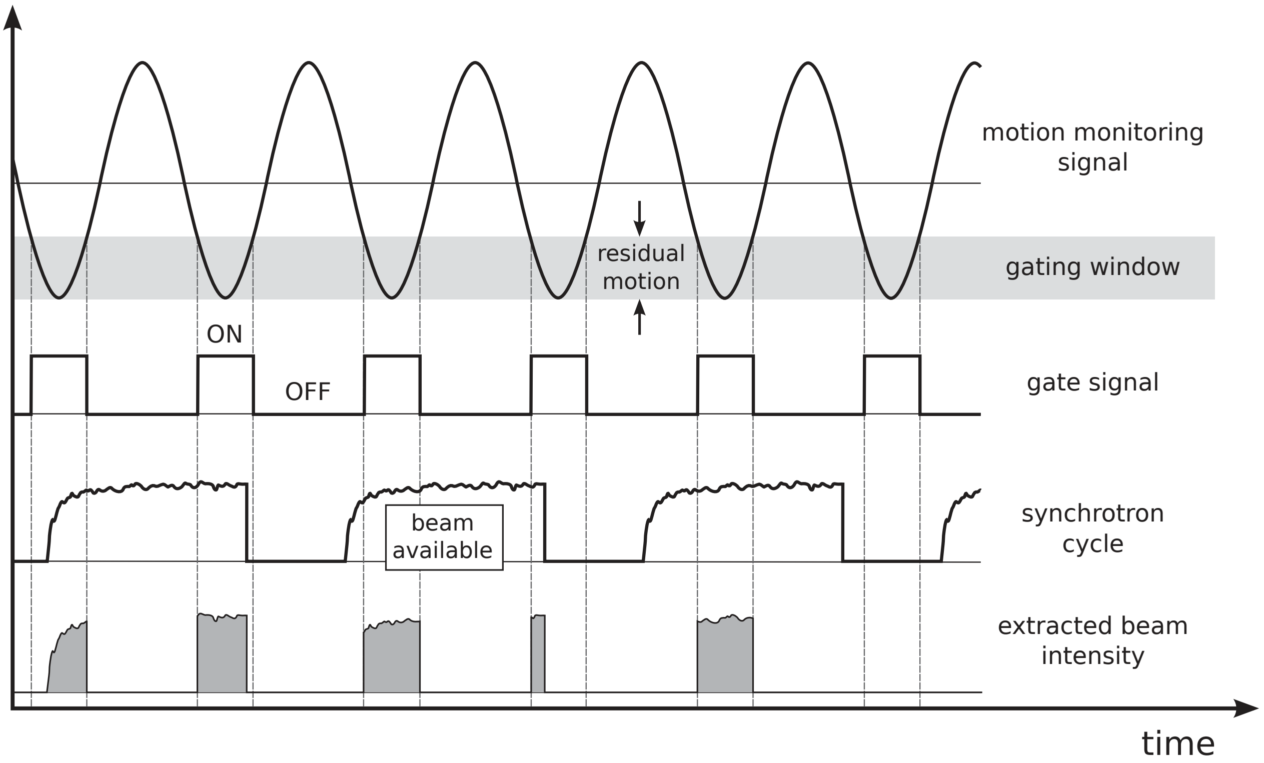

Figure 1.16.: Simplified diagram of the gating delivery mode with a synchrotron accelerator. The logical gate signal is generated by applying the gating window to the motion monitoring signal. Irradiation is only possible if the gate signal is active during beam availability. The amount of residual tumor motion depends on the gating window size. Figure from [Richter, 2012].

1.6.7.3 Tracking

Tumor tracking is a combination of real-time motion monitoring with online corrections of the tumor location from the original treatment plan due to patient motion. The idea was originally proposed for IMRT [Keall et al., 2001] and is now used routinely in clinics, e.g. for X-ray radiosurgery with the robotic Cyberknife Synchrony system (Accuray Inc., Sunnyvale, CA, USA) [Brown et al., 2007; Kilby et al., 2010].

At GSI, a full tracking system has been implemented for the scanned delivery of carbon ion beams. For the compensation of longitudinal range changes, a fast modulation of particle energies is required. Fast energy modulation is provided by a system of opposing PMMA wedges mounted on a linear step-motor [Weber et al., 2000]. For lateral compensation, the already existing scanning magnets were used, as the schematic illustration shows in figure 1.17. The correction of patient movement was based on pre-calculated look-up tables containing the compensation parameters and guided by a motion monitoring signal. Important requirements for beam tracking were accurate 4DCT image data and a fast and precise motion monitoring unit for measuring the movement of internal organs. Dose measurements and technical tests have shown the feasibility and high precision of the system [Bert and Rietzel, 2007; Bert et al., 2010; Saito et al., 2009]. Besides the technical challenges in general, especially the longitudinal beam tracking suffers from the finite size of the pencil beam diameter: high density gradients within the patient geometry can cause edge effect deteriorating the adapted dose distribution. However, beam tracking is not yet clinically implemented primarily due to the complexity of the whole system.

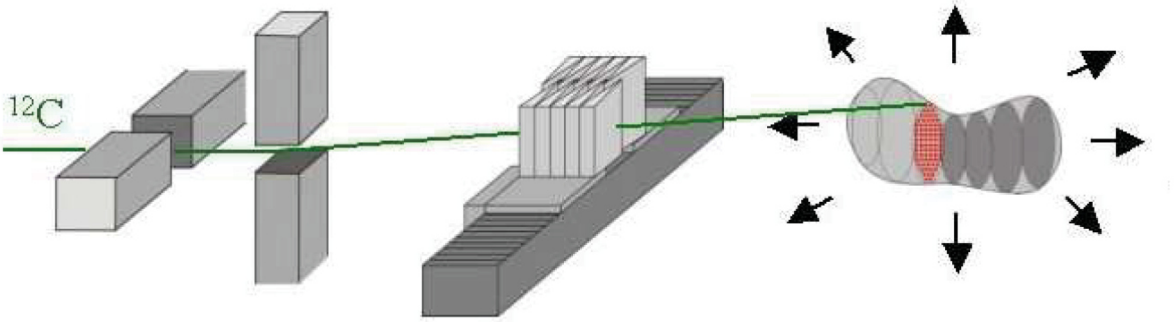

Figure 1.17.: Schematic illustration of the tracking system. A motion monitoring unit (not depicted) is necessary to determine the correction parameters for the control system. Lateral offsets in BEV are compensated by a correction of the position of the scanning magnets. Range offsets are compensated by a range modulator consisting of PMMA wedges mounted on a linear step-motor in front of the patient. In its nominal position, the wedges already overlap to enable also range reductions. Figure from [Groezinger, 2004].

1.6.8 4D treatment planning

The goal of 4D treatment planning (4DTP) is to account for organ motion already during treatment planning, to eventually increase the dose to a moving tumor while sparing normal tissue at the same time. Compared to photon therapy, there is a greater challenge for 4DTP with charged particles, since scanned ion beams are much more prone to motion induced errors like range changes or interplay (see section 1.6.6). As proposed by Keall et al. [2004], 4DTP must account for temporal changes in patient's anatomy during the imaging, treatment planning and treatment delivery of radio therapy. In particle therapy, this is especially important for single fractionated treatments, since tumor miss risks high doses to normal tissue. Despite the risk, dose escalation can significantly improve local tumor control rates, in particular for NSCLC [Rosenzweig et al., 2005; Kong et al., 2005], and is therefore desirable for treating resistant lung cancers. The occurrence of radiation-induced normal tissue complications also depends significantly on the OAR doses. The probability for treatment side effects such as acute esophagus toxicity depends significantly on the volume of the esophagus receiving more than 35 Gy [Belderbos et al., 2005].

4D dose calculation

4D dose calculation allows for the quantification of dose heterogeneities caused by patient motion, including interplay effects. In the field of particle therapy, different strategies to calculate 4D dose distributions, exploiting deformable image registration (see section 1.6.9) and 4DCTs, are used. In the case of scanned ions, the temporal correlations between the time-structure of the sequential plan delivery and the patient motion have to be accounted for [Bert and Rietzel, 2007; Paganetti et al., 2004]. Currently, there are two major approaches for calculating 4D dose distribution: transformation of the individual dose contribution of each motion phase to a common reference frame [Bert and Rietzel, 2007] and deformation of the dose grid, as implemented into the GSI TPS [Gemmel et al., 2011]. The latter approach is advantageous for heavy ion therapy, since it enables biological dose calculation. For validation of this algorithm, a dedicated phantom has been built and was successfully used in measurements. A dose delivery simulation (DSim) tool used for temporal correlation between target motion and beam delivery sequence was revised, now capable of simulating synchrotron timings from GSI, HIT, MIT [Richter, 2012] and soon CNAO, Italy.

4D optimization

In 4D treatment planning, 4D optimization is used to account for temporal changes patient's anatomy due to patient motion. The 4D optimization strategies rely on the usage of the motion states of a 4DCT. At GSI, the 4D treatment planning system is an expanded version of TRiP98, called TRiP4D. A detailed description is given by Richter et al. [Richter, 2012; Richter et al., 2013].

Several 4D optimization strategies have been implemented into TRiP4D [Richter, 2012; Richter et al., 2013; Graeff et al., 2012, 2013, 2014; Graeff, 2014]. More details on the 4D optimization algorithms used in this thesis, are given in the first sections of chapters 3 and 4.

1.6.9 Image registration

By using different imaging modalities (CT, MRI, PET, etc.) or several images of the same modality at different times (4D-CT, 4D-MRI, 4D ultra sound), the temporal changes of patient anatomy can be observed. To gain processable data of patient or organ motion, it is necessary to generate a spatial correlation between image sets. This can be done by using image registration techniques. For the registration, two image sets are required: a fixed image set (as reference) and a moving image set. The image registration process results in a voxel-to-voxel deformation map, which is a map of vectors originating in the moving image voxel and are pointing to the corresponding fixed image voxel. The two associated points x and x' in the fixed and the moving image, respectively, are represented in the following formula:

$$x' = x + \mathrm{u}_{ri}(x), \tag{1.15}$$

where r indicates the reference state and i, the moving state. The deformation map is represented as a vector field u_{ri}. The resulting vector field can be used for assessing quantities like motion amplitude or for 4D dose calculation [Richter, 2012]. Figure 1.18 shows image registration applied on an axial CT image of a patient's thorax. Applying the deformation map to the moving image creates a warped image. Ideally, the warped image is as close to the fixed image as possible.

Two main groups of transformations exist: The first group includes linear or rigid transformations which describe translation or rotation by using 4 × 4 transformations matrices, affecting a CT image globally. Typically, these transformations are used to describe non-complex motion of simple setups such as dose simulations in water phantoms. The second group uses vector fields from deformable transformations also capable of describing complex organ motion such as deformation (e.g. changing volume of the lung lobe) or gliding motion between organs (e.g. between the chest wall and lung). There is a variety of registration algorithms which are capable of generating these vector fields. The algorithms have a high degree of complexity and further information is available [Hill et al., 2001; Brock et al.,

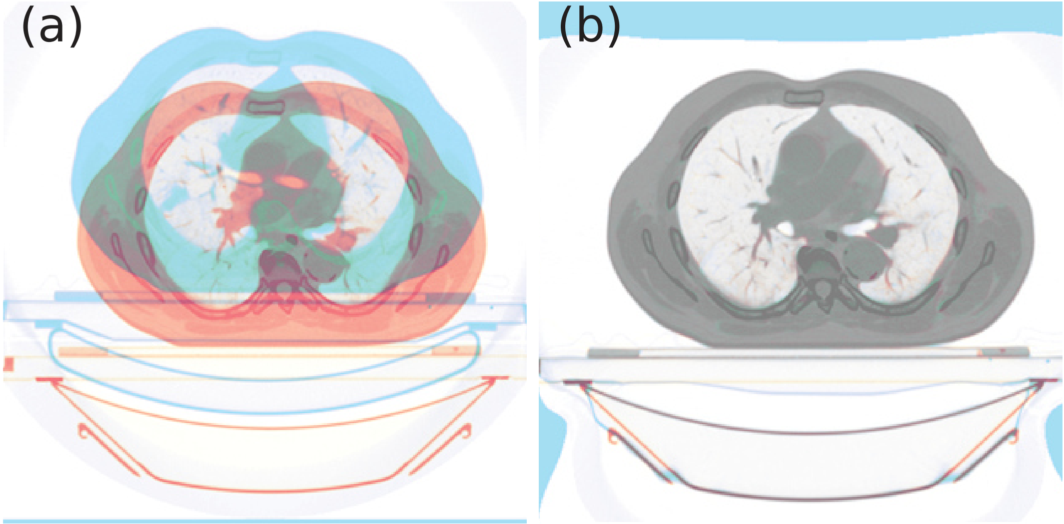

Figure 1.18.: Image registration for axial CT image of a patient's thorax. Panel (a) shows overlap of a fixed and a moving image and panel (b) the fixed and warped image after registration. Using inverse colors in both CTs will result in gray colors where both images overlap perfectly. Figure courtesy Kristjan Anderle.

2006; Rietzel and Chen, 2006]. Brock et al. have conducted a comprehensive multi-institutional study on the accuracy of image registration algorithms. Despite large discrepancies, the majority of registration algorithms have an accuracy on the order of typical CT voxel sizes (1 mm to 2.5 mm) encouraging the further use of image registration to improve treatment planning and delivery [Brock, 2010]. Despite the high level of accuracy, dedicated quality assurance protocol is still recommended [Anderle, 2016].

1.6.10 Treatment volumes and margins

Safety margins are already in use for treatment planning in radiotherapy with photons. The basic premise is to increase robustness of the plan by increasing the treatment volume. This accounts for slight misalignment during patient setup and marginal uncertainties to patient movement during treatment. The common definitions of treatment volumes as recommended by the ICRU are stated below [ICRU, 1993, 1999].

- **Gross Tumor Volume:** The GTV is the gross palpable or visible/demonstrable extent and location of malignant growth.

- **Clinical Target Volume:** The CTV is a tissue volume that contains a demonstrable GTV and/or subclinical microscopic malignant disease, which has to be eliminated. This volume thus has to be treated adequately in order to achieve the aim of therapy, cure or palliation.

- **Planned Target Volume:** The PTV is a geometrical concept and it is defined to select an appropriate beam size and beam arrangements, taking into consideration the net effect of all the possible geometrical variations, in order to ensure that the prescribed dose is actually absorbed in the CTV.

- **Internal Target Volume:** The ITV is the margin that must be added to the CTV to compensate for expected physio-logical movements and variations in size, shape and position of the CTV during therapy.
- **Organs At Risk:** OAR are normal tissues whose radiation sensitivity may significantly influence treatment planning and/or prescribed dose.

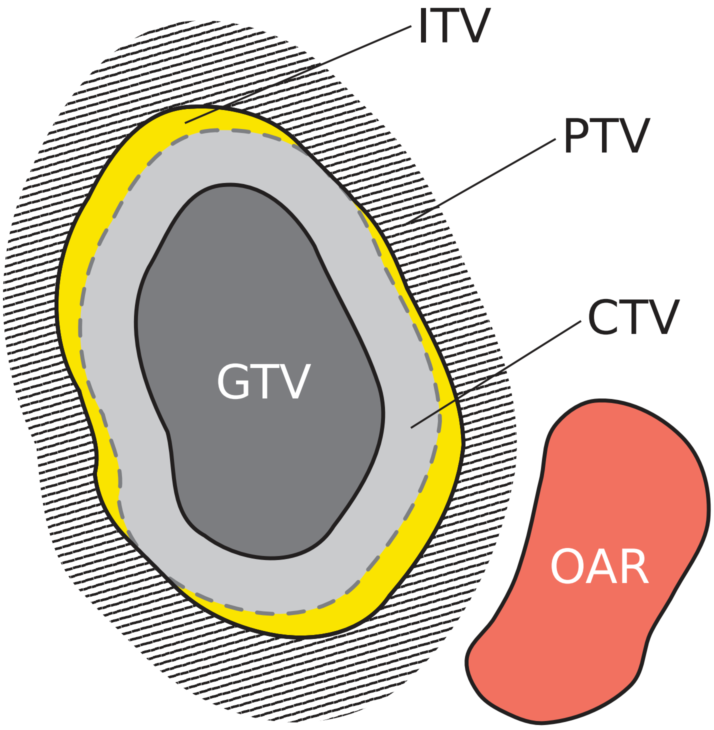

Figure 1.19.: Nomenclature of volumes used in treatment planning, from inside out: gross tumor volume (GTV), clinical target volume (CTV), internal target volume (ITV) and planning target volume (PTV). Critical structures are abbreviated as organs at risk (OAR). Figure from [Richter, 2012].

An illustration of a typical configuration of treatment volumes in case of a moving tumor is depicted in figure 1.19. The CTV surrounds the GTV, including possible microscopic spread of tumor tissue. CTV and GTV are typically contoured by experienced physicians. The ITV is generated by the union of all CTVs in all motion phases. The PTV margins account for geometrical uncertainties and the sparing of critical structures (OAR).

Due to the high spatial precision of the Bragg peak of protons or heavy ions, treatment plans are more prone to errors during treatment delivery. Choosing appropriate safety margins is important and of high relevance for particle therapy; however, safety margins should not be increased without restriction. Assuming a spherical target with a diameter of 30 mm, additional PTV safety margins of 3 mm would increase the treated volume by about 73 %. Since this additional volume is, in most cases, normal tissue, extension of the margins must be carefully chosen. The topic of safety margins in robust optimization is further discussed in chapters 2 and 3.

1.7 Summary

An introduction on lung cancer was given, stating the poor prognosis of the disease, potential risk factor such as tobacco consumption in particular, and giving an overview about non-small cell lung cancer (NSCLC) as the lung cancer subgroup which will be primarily addressed in this thesis. Further, the rationale for the clinical application of ion beams was given and the physical and biological properties of ion beams were introduced. The second half of this chapter looked at treatment planning with ions, also presenting the two concepts of treatment delivery. Further, the implications of patient motion were addressed, where the raster scanning approach is especially prone to dosimetric errors due to moving targets. In the following section, mitigation strategies to overcome the issue of respiratory patient motion were presented, including rescanning, beam gating and beam tracking. In the following section, 4D treatment planning was introduced, describing the potential benefits and requirements using 4DCTs and image registration for treatment planning. Details on the implementation of robust optimization methods for 3D and 4D treatment plan optimization will be introduced and discussed in the upcoming three chapters.

2 Introduction to robust optimization

Contents

2.1 Introduction

In contrast to photon therapy, particle therapy is much more prone to range uncertainties due to the high precision of the energy deposition provided by the Bragg peak. While traversing heterogeneous tissue, unplanned density variations can alter the range of particles on the order of several millimeters.

Range or setup uncertainties can eventually lead to a deterioration of the delivered dose distribution, in particular for multiple field optimization (MFO) when a mismatch of inter field dose gradients occurs. This is illustrated in figure 2.1, where the increasing color gradients represent internal dose gradients. These dose gradients can for example occur in situations, where a critical organ which is in close proximity to the target volume needs to be spared. In the depicted example, the dose deterioration is caused by a range undershoot which can be due to a higher CT density of the traversed tissue.

The topic of accounting for range uncertainties with robust optimization was first addressed by Unkelbach et al. [2007]. He proposed a probabilistic approach which handles range uncertainties as a random variable. The cost function becomes a random variable too and the expectation value is then optimized. For protons, the resulting robust cost function depends linearly on the particle vector $\vec{N}$ and it can be minimized using linear optimizing algorithms.

As described in section 1.6.2, biological dose calculation for heavy ions relies on variable RBE. Due to the variable RBE, the biological dose depends nonlinearly on $\vec{N}$ (see equation (1.11)). For the optimization of a biological dose, this nonlinearity is passed on to the cost function in equation (1.12). To minimize this "biological" cost function, which now also depends nonlinearly on $\vec{N}$, a nonlinear solver

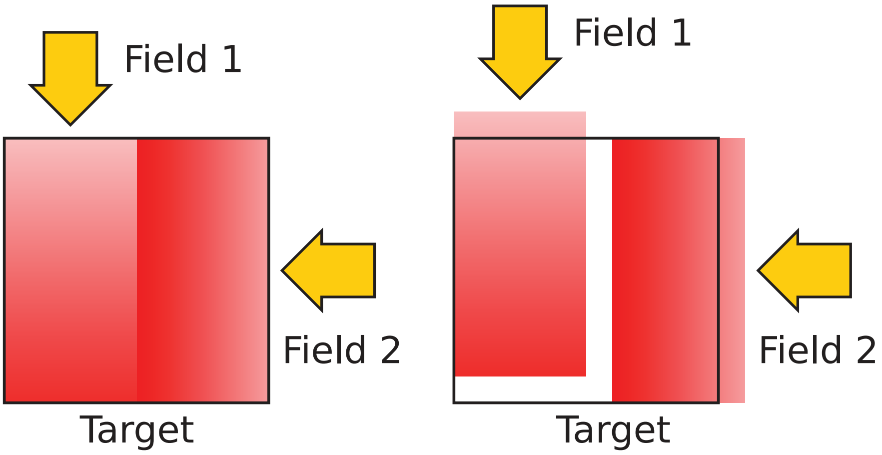

Figure 2.1.: Sketch of target irradiated by two orthogonal IMPT fields. Color gradients illustrate internal dose gradients due to IMPT. Left: both fields are irradiated exactly as planned. Right: the dose distribution is deteriorated because of reduced particle ranges. Figure adapted from [Graeff et al., 2012].

is required. Therefore, TRiP98 uses the implementation of a conjugate gradient algorithm [Krämer et al., 2000; Horcicka et al., 2012]. In contrast to robust optimization of proton treatment plans, the probabilistic approach is less suited for robust optimization of carbon treatment plans.

2.2 Worst-case method

The *worst-case* approach for the robust optimization of a cost function described by Pflugfelder et al. [2008] demonstrates a method which is more suitable for the nonlinear biological dose calculation. Besides the nominal scenario, the robust cost function $\tilde{F}(\vec{N})$ includes an additional term for a worst-case dose scenario:

$$\tilde{F}(\vec{N}) = F(D_{\text{nom}}(\vec{N})) + p_{\text{worst case}} \cdot F(D_{\text{worst case}}(\vec{N})), \tag{2.1}$$

which is steered by a worst-case penalty weight p_w. For $p_{\text{worst case}} = 0$ the original nominal case is obtained. The worst-case dose distribution $D_{\text{worst case}}$ is calculated by initially assessing the expected range uncertainties for all pencil beams included. Since it is most likely that the pencil beams and their range uncertainties are not independent, a minimal and maximal range uncertainty is estimated [Pflugfelder et al., 2008]. This will result in two possible dose distributions. In the proposed approach of Pflugfelder et al., setup uncertainties are accounted for by shifting the dose distribution in lateral directions in BEV. For the worst-case approach two simplifications are made: the laterally shifted dose distributions are calculated for only the nominal pencil beam range and dose distributions for minimal and maximal range are considered for the unshifted nominal case only. This results in seven different dose distributions.

If the reference frame for the setup uncertainty is changed from BEV to the patient system, this results in six possible scenarios, which are described in section 2.2.0.1.

In this study an approach similar to the one proposed by Liu et al. [2012] has been implemented. This methods differs from Pflugfelder et al. in the less prominent role of the nominal case as it is handled as on of the possible uncertainty scenarios only.

2.2.0.1 Modeling of setup uncertainty

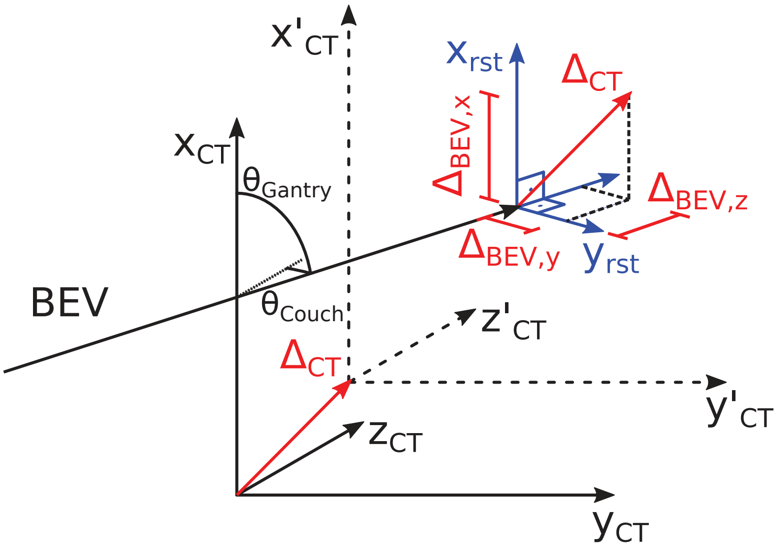

Figure 2.2.: Projection Δ_{BEV} of the setup error Δ_{CT} onto the coordinate system of the BEV system of an arbitrary raster point resulting from shifting the patient during setup. Here the Δ_{CT} consists of a x and y component in the CT system.

Patient setup errors are modeled by shifting the patient's isocenter in the direction of the major anatomical axis (SI, anterior-posterior (AP) and left-right (LR) direction) by a few millimeters.Since a field specific set of pencil beam spots of a treatment plan is optimized with water equivalent path lengths (WEPLs), the shift Δ_{CT} in the CT system is transformed to this coordinate system (see figure 2.2). In the WEPL system, also referred to as BEV, the transformed shift Δ_{BEV} can be divided into two lateral parts $\Delta_{BEV,x}$ and $\Delta_{BEV,y}$ as well as a part collinear to the BEV axis, $\Delta_{BEV,z}$.

This is in contrast to the method by Pflugfelder et al. [2008], where the patient setup shifts are directly applied as lateral shifts in the WEPL coordinate system and no collinear shift is applied. The rationale is that, due to the high difference between mass density of air and of human tissue (a factor of about 1000), the particle ranges are only marginally affected by traversing an additional distance through a layer of air.However, the approach of Pflugfelder et al. ignores that the setup error originally occurs in the patient coordinate system and, hence, overestimates the resulting setup errors in the BEV system. This can be solved by only accounting for the relevant projections of the setup error in the BEV system as shown in figure 2.2. In case of collinearity between the field angle and one of the major anatomical axes, the orthogonal projection of the shift becomes zero and effectively turns the respective setup error scenario into the nominal one. For all other field angles, the described approach yields the relevant shift in the WEPL system.

2.2.0.2 Modeling of range uncertainty

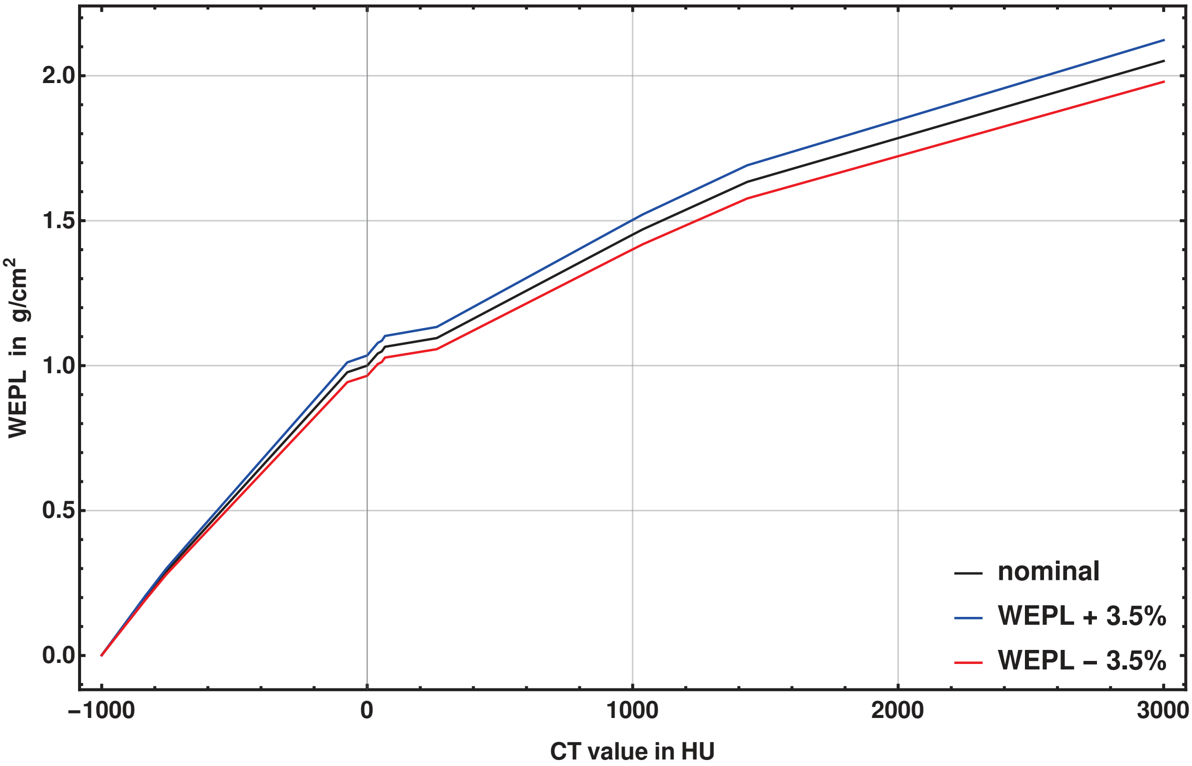

Figure 2.3.: HLUT used for translation of geometric length to WEPL space. Black: nominal HLUT, blue: WEPL + 3.5 %, red: WEPL - 3.5 %.

A straightforward approach to globally shift the particle ranges of a treatment plan is to scale the Hounsfield unit (HU) values of a CT cube. This will change the tissue density of the patient and inversely change the particle ranges.

Since the particle numbers for all pencil beams in a treatment plan are optimized in the space of WEPLs, it is also possible to scale the function which translates the CT coordinates into WEPL space. Compared to the approach of storing two additional CT cubes with scaled HU values in addition to the nominal CT cube, no additional memory is needed. To convert geometrical distances into WEPL space, a simple Hounsfield unit lookup table (HLUT) is required. The HLUT correlates the HU values of a CT with its equivalent path length in water. The WEPL for water, which corresponds to a HU value of 0, is normalized to 1.0. Hence, by reading the CT value of a traversed voxel, the geometrical intersection length between a pencil beam and the voxel can be translated to the WEPL space by scaling the geometrical distance with the corresponding scaling factor from the HLUT. Since the HU values depend on the CT machine, the HLUT has to be experimentally determined by evaluating CT images with a variety of tissue equivalent materials. The nominal and the shifted HLUTs are shown in figure 2.3.

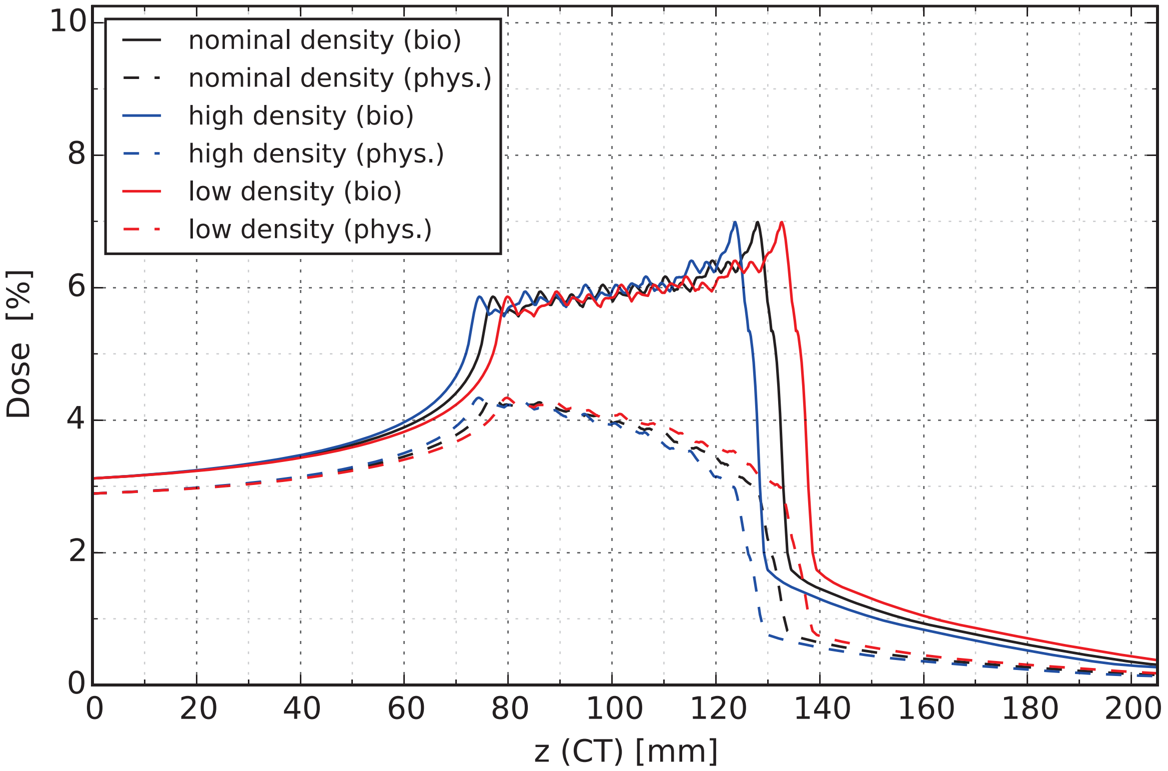

Figure 2.4.: Spread out Bragg peak along the BEV axis for one of two opposing fields irradiating a sphere in water. Solid lines represent biological dose and dashed lines represent physical dose. SOBPs are shown for three ranges: nominal range (black lines), reduced range with CT density increased by 3.5 % (blue lines) and increased range with CT density decreased by 3.5 % (blue lines).

The impact on the range of a SOBP in BEV is shown in figure 2.4 for one of two opposing fields irradiating a sphere in a water phantom with a diameter of 50 mm. The biological and physical dose is plotted over the z-direction of the raster system in CT coordinates in mm. Shifting the WEPL values by 3.5 % increases the CT density which results in a shortened range (solid blue line), whereas shifting by −3.5 % yields a prolonged range (solid red line) due to the decreased CT density.

WEPL shift [%]	80% range [mm]	Δ_{range} in [mm]	$\Delta_{\text{range rel}}$ in [%]
-10.0	144.8	14.5	11.1
-3.5	135.1	4.7	3.6
nominal	130.3	-	-
3.5	125.9	4.4	3.4
10.0	118.5	11.8	9.1

Table 2.1.: 80 % ranges and deltas to nominal range of SOBPs shifted by ±3.5 % (depicted in figure 2.4) and ±10.0 %.

Table 2.1 presents the range shifts due to scaling the CT density by ±3.5 % and ±10.0 % for the above mentioned example of a sphere in water. The table states distal 80 % ranges, and the absolute and relative differences between the nominal range and the two scenarios with higher and lower CT density. Shifting the WEPL values of the HLUT by ±3.5 % results in a comparable range shift of approximately

$\mp 3.5\,\%$. It's important to note that the relationship between WEPL and range shift is not linear, due to the Bethe-Bloch equation. For larger shifts, such as a WEPL reduction by $-10\,\%$ the range is prolonged by $11.1\,\%$. However, in the desired order of a few millimeters, the difference in range shifts between scenarios with low and high density is negligible.

2.2.1 Implementation of the robust optimization algorithm

Robust field setup

Whether for single or multiple field robust optimization, the setup procedure per treatment field is identical. Figure 2.5 summarizes the process of the field setup for robust optimization. First, the same parameters as for a "normal" field setup are used, namely couch angle, gantry angle, isocenter, target contours, pencil beam width, pencil beam grid spacing, thickness of ripple filter, etc. Here, the original implementation of the field setup algorithm in TRiP4D is used, which results in an initial RST grid for the nominal case. The target volume is transformed to the WEPL space in reference to the BEV axis which is determined by couch angle, gantry angle and the patient's isocenter. To find the proximal and distal limits of the target volume, CT⟷RST intersections are calculated using a ray-tracing algorithm. During the ray-tracing process, the geometrical intersections of the pencil beams traversing the voxels of a CT cube are calculated. By scaling the geometrical distance with the WEPL, which corresponds to the HU value of the intersected CT voxel, the range in water can be estimated. The transformed volume is divided in IES determined by the thickness of the ripple filter and the available primary particle energies. The slice with the largest extension is used as a starting point for the remaining slices. The resulting three dimensional RST grid is cubical in shape and contains all necessary pencil beam spots to cover the target volume.

As mentioned in section 2.2.0.1, there are two primary input parameters for robust optimization: the patient setup uncertainty (in mm) and the range uncertainty (in percent). From here, nine uncertainty scenarios are initialized. Since changing the CT density affects the particle ranges, the corresponding shifted Hounsfield lookup tables are also stored, as well as the patient-to-gantry and gantry-to-patient transformation matrices which are changed when shifting the patient's isocenter.

The goal of the robust field setup is to further extend the initial RST grid to contain all possible pencil beam spots resulting from the 9 uncertainty scenarios. To achieve this, a loop over the uncertainty scenarios is repeated to find the lateral, proximal and distal limits of the target volume. This process can result in additional proximal and distal IES; however, the final result is an extended RST grid (see figure 2.5).

Initially, all RST points of the final cubical RST grid are valid beam spots and their particle numbers would be optimized to deliver the planned target dose to the entire volume of the RST grid. Typically, tumors are more or less of spherical shape and beam spots which are outside of the treatment volume need to be discarded. In the original algorithm this is done looping all RST points and recheck, whether they are inside of the treatment volume. Since the position of the treatment volume changes within the patient for different uncertainty scenarios, an additional loop over all scenarios is required for each beam spot from the final RST grid.

In case of the robust field setup, the order of these two loops is commutable. Hence, the loop over the uncertainty scenarios can be performed first. The target contours are shifted, corresponding to the

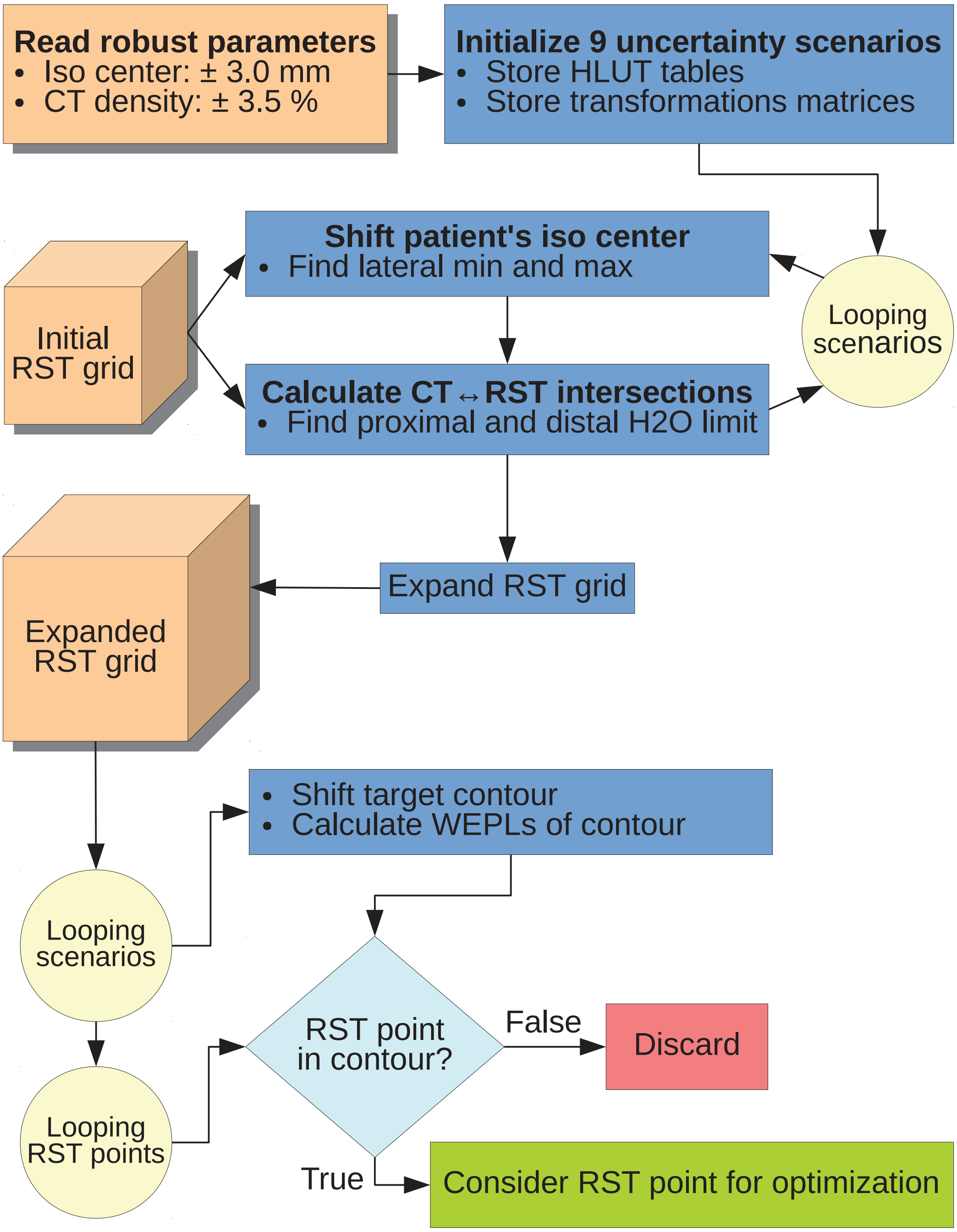

Figure 2.5.: The flowchart schematically shows the setup of a RST grid for a field used in robust optimization. Inputs are the basic field parameters like couch angle, gantry angle, isocenter, target contours, pencil beam width, pencil beam grid spacing, thickness of ripple filter, etc. These are not explicitly shown in the chart, but the resulting initial, nominal RST grid. Further inputs are the uncertainty parameters for the robust optimization e.g. ±3.0 mm for patient setup error and ±3.5 % shift of CT density to model range uncertainties.

robust parameters of each scenario and the WEPLs are recalculated. This is followed by the loop over all RST points, rechecking if the RST point is within the target contours. This procedure ensures, that all relevant RST points are considered for the robust optimization.

Robust optimization

The two basic inputs for the subsequent robust optimization are the extended RST grid per treatment field as described in the previous section, and the CT image. Both inputs are needed to calculate the entries of the field dose correlation (FDC) matrices for each uncertainty scenario. For each scenario, the CT voxels corresponding to the shifted target volume are correlated to the dose contribution of each field. The lateral and depth dose contributions result from the pencil beam model used for physical and biological dose calculation, which has been presented in sections 1.6.1 and 1.6.2. Since the lateral and longitudinal shifting of the target volume within the CT image addresses different voxel, the resulting 9 FDC matrices are also differing, describing different dose distributions. In figure 2.6 the setup of the FDC matrices is shown as a flowchart. The FDC matrices are schematically visualized as two dimensional false color plot. As described in section 1.6.1, the dose of an voxel i results of the scalar product between the particle vector $\vec{N}$ and the *i-th* line of the FDC matrix. For the robust optimization, there are nine different dose values for each voxel (see also equations (1.8),(1.9) and (1.11)).

An optimal solution for the particle numbers for each pencil beam spot N_j (within the particle number vector $\vec{N}$) is found by minimizing the cost functions presented in the following sections 2.2.2 and 2.2.3. As described in section 1.6.3 a conjugate gradient algorithm is used for solving the minimization problem. For determination of step width and search direction in each iteration of the conjugate gradient algorithm, the calculation of the particle vector gradient $\nabla F(\vec{N})$ is necessary, as described explicitly in Horcicka [2011]. Since this gradient has contributions of each voxel considered in the optimization, these contributions can differ depending on the uncertainty scenario chosen by the worst case optimization algorithm. As the entries of FDC matrix are used for the calculation of this gradient, all FDC matrices have to be held in memory over the complete course of the optimization, which increases the amount of memory required for the execution of a 3D robust optimization by a factor of 9. A detailed description of the used conjugate gradient algorithm can be found in Horcicka [2011].

2.2.2 Difference between conventional and robust cost function

The robust cost function used in this thesis, based on the worst-case method proposed by Liu et al. [2012], is defined as

$$\begin{aligned} F_{\text{Robust}}(\vec{N}) = & \sum_{i \in \text{CTV}} w_{\text{CTV}} \cdot \left(\min_{\{k \in K_{\text{Scen.}}\}} \left[D^{i}_{\text{act.}}(\vec{N},k) \right] - D_{\text{presc.}} \right)^2 \\ & + \sum_{j \in \text{OARs}} w_{\text{OARs}} \cdot \Theta\left(\max_{\{k \in K_{\text{Scen.}}\}} \left[D^{j}_{\text{act.}}(\vec{N},k) \right] - D_{\text{limit}} \right) \cdot \left(\max_{\{k \in K_{\text{Scen.}}\}} \left[D^{j}_{\text{act.}}(\vec{N},k) \right] - D_{\text{limit}} \right)^2 , \end{aligned} \tag{2.2}$$

where the minimum and maximum dose is taken from a set of $K_{\text{Scen.}}$ possible dose scenarios per voxel. In this thesis, 9 uncertainty scenarios are used for lateral and longitudinal displacement of the target volume, as described in section 2.2.0.1. The Heaviside function, $\Theta(D_{\text{act.}} - D_{\text{limit}})$, is unity when $D_{\text{act.}} > D_{\text{limit}}$ and zero when $D_{\text{act.}} < D_{\text{limit}}$. By using the Heaviside function, under dosage is neglected in the organs at risk (OAR).

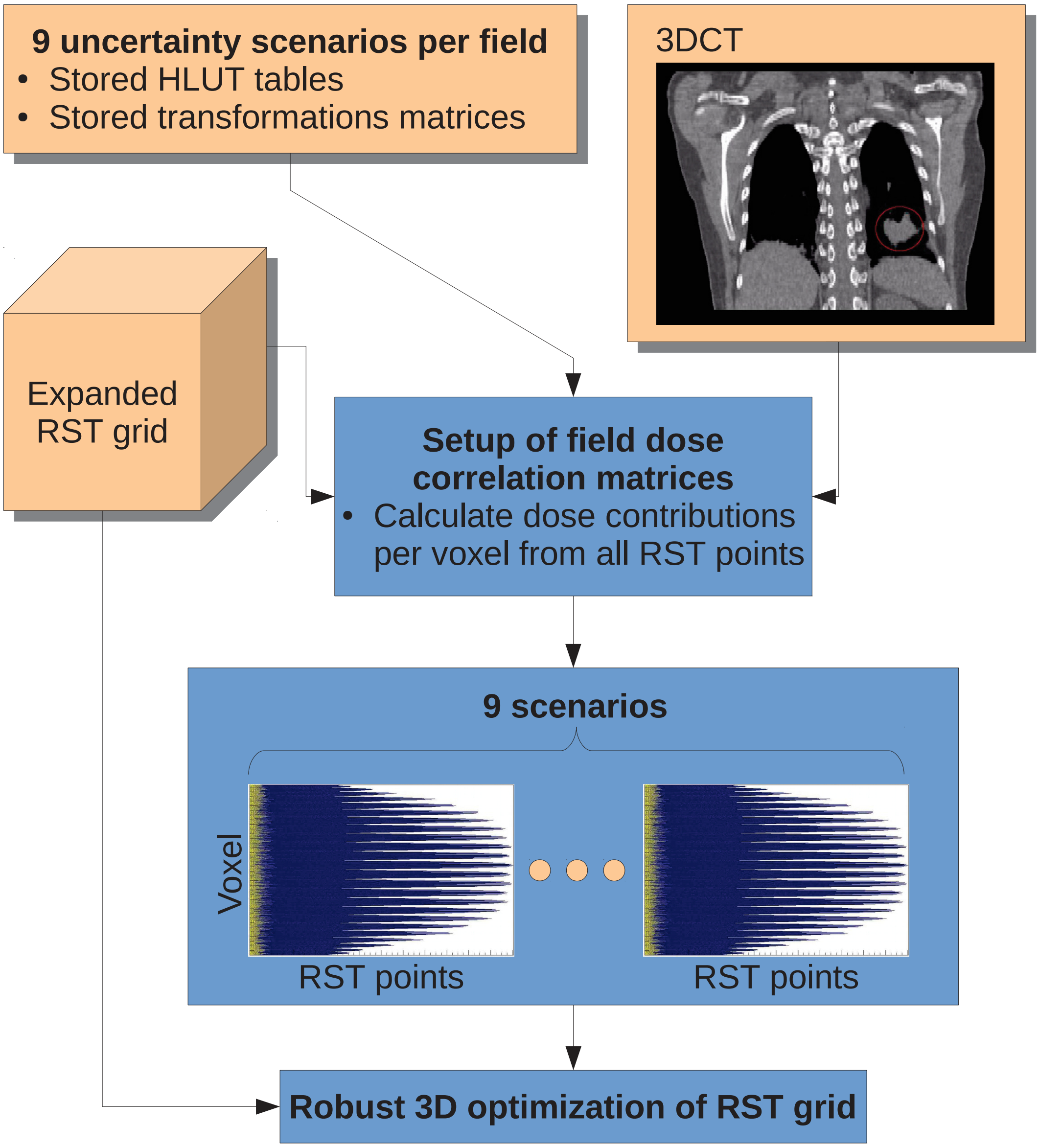

Figure 2.6.: The flowchart schematically shows the setup of field dose correlations matrices for the robust 3D optimization. Based on the 9 uncertainty scenarios (from fig. 2.5) and the field dose correlations (FDC) for each pencil beam are calculated and stored. For this approach this results in 9 FDC matrices from which different dose scenarios are calculated. Eventually, the expanded RST grid is then robustly optimized.

Choosing the actual dose, $D_{\mathrm{act.}}$, from a set of $K_{\mathrm{Scen.}}$ possible dose scenarios per voxel is the major difference between the conventional definition of the cost function, F_{PTV}, in equation (1.12) and the robust definition, F_{Robust}, presented above. Following the worst-case approach, the minimal dose is assigned to CTV voxels, while the maximum dose is assigned to OAR voxels.

The formulation of the optimization problem is identical with equations (1.13) and (1.14), except that $F_{\mathrm{Robust}}(\vec{N})$ is used as cost function.

The robust cost function uses the CTV without additional margins around the target structure. This is unlike the conventional definition, where the treatment plan is optimized on the PTV. By running on several uncertainty scenarios, the presented robust optimization method intrinsically creates patient and case specific margins, eliminating the need for the standard safety margins of the PTV.

2.2.3 Robust cost function with maximum dose term

The maximum dose term (MDT) is an optional and additional contribution to the robust cost function (2.2) introduced by [Liu et al., 2012]. The original purpose of this term was to reduce hot spots in dose distributions for proton therapy by including the maximum dose scenario from each target voxel in the robust cost function. The maximum dose term has its own penalty weight, $p_{\text{CTV, max}}$, which is independent from the CTV contributions shown in equation (2.2). This results in the following cost function

$$\begin{aligned}F_{\text{Robust, MDT}}(\vec{N}) = &\sum_{i\in\text{CTV}} w_{\text{CTV}} \cdot \left(\min_{\{k\in K_{\text{Scen.}}\}} \left[D^{i}_{\text{act.}}(\vec{N},k) \right] - D_{\text{presc.}} \right)^2 \\ &+ \sum_{i\in\text{CTV}} w_{\text{CTV, max}} \cdot \left(\max_{\{k\in K_{\text{Scen.}}\}} \left[D^{i}_{\text{act.}}(\vec{N},k) \right] - D_{\text{presc.}} \right)^2 \\ &+ \sum_{j\in\text{OARs}} w_{\text{OARs}} \cdot \Theta \left(\max_{\{k\in K_{\text{Scen.}}\}} \left[D^{j}_{\text{act.}}(\vec{N},k) \right] - D_{\text{limit}} \right) \cdot \left(\max_{\{k\in K_{\text{Scen.}}\}} \left[D^{j}_{\text{act.}}(\vec{N},k) \right] - D_{\text{limit}} \right)^2 .\end{aligned} \tag{2.3}$$

For proton therapy, the robust cost function with the maximum dose term is used optionally only, whereas for carbon ion therapy the maximum dose term is mandatory to avoid an increase in target doses far beyond the prescribed dose. The impact of the maximum dose term is shown in figure 2.7 for a 50 mm diameter sphere in a cubical water phantom, optimized to a biological dose of 10 Gy(RBE). When no maximum dose term is applied (MDW=0.0, black line), the dose volume histogram (DVH) shows a massive overdosage, reaching maximum doses of 126 %. By increasing the maximum dose penalty weight, the overdosage can be reduced to 101 % for MDW=1.0 (cyan line). For a simple volume such as a sphere in water, increasing the maximum dose penalty weight above 1.0 leads to slight degradation of the DVH; however, for patient cases, and maximum dose weight (MDW) of 1.0 is sometimes insufficient to control overdosage within the target volume. Empirically determined MDW values up to 1.2 have shown to decrease the maximum delivered dose to an acceptable level below about 110 % of the planned dose.

2.2.4 Robustness analysis — Conventional vs. robust optimization

In this section, a comparison between conventional and robust optimized treatment plans will be made for the simplified case of dose delivery to a spherical target inside of a water phantom. For this setup IMPT with two opposing fields was used. The plans were optimized to a biological dose of 10 Gy(RBE). In case of the conventional optimization, a PTV with 5 mm isotropic safety margins on the CTV was chosen as the target volume. For robust optimization, the CTV was chosen as target with MDW value of 1.0.

The treatment plan quality was assessed using a robustness analysis (RA), which involves calculating 21 different dose distributions from 21 different uncertainty scenarios, namely from a manipulation

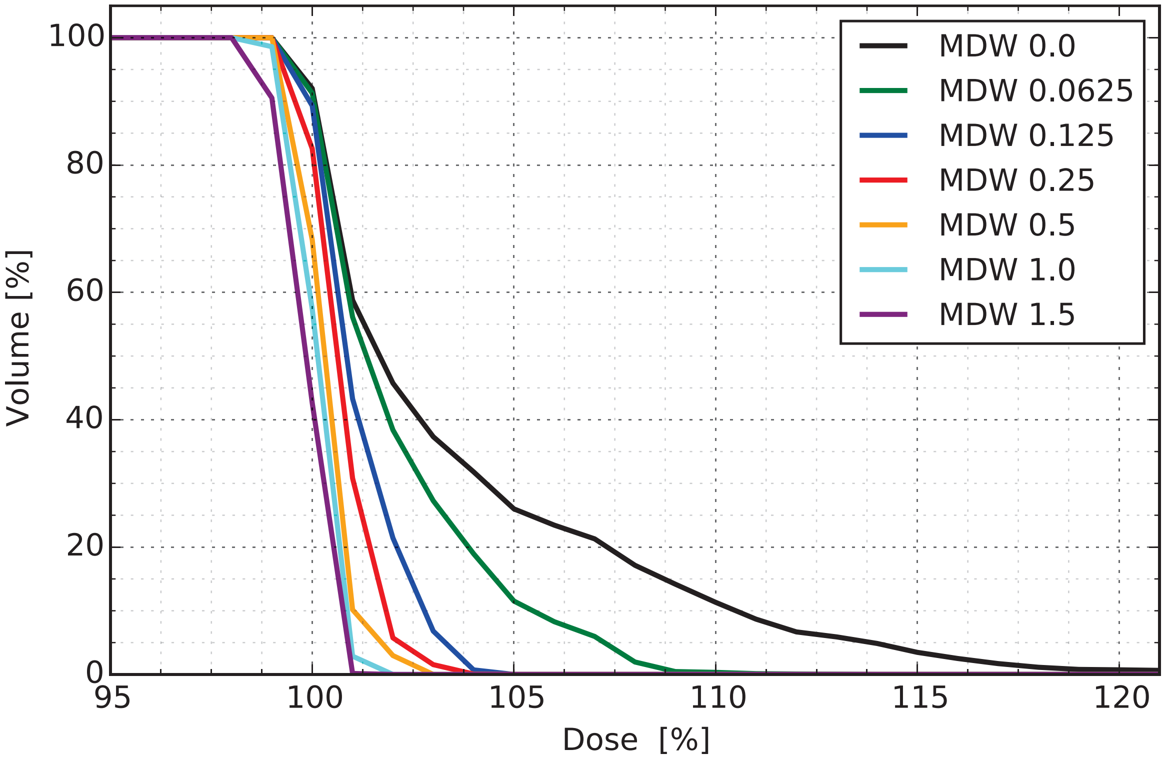

Figure 2.7.: DVH for a sphere with a diameter of 50 mm in a water phantom, showing the influence of the maximum dose term in the robust cost function for different penalty weights (MDW).

of the CT density, and shifts to the patient's isocenter. Even the superposition of density changes and position shifts are considered in the RA. The scenarios used in optimization and robustness analysis are described in more detail in table 2.2.

	nominal density	low density	high density
no shift	Opt. & RA	Opt. & RA	Opt. & RA
pos. x shift	Opt. & RA	RA	RA
neg. x shift	Opt. & RA	RA	RA
pos. y shift	Opt. & RA	RA	RA
neg. y shift	Opt. & RA	RA	RA
pos. z shift	Opt. & RA	RA	RA
neg. z shift	Opt. & RA	RA	RA

Table 2.2.: The scenarios used in the robust optimization (9 in total) are denoted with 'Opt.', the ones used for the robustness analysis (21 in total) are denoted with 'RA', i.e. for the RA also superpositions of position and density shifts are used.

Figure 2.8 illustrates the average dose curve (solid line) and the corresponding uncertainty band (light color) resulting from 21 DVHs for four treatment plans. The uncertainty band is the envelope of the minimum and maximum volumes from all 21 scenarios for each dose value on the horizontal axis of the DVH. In the conventional case (fig. 2.8(a)), the biggest uncertainty occurs at the region of the dose fall-off which around 100 % of the target dose. For plans where the robust optimization was applied, the uncertainty band has been reduced to a small area, located directly on the shoulder of the dose fall-off (feg. 2.8(b)).

In order to measure the robustness of a plan, the dose spread (DS) is used, as follows:

$$\mathrm{DS} = \max_{\{k \in K_{\mathrm{Scen.}}\}} \mathrm{D}_{50\%}(k) - \min_{\{k \in K_{\mathrm{Scen.}}\}} \mathrm{D}_{50\%}(k), \tag{2.4}$$

where k is from the set of $K_{\mathrm{Scen.}}$ uncertainty scenarios. Table 2.3 summarizes DS, values for the minimum dose delivered to 99% of volume ($\mathrm{D}_{99\%}$), minimum dose delivered to 50% of volume ($\mathrm{D}_{50\%}$), the homogeneity index (HI) and the maximum dose delivered to a single voxel ($\mathrm{D}_{\mathrm{Max}}$) from a RA with $K_{\mathrm{Scen.}} = 21$ uncertainty scenarios. Using robust optimization, the DS is shown to be reduced by a factor of approximately 8; however, this reduction of the uncertainty band comes at the price of a smaller $\mathrm{D}_{99\%}$ and an increased $\mathrm{D}_{\mathrm{Max}}$. Therefore, the planned dose must be increased by 2 % recovers the $\mathrm{D}_{99\%}$ value while maintaining the reduced DS. This will come at the cost of an additional increase to the maximum dose.

	conventional	robust	robust*	robust$^{\mathrm{HC}}$
D99 [%]	98.2 ± 2.0	96.9 ± 1.6	99.1 ± 1.7	99.4 ± 1.6
D50 [%]	100.01 ± 1.45	100.03 ± 0.18	102.05 ± 0.20	102.48 ± 0.04
HI [%]	2.9 ± 1.0	2.2 ± 0.5	2.1 ± 0.4	2.7 ± 0.3
D_{max} [%]	101.1 ± 1.6	102.0 ± 1.5	104.0 ± 1.5	105.0 ± 2.0
DS [%]	3.63	0.44	0.47	0.13
D99 ≥ 100% [%]	33.3	0.0	47.6	47.6

Table 2.3.: Average values and standard deviation for dose measurements from robustness analysis for a sphere in water phantom for conventional and robust optimization. The robust plan with the increased planned dose ($D_P = 10.2\,\mathrm{Gy(RBE)}$) is denoted with a *. The robust plan optimized with a hard constraint of 10 Gy(RBE) is denoted with a $^{\mathrm{HC}}$. The last line states the percentage from 21 uncertainty scenarios in which $\mathrm{D}_{99\%}$ is ≥ 100 %.

Instead of increasing the planned target dose manually, in order to increase the $\mathrm{D}_{99\%}$ of the robust plan to values comparable to the conventional plan, it is possible to repeat the optimization several times until the desired goal is accomplished. This strategy is called "objective optimization" and has been implemented into TRiP4D by Anderle et al. [2018]. As this strategy is independent of the optimization algorithm itself, only minor adaptations were necessary to use it for the robust optimization kernel. For the presented case, the chosen "objective" is a $\mathrm{D}_{99\%} \geq 100\,\%$, which corresponds to a hard constraint dose value of 10 Gy(RBE). As this objective sets a strict limit to the $\mathrm{D}_{99\%}$ value, it will be further on called "hard constraint" (HC).

The procedure of the objective optimization starts with assessing the fraction of under-dosed voxels after an initial optimization with the number of iterations reduced by a factor of 2. The underdosage is the difference between the actual dose of a voxel and the predefined hard constraint dose value. For the robust optimization kernel, the algorithm of the objective optimization always chooses the dose of the nominal scenario as actual dose for each voxel. A voxel is counted as under-dosed if its actual dose is below the hard constraint dose value. The algorithm then increases the planned dose, voxel by voxel,

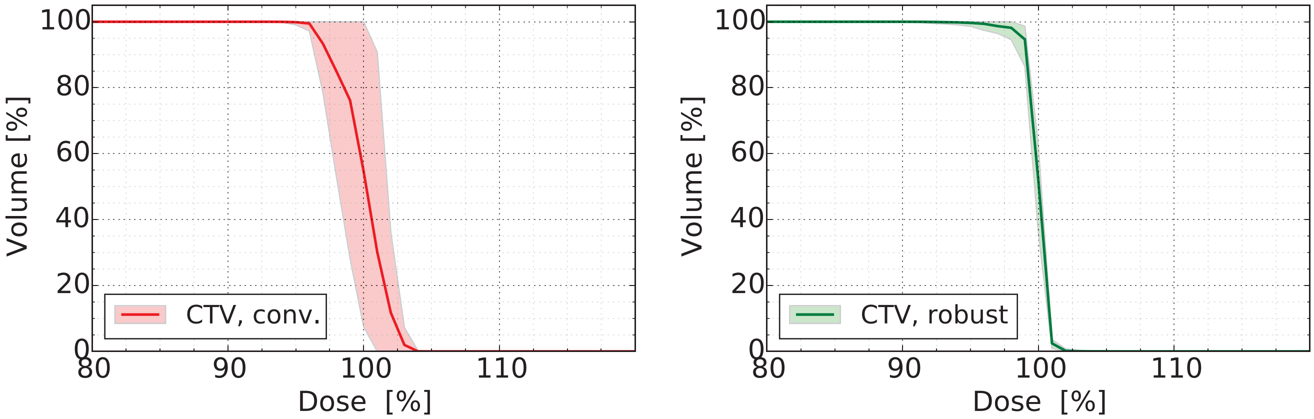

(a) Conventional PTV optimization.

(b) Robust CTV optimization.

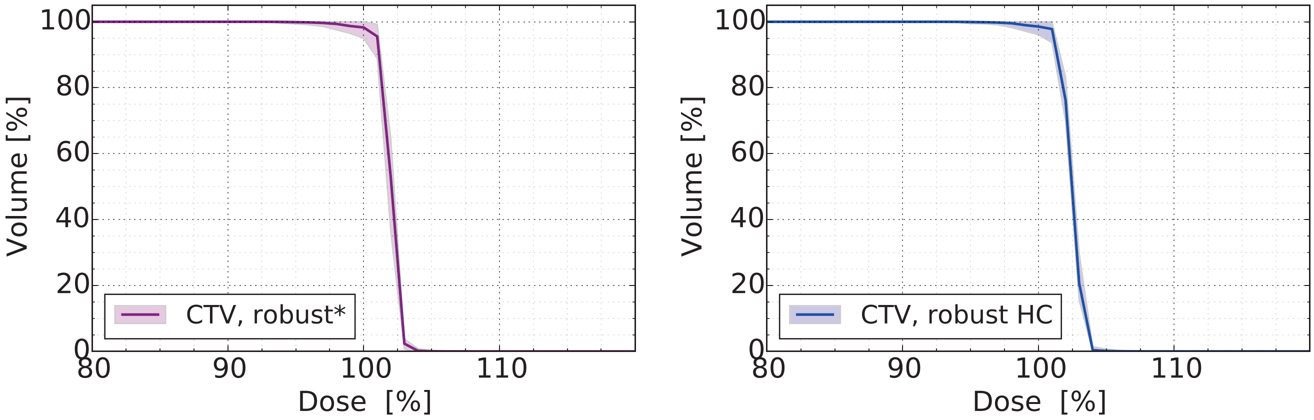

(c) Robust CTV optimization with a planned dose of 10.2 Gy(RBE).

(d) Robust CTV optimization with hard constraint of 10 Gy(RBE).

Figure 2.8.: DVHs with uncertainty bands resulting from robustness analysis for a sphere in water with a diameter of 50 mm. Figure shows the difference between (a) conventional, robust optimization with (b) default and (c) by 2 % increased planned dose and (d) robust optimization using adaptive planning with an hard constraint on the CTV of D99 $> 100\,\%$. Solid lines: average DVH, light colors: uncertainty band (min/max envelope). All DVHs are normalized to a target dose of 10 Gy(RBE).

for each under-dosed voxel, up to 0.1 Gy additional dose. The increase of the planned dose is restricted to a maximum of 110 % of the hard constraint dose value.

Comparing the robust HC plan (figure 2.8(d)) with the other two robust optimized plans (figures 2.8(b) and 2.8(c)), the fall-off of the average DVH curve is not as linear. Furthermore, compared to the robust plan with the planned dose increased by 2 %, the maximum dose in the DVH of the robust HC plan is slightly increased (see also table 2.3).

If objectives, such as $D_{99\%} \geq 100\,\%$ of the planned dose, are required during treatment planning, there are only few qualitative differences between the simple robust optimization with an empirically increased planned dose by 2 % and these of an objective optimization with a hard constraint. For both plans, the constraint is fulfilled in 10 of the 21 scenarios considered in the RA only.

2.3 Robust RBE variation

Since the RBE plays an important role in calculating the biological dose for carbon ions, it was postulated that varying the RBE during robust optimization could potentially improve the treatment plan robustness against biological uncertainties. A sensitivity analysis by Friedrich et al. [2013] of the parameters determining the RBE estimated an uncertainty for the RBE value in the SOBP of about 10 %; however, the given RBE uncertainty served as a guiding value only and also depends on patient geometry, the choice of beam angles, and the α/β ratio of the tissue. Nonetheless, the findings from [Friedrich et al., 2013] support the hypothesis that introducing an RBE uncertainty scenario into the robust optimization will reduce the susceptibility of carbon ion treatment plans to manipulated RBE values.

The conception of the robust RBE scenario was to describe the worst case for target and OAR voxels in a single scenario. This is possible as the biological dose is proportional to the RBE value and reducing the RBE means reducing the biological dose and vice versa. Given that underdosage is the worst case for target voxels and overdosage the worst case for OAR voxels, scaling the RBE value depending on the voxel type will cover the RBE uncertainty in a single scenario.

During each iteration step of the optimization, the biological dose is calculated for all target and OAR voxels. First, the physical dose is determined and the $\mathrm{RBE}^i_{\mathrm{initial}}$ value for a each voxel i is calculated from particle spectra and the α_i and β_i values of the corresponding voxel. The biological dose is computed by multiplying physical doses with $\mathrm{RBE}^i_{\mathrm{initial}}$ values. At this point, the $\mathrm{RBE}^i_{\mathrm{initial}}$ value must be scaled by ±10 % depending on the voxel type.

Since the RBE value is always larger or equal than unity by definition, following scaling function is used:

$$\mathrm{RBE}^i_{\mathrm{final}} = \left(\mathrm{RBE}^i_{\mathrm{initial}} - 1\right) \cdot \left(1.0 \pm 0.1\right) + 1. \tag{2.5}$$

For OAR voxels, the 10 % values are added on the initial RBE value $\mathrm{RBE}_{\mathrm{initial}}$, increasing the biological dose, and for target voxels, the 10 % values are subtracted to decrease the dose. This strategy ensures that RBE values are always ≥ 1.0.

The robust optimization with an additional RBE scenario was tested on a lung cancer patient. For simplification, only 3D optimization was used to create the treatment plans, where the planned target dose was 25 Gy(RBE). The robust RBE plan was compared to a robustly optimized plan (as described in section 2.2.2) and a conventionally optimized PTV plan.

To observe the influence of the RBE shift, plan quality was initially assessed by evaluating the CTV coverage for the aforementioned nine basic scenarios (the nominal, two range error and six position error scenarios); the corresponding DVHs, including uncertainty bands, are shown in the left column of figure 2.9. The 27 error scenarios of the superposition of the 9 basic uncertainty scenarios with RBE shifts of ±10 % are presented in the right column of figure 2.9. The results of the RA are summarized in table 2.9. Target coverage is assessed with dose measurements such as D99, $\mathrm{D}_{\mathrm{max}}$ HI, DS and the dose exposure of the smaller airways (SA) with $\mathrm{D}_{\mathrm{vol}}$ and $\mathrm{D}_{\mathrm{max}}$.

As the left column of figure 2.9 shows, all three plans were robust against the basic nine error scenarios as almost no uncertainty bands are present for the target dose measures. Compared to both robust plans, the conventional PTV plan unexpectedly had the lowest dose spread, a factor of about 2 smaller than for

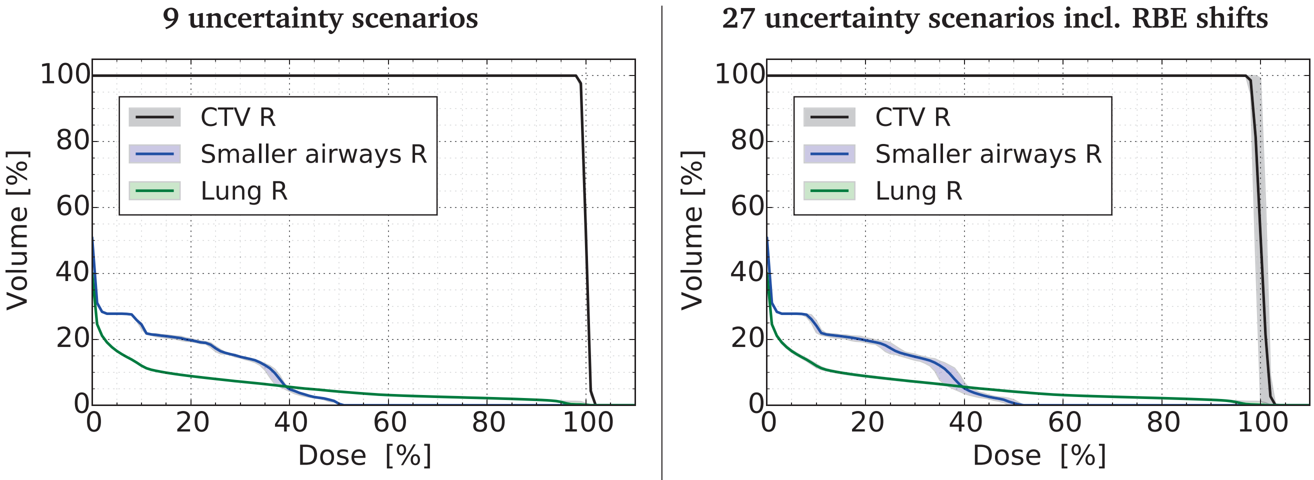

(a) Conventional PTV optimization.

(d) Conventional PTV optimization.

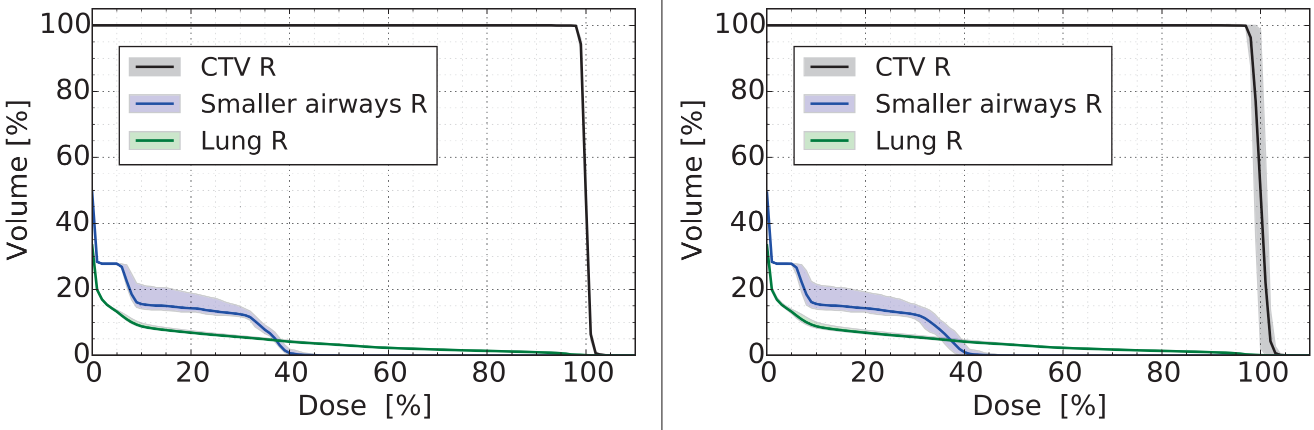

(b) Robust CTV optimization.

(e) Robust CTV optimization.

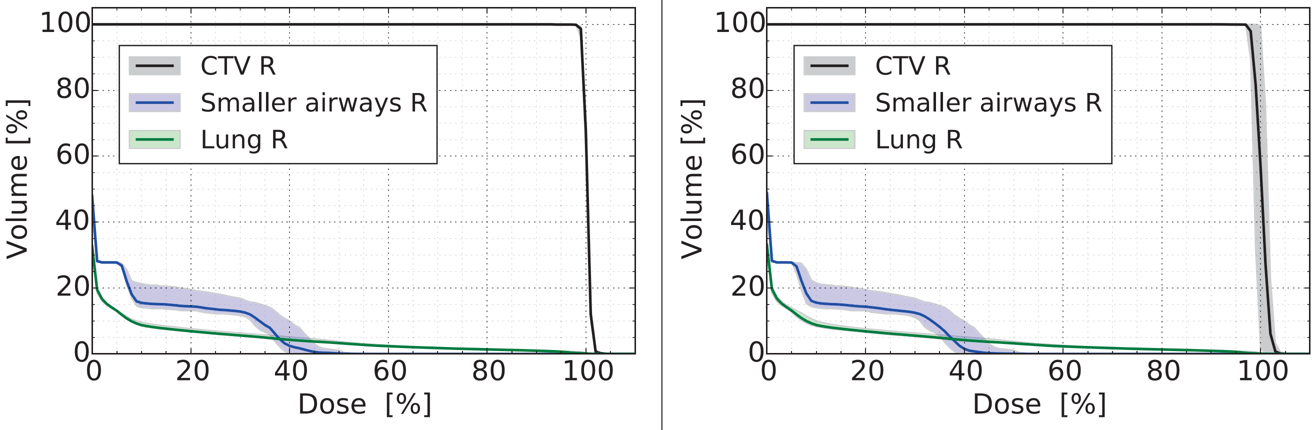

(c) Robust CTV optimization incl. RBE scenario.

(f) Robust CTV optimization incl. RBE scenario.

Figure 2.9.: DVHs with uncertainty bands resulting from robustness analysis for a lung cancer patient irradiated with a 3D treatment plan with two orthogonal fields on the reference CT phase for 3 different plans from conventional optimization (a,d), default robust optimization (b,e) and robust RBE optimization (c,f). Left column shows results for the 9 basic uncertainty scenarios. Right column the superposition with an RBE shift of ±10 % resulting in 27 error scenarios. Solid lines: average DVH, light colors: uncertainty band (min/max envelope). All DVHs are normalized to a target dose of 25 Gy(RBE).

		conventional	robust	robust RBE
9 scenarios	D99 [%]	98.4 ± 0.1	98.2 ± 0.0	99.1 ± 0.0
	D_{max} [%]	101.0 ± 0.0	103.4 ± 0.7	103.7 ± 0.7
	HI [%]	2.0 ± 0.1	2.4 ± 0.1	2.5 ± 0.0
	DS [%]	**0.04**	**0.07**	**0.15**
	SA: D0.5cc [%]	25.6 ± 0.5	11.8 ± 7.0	12.9 ± 8.9
	SA: D_{max} [%]	50.0 ± 0.0	42.8 ± 3.3	44.0 ± 5.6
27 scenarios incl. RBE shifts	D99 [%]	98.5 ± 1.0	98.2 ± 1.0	98.6 ± 1.1
	D_{max} [%]	101.3 ± 1.2	103.7 ± 1.4	103.7 ± 1.4
	HI [%]	2.1 ± 0.2	2.5 ± 0.1	2.4 ± 0.2
	DS [%]	**2.32**	**2.50**	**2.81**
	SA: D0.5cc [%]	25.6 ± 1.0	11.9 ± 7.1	12.2 ± 7.8
	SA: D_{max} [%]	50.0 ± 0.8	42.8 ± 3.4	43.1 ± 4.2

Table 2.4.: Average values and standard deviations of dose measurements from robustness analysis of a 3D treatment plan for conventional, robust and robust RBE optimization for a lung cancer patient. SA = smaller airways.

robust plan and of about 4 for the robust RBE plan, respectively. Even the homogeneity index was about 20 % smaller for the conventional plan. Hence, for the basic uncertainty scenarios, the conventional plan provided the highest robustness.

When the additional 18 dose scenarios with a superposition of the basic nine scenarios with an RBE shift of ±10 % were also taken into account, the uncertainty bands increased for all three plans. The conventional plan still maintained lower homogeneity index and dose spread values than for both robust plans.

Despite the reduced robustness of the target coverage, both robust plans have been shown to generate superior OAR sparing. Independent of including RBE shifts to the RA, the volume dose for the SA was a factor of about 2 smaller for both robust plans compared to the conventional plan. Also the maximum dose was about 20 % smaller for both robust plans. As the uncertainty bands for the target coverage are only marginally differing, the default robust plan is the more favorable plan due to the shape of dose curve for the SA, generating the lowest volume dose and maximum dose. Additionally, the more symmetrical distribution of the uncertainty band around the average dose curve of the CTV is more favorable for the robust plan, especially for doses larger than 100 % of the target dose.

Discussion

For the tested lung patient case, the conventional PTV plan and the two robust plans seem to be inherently robust against the integrated RBE uncertainty. For all plans, the uncertainty band around the average dose curve of the CTV increased similarly, when RBE errors of ±10 % were included. Using an additional worst-case scenario during the robust optimization which considers a shifted RBE value does not improve the resulting dose distribution. Instead, the resulting target coverage becomes slightly worse than for the conventional or robust treatment plan.

As introducing an RBE shift during the dose calculation produces a global increase to the dose if the shift is positive and a reduction to the dose if the shift is negative, the initial approach to include RBE uncertainty into the robust optimization was different. Two RBE uncertainty scenarios were added to the nine basic uncertainty scenarios of the robust optimizer, one decreasing and the other increasing the RBE, resulting in 11 error scenarios. These two scenarios proved to overshadow the other scenarios during optimization and, being potentially incongruous, prevent the optimizer from finding any optimal solutions. This conclusion was the rationale for the approach described in section 2.3, unifying the worst-case RBE values for target and OAR voxels in a single uncertainty scenario. Enabling the robust optimizer to successfully minimize the cost function, the RBE uncertainty scenario did not show the expected improve in robustness against RBE uncertainty. Surprisingly, the dose distribution with the highest robustness for target coverage was generated by the conventional plan. Possibly, even the unified RBE error scenario is still incongruous to the remaining uncertainty scenarios, more impeding the optimizer from finding optimal solutions, than helping to generate robust treatment plans.

Conclusion

Since the RBE calculation is highly complex and depending on numerous quantities, a simplified approach has been developed to implement the RBE uncertainty scenario into the robust optimizer. As a simplification, a single scenario, unifying the worst-case RBE values for target and OAR voxels, was added to the already existing nine uncertainty scenarios. Depending on the voxel type, the RBE value was scaled by ±10 %. As the resulting DVHs show, the anticipated improvement of robustness against RBE variation during dose calculation could not been accomplished by using an additional RBE uncertainty scenario in the robust optimization. Possibly, the chosen approach oversimplified the source for RBE uncertainty. Against the initial assumptions, a more complex approach is probably needed. However, due to the numerous quantities influencing the RBE, the potential degree of complexity could again impede the optimizer from finding optimal solutions. Since the RBE is a quantity afflicted with uncertainties as described by Friedrich et al. [2013], it would be still of high relevance to consider RBE uncertainties within a robust optimization.

2.4 Discussion

In this chapter, an algorithm for the robust optimization of carbon ion treatment plans has been presented. The algorithm was based on a voxel-wise worst-case approach as described by Pflugfelder et al. [2008] and Liu et al. [2012]. From a set of potential range or patient setup errors resulted a set of different possibly dose distribution. In each iteration step of the robust optimization, the scenario with the lowest dose is selected for target voxels and the scenario with the highest dose is selected for OAR voxels. Since this selection is done on a voxel-wise basis, the resulting treatment plan will consist of mixed contributions from different uncertainty scenarios, which can not be realized at the same time in a real patient. For example, if a real patient is shifted to the right during setup, a simultaneous shift to left is not possible. With the current implementation, the optimizer can not account for these illogical combinations of uncertainty scenarios, resulting in “unphysical” treatment plans. However, the resulting plans could also be described as overly conservative, anticipating the incidence of errors impeding the delivered dose distribution.

The treatment plans generated with the robust optimizer, were tested on a spherical target in a water phantom without the presence of critical structures. Conventional plans optimized on a PTV and the robust treatment plans were compared for plan quality and robustness against different uncertainty scenarios. This was done by performing a robustness analysis (RA). During this RA, dose distributions for different error scenarios were calculated. The RA considered the nine basic uncertainty scenarios, as well as the superposition of range and setup uncertainties resulting in additional 12 error scenarios, which adds up to 21 uncertainty scenarios in total. Thus, the RA is enabled to see beyond potential error scenarios, which have already been accounted for during the robust optimization.

Comparison between the RA for the conventional plan (as seen in figure 2.8(a)) and the robust plan (as seen in figure 2.8(b)) has revealed a considerable increase in robustness as seen in the large reduction to the uncertainty bands around the average CTV dose curves. The dose fall-off of the robust plan intersects the 100 % dose value at around 50 % of the volume, inevitably leading to a reduction in target coverage. The average D99 value is reduced from 98.2 % to 96.7 %. An additional method for recovering the target coverage is then necessary. In this work, two options for recovery of the target coverage were investigated. First, an empirical approach of globally increasing the planned target dose by 2 % was investigated. Second, a more elaborate method involving the usage of an existing objective optimization strategy was used. By repeating the optimization several times while adapting weights and planned target dose on a voxel-wise basis after each optimization run, this method enabled the consideration of dose volume and hard constraints.

The resulting DVH for the case of globally increased planned dose is shown in figure 2.8(c). The average DVH curve as well as the uncertainty band has nearly the same shape as the DVH curve of the robust plan (as seen in figure 2.8(b)), but is shifted to higher dose values by an offset of about 2 %. This can also be observed in the $D_{99\%}$, $D_{50\%}$ and D_{Max} values in table 2.3 which are likewise increased by approximately 2 %. The steep and narrow fall-off of the DVH curve of the robust plan with globally increased planned dose enabled a recovery of the target coverage.

A similar result could be obtained by using an objective optimization approach which sets a hard constraint for the target of $D_{99\%} \geq 100\,\%$. The objective optimization algorithm successfully adapted the planned dose for underdosed voxels and produced a similar plan as the robust optimization with globally increased target dose. Compared to figure 2.8(c), the DVH in figure 2.8(d) has an even narrower uncertainty band than robust plan with globally increased target dose, but the fall-off is less steep resulting in slightly more overdose of $(104.0 \pm 1.5)\,\%$ vs. $(105.0 \pm 2.0)\,\%$. The percentage of uncertainty scenarios, in which the constraint of $D_{99\%} \geq 100\,\%$ is fulfilled, is about 48 % for both, the robust plan with globally increased planned dose and the robust plan using objective optimization.

In this chapter, treatment planning was limited to cases with no consideration of critical structures. The influence of OARs on plan quality of robust treatment plans will be investigated in chapter 3. The relevance of an objective optimization will change for complex patient cases, especially with dose volume constraints for OARs in close vicinity to the target. To be fulfilled, a dose volume constraint requires a certain fraction of the OAR volume to not exceed a given dose value. Compared to objective optimization, the empirical method of increasing the planned dose globally by some percent during robust optimization only works for hard constraints on target dose, but not for dose volume constraints.

The impact of the maximum dose term in the robust cost function was an unexpected finding. For robust proton treatment planning, the maximum dose term was proposed to minimize the occurrence of hot spots in the target volume [Liu et al., 2012]. For carbon ions, this term not only reduced hot spots (compare figure 3.4 (a) and (b)), but more importantly, the maximum dose term helped to attenuate an unrestricted growth of the maximum dose (see 2.8(d)). A maximum dose penalty weight around 1.0 was, therefore, recommended. For values larger than about 1.5, the maximum dose was even further reduced, at the cost of sacrificing target coverage around the D95 region. Using penalty weights below 1.0, basically deactivated the efficacy of the maximum dose term in avoiding overdosage, resulting again in unfavorable high maximum dose values.

The reason for this behavior may be that the robust optimizer uses only the minimal dose scenario to determine the new particle numbers for *all* possible scenarios. During the optimization, particle numbers get adapted in the manner that every scenario is as close as possible to the prescribed dose. However, without the maximum dose term, there is no correcting momentum in the robust cost function which stops the optimizer from exceeding the planned dose.

As described in section 2.2.1, field dose correlation matrices are set up for each uncertainty scenario, which increases the used working memory by a factor of about nine. Optimizing simple target structures in a water phantom does not pose a big challenge to the optimizer, but robust treatment planning of patient CT scans does. As will be described in chapter 3, the use of randomized subsampling of voxels becomes necessary during robust optimization to enable that the robust optimizer can handle the robust optimization's problem size at all. There are other potential methods to decrease memory consumption which have yet to be explored, such as deleting FDC matrices describing similar scenarios. This is the case for patient setup error scenarios, whose lateral projection on the BEV axis is zero, generating a FDC matrix which is identical to the one of the nominal case. Having two identical FDC matrices present during optimization dose not further contribute to the process of finding a robust treatment plan. Therefore, the uncertainty scenario in question, including its corresponding FDC matrix, can be deleted. Due to the current implementation of the robust optimization in TRiP4D, such a scenario cannot simply be deleted. However, the potential of this method to save memory may be used by a more modular implementation of the error scenarios for the robust optimization with TRiP4D.

2.5 Conclusion

The presented robust optimization algorithm, which uses a voxel-wise worst-case approach, provides a suitable method to account for uncertainties such as patient setup errors and range changes during treatment delivery for carbon ions. The increase in robustness could be seen in the resulting set of DVH curves from a robustness analysis and was characterized by an reduced uncertainty band, a steeper fall-off of the average dose curve of the CTV and a more homogeneous plan. Due to the shape of the robust DVH, the increased robustness was achieved by a minor decrease to the target coverage. This can be solved by globally increasing the planned target dose by approximately 2 % or by using an objective optimization with an hard constraint on the target volume. Using one of the aforementioned approaches for a simple spherical structure in a water phantom, average dose measurements for target coverage, such as D99, became comparable to the results of a conventional PTV plan.

The presented robustness analysis (RA) not only uses error scenarios already applied in the robust optimization, but additionally considers the superposition of setup errors and range uncertainty scenarios. This approach is favored, as it accounts for combinations of scenarios which are likely to occur during treatment, but which are not explicitly considered during the robust optimization process.

Finally, the importance of the maximum dose term on the quality of robust treatment plans using carbon ions, was studied. For treatment planning with protons, this additional term of the robust cost function is used optionally, in order to avoid hot spots in the delivered dose distribution. For robust optimization with carbon ions this term is not optional,as without it overdosage in the target volume is certain. It is strongly recommended to use the maximum dose term in robust optimization for carbon ions. If the cost function's worst-case term has a penalty weight of 1.0, the suggested range for the penalty weight of the maximum dose term is 1.0 to 1.2.

The influence of the presence of OARs during robust optimization will be investigated in the following chapter within.

3 Robust 4D optimization

Contents

3.1 Introduction

One of the major issues encountered during carbon ion radio therapy of lung tumors is the density gradient between lung and surrounding tissue. This density difference can lead to significant range changes from nominal targeting accuracy, which not only deteriorates the delivered dose distributions, but also harms surrounding normal tissues. For moving tumors, such as those of the lung, the main source of range uncertainties is caused by the periodic tumor motion, leading to changes in the WEPLs over time.

Figure 3.1 exemplarily shows the dose distribution of a single field uniform dose (SFUD) plan, optimized on the end inhale phase of a 4DCT, and the same plan applied on the end exhale phase of the same 4DCT without any adaptations. In the end exhale phase, the tumor has moved about 2 cm in superior direction, causing a deterioration of the inferior part of the dose distribution. Due to the lower density of the surrounding lung tissue, considerable range overshoots occur which increase the dose exposure to the heart.

The changes in tumor depth due to respiratory motion can be addressed by creating a WEPL ITV. To create a WEPL ITV, the target volumes from all motion states of a 4DCT are transformed to the WEPL space, then the union of these transformed target volumes is generated. The resulting volume, the WEPL ITV, accounts for ranges changes which are caused by respiratory tumor motion. As the transformation to the WEPL space strictly depends on field parameters like couch and gantry angle, the resulting WEPL ITVs

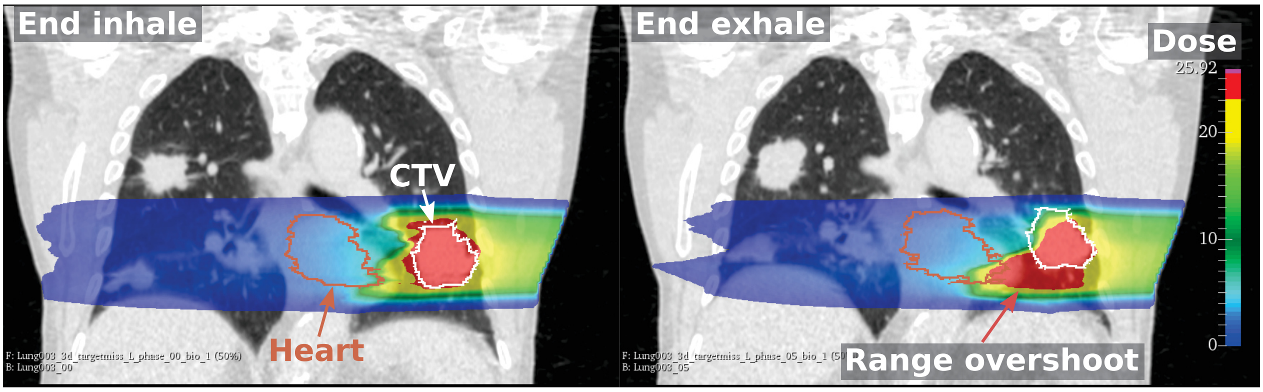

Figure 3.1.: Left panel: dose distribution of a SFUD plan, optimized on the end inhale phase of a 4DCT of lung cancer patient without safety margins. Right panel: same SFUD plan applied on the end exhale phase. Due to periodic tumor motion and the density gradient between tumor and surrounding lung tissue, considerable range changes are generated for the end exhale phase, causing dose deteriorations which increase the dose exposure to the heart.

are likewise field specific, only allowing to be used in SFUD optimization. Graeff et al. [2012] proposed a solution to this limitation by moving the part of algorithm calculating the field specific WEPL changes to the part of the optimization algorithm which transforms geometrical path lengths to WEPL space. With this approach, a MFO IMPT optimization can be performed, which is based on the geometrical ITV, not requiring field specific increases to the target volume. Though this method works, it is highly complex and the internal transformation of the geometrical ITV to the WEPL space is not a unique mapping.

A more elegant approach is the 4D ITV optimization introduced by Graeff [2014], where an influence matrix is set up for each motion state, correlating all target voxels from a specific motion state to the grid of beam spots of a single treatment plan. This method has been successfully adapted for multiple targets and used in an in-silico patient study with carbon ions presented by Anderle et al. [2018]. In the corresponding study, the results were compared to actual treatments done with SBRT and showed that the 4D ITV approach could meet strict dose constraints for critical organs (defined by Benedict et al. [2010]) without compromising the prescribed target dose. Although different interplay patterns were assessed on four motion patterns with different combinations of respiration periods and starting phases, the study only looked at a single nominal dose scenario, not considering any further range changes or patient positioning uncertainties.

The dose distribution of a 4D IMPT carbon ion plan differs from the an 3D SBRT plan as shown in figure 3.2. The SBRT dose distribution shows an inevitable low dose bath of X-rays, which is delivered to the complete thorax. In contrast, carbon ion therapy with the 4D IMPT approach significantly decreases the low dose exposure of the thorax, due to both, the usage of less treatment fields and the favorable depth-dose profile of ions as shown in figure 1.5. Compared to photons, not only the dose to surrounding tissue but also the dose deposited in entry channels is considerably reduced for the usage of carbon ions.

A robustness analysis, as described in chapter 2, was performed for the same patient cohort used in Anderle et al. [2018]. The treatment plans used for this analysis are the same 4D ITV plans as used in the study conducted by Anderle et al. The RA reveals that for some critical structures, like smaller airways, the strict dose constraints (as described in Benedict et al. [2010]) could not be met any longer in the majority of considered uncertainty scenarios.

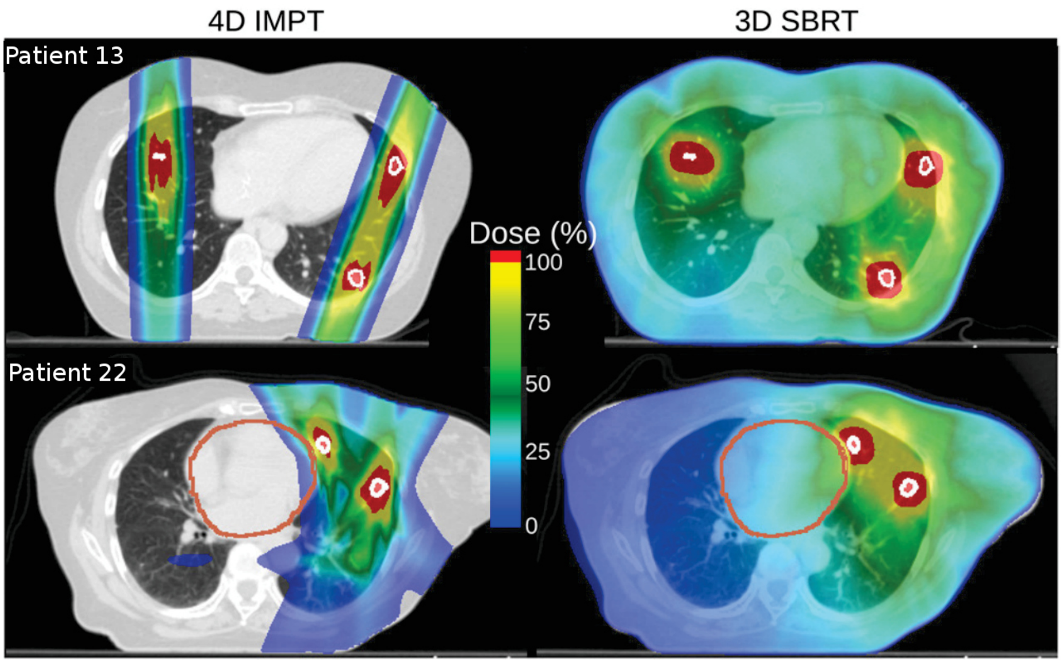

Figure 3.2.: 4D IMPT and SBRT treatment plans for two patients. First row: patient 13 with 5 tumors and no nearby critical organs. Second row: patient 22 with 4 tumors, from which 2 are next to the heart. For the 4D IMPT plans, the doses are calculated on 4DCTs, whereas the SBRT plans are calculated on static CTs. The targets are outlined in white, the heart in red. Figure adapted from [Anderle et al., 2018].

To account for range changes and setup uncertainties, a robust version of the 4D ITV approach was introduced, based on the worst-case method presented in chapter 2. This algorithm has been implemented into TRiP4D, and a more detailed description can be found in section 3.2.

The following hypotheses are established and will be examined later in this chapter:

1. Robust 4D ITV optimization leads to a general increase in robustness against range changes and patient positioning uncertainties.
2. Robust 4D ITV optimization enables a superior OAR sparing in the majority of considered uncertainty scenarios.
3. Although the nominal dose distribution from the robust plan might degrade, robust 4D optimization still maintains the advantage in OAR avoidance over photon therapy.

3.2 Optimization method

The 4D ITV optimization strategy used in this chapter is based on the method developed by Graeff [2014]. In order to handle multiple targets, the optimization algorithm has received further extensions by Anderle et al. [2018]. The cost function for 4D-ITV-based IMPT, as used by Anderle et al., is described by

$$F_{\text{4D ITV}}(\vec{N}) = \sum_{m\in M} \left[\begin{array}{l} \displaystyle\sum_T w_T \sum_{i\in\text{Target}} \left(D^{i,m}_{\text{act.}}(\vec{N}) - D_{\text{presc.}}\right)^2 + \\ \displaystyle\sum_{j\in\text{OARs}} w_{\text{OARs}} \cdot \Theta\left(D^{j,m}_{\text{act.}}(\vec{N}) - D^{j}_{\text{limit}}\right) \cdot \left(D^{j,m}_{\text{act.}}(\vec{N}) - D^{j}_{\text{limit}}\right)^2 \end{array} \right], \tag{3.1}$$

where M is the set of all motions states of a 4DCT. For patients with multiple tumors, T represents the set of all targets included in the optimization. $D_{\text{presc.}}$ denotes the dose prescribed by a physician and D_{limit} is the dose limit for the surrounding critical structures considered during treatment planning. Values for D_{limit} which depend on organ and fractionation according to Benedict et al. [2010] can be found in table B.1. The formulation of the optimization problem is identical with equations (1.13) and (1.14), except that $F_{\text{4D ITV}}(\vec{N})$ is used as cost function.

One should note, that this approach, though it considers all motion states of a 4DCT, only generates a single treatment plan (single RST grid) which is valid for all motions states accounting for motion induced range changes from all phases. In order to ensure that the tumor is within the treatment volume at all times, the final 4D ITV can be considerably larger than the geometrical ITV. Further motion mitigation, using slice-by-slice rescanning, is addressed in section 3.4.

A robust version of the 4D ITV approach was realized by a straightforward implementation of the worst-case method into the existing 4D ITV algorithm. The same implementation as presented in chapter 2.2.1 was used for the setup of the robust IMPT fields. The further procedure of the robust 4D ITV optimization is described in figure 3.3. As in figure 2.5, the result of the robust field setup is an expanded RST grid which is large enough to contain all pencil beam spots corresponding to the uncertainty scenarios under consideration. The nine stored uncertainty scenarios per field containing shifted HLUT tables and shifted patient to gantry and gantry to patient transformation matrices are stored in the working memory for the setup of the field dose correlation (FDC) matrices.

Following the non-robust implementation of 4D ITV optimization method, the dose contributions from each pencil beam spot from the RST grid are calculated and stored in the FDC matrices for all target and OAR voxels from all motion states from a 4DCT (typically 10 motion states). For the non-robust implementation, this typically results in 10 FDC matrices. For the robust implementation, a FDC matrix for each of the nine uncertainty scenarios is calculated at each motion state. This additional dimension can be seen in the $k = 9$ dose scenarios $D^{i,m}_{\text{act.}}(\vec{N}, k)$ used in the cost function for the robust 4D ITV optimization:

$$F_{\text{Robust 4D ITV}}(\vec{N}) = \sum_{m \in M} \left[\begin{array}{l} \displaystyle\sum_{T} w_T \sum_{i \in \text{Target}} \left(\min_{\{k \in \text{Scen.}\}} \left[D^{i,m}_{\text{act.}}(\vec{N}, k) \right] - D_{\text{presc.}} \right)^2 + \\ \displaystyle\sum_{T} w_{T,max} \sum_{i \in \text{Target}} \left(\max_{\{k \in \text{Scen.}\}} \left[D^{i,m}_{\text{act.}}(\vec{N}, k) \right] - D_{\text{presc.}} \right)^2 + \\ \displaystyle\sum_{j \in \text{OARs}} w_{\text{OARs}} \cdot \Theta \left(\max_{\{k \in \text{Scen.}\}} \left[D^{j,m}_{\text{act.}}(\vec{N}, k) \right] - D^{j}_{\text{limit}} \right) \cdot \left(\max_{\{k \in \text{Scen.}\}} \left[D^{j,m}_{\text{act.}}(\vec{N}, k) \right] - D^{j}_{\text{limit}} \right)^2 \end{array} \right], \quad (3.2)$$

where m is the current motion states from a set of M motion states. During the optimization, the minimum or maximum dose scenario k from a set of dose scenarios is chosen, depending on the voxel being target or OAR for each voxel i and j. This means that for each motion state, 9 FDC matrices are set up, creating a total of 90 influence matrices in the working memory during the plan optimization. The formulation of the optimization problem is identical with equations (1.13) and (1.14), except that

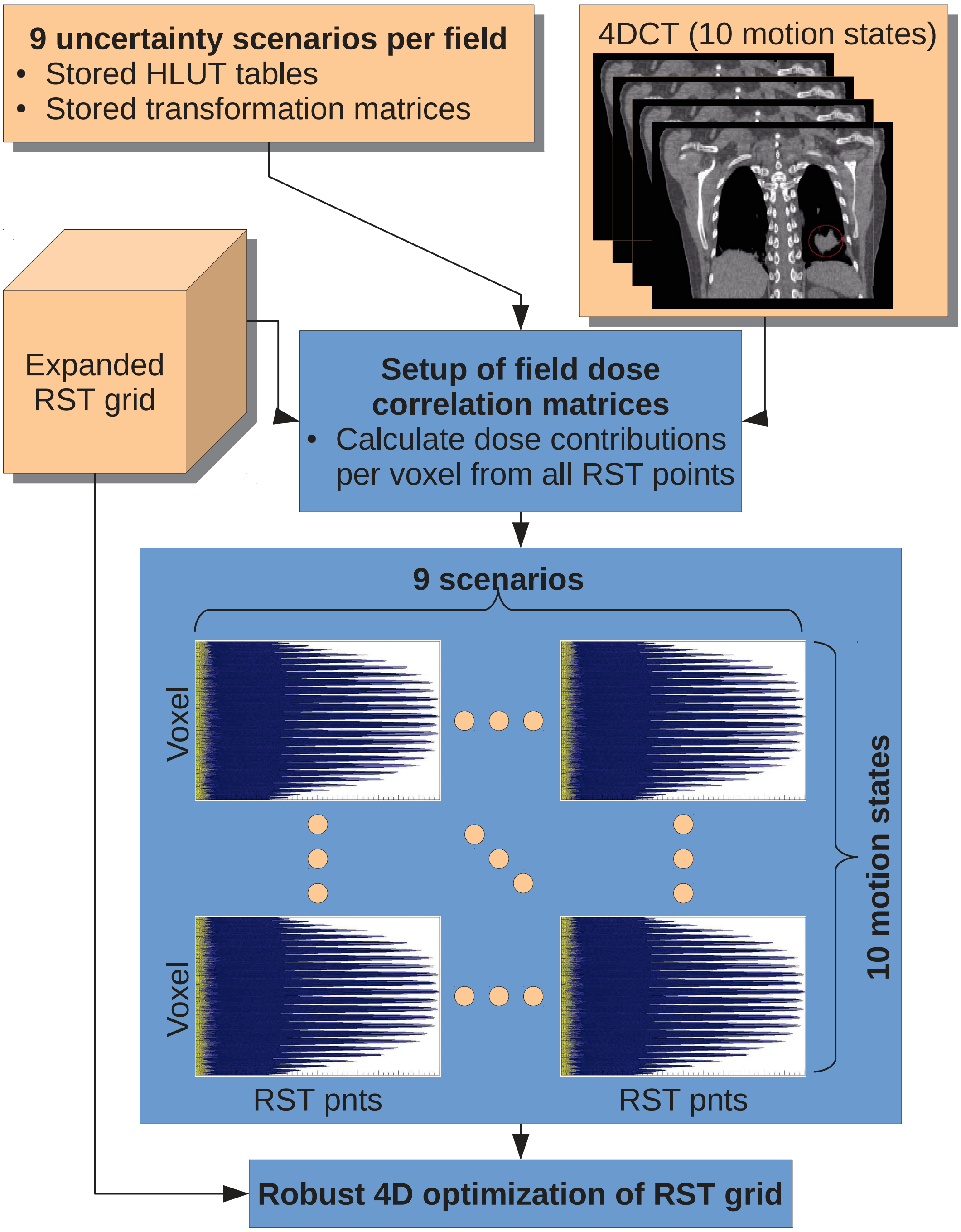

Figure 3.3.: The flowchart schematically shows the setup of field dose correlations matrices for the robust 4D ITV optimization. The field dose correlation (FDC) matrices for each pencil beam are calculated and stored, based on the 9 uncertainty scenarios from fig. 2.5 and the 10 motion states of a 4DCT. This results in 90 FDC matrices from which different dose scenarios can be calculated. The expanded RST grid can finally be used for robust optimization.

$F_{\text{Robust 4D ITV}}(\vec{N})$ is used as cost function. Depending on the size of the target(s) and critical structure(s), a calculation could require up to hundreds of gigabyte of working memory. To handle the work load, machines with suitable computational power are necessary. Alternatively, smart software solutions might reduce the needed matrix size.

3.3 Patient data

The robust 4D ITV algorithm was tested on a set of 8 patients with 2 - 5 tumor lesions in the lung. In total there were 24 metastases. This set of patients represents a subset of the most complex cases of a patient cohort presented in Anderle [2016]. The patient numbering from Anderle is preserved in this thesis to maintain consistency.

For each patient, 4DCTs with 10 motion states (0-9) were obtained, where the end inhale phase is defined as the reference state (0). Additionally, a deformable image registration (DIR) is performed for each 4DCT which is used to transform all structure like CTVs and OARs from the reference state to the remaining motion states.

The average tumor volume was $28.8\,\text{cm}^3$, with a range of $0.4\,\text{cm}^3$ to $139\,\text{cm}^3$ for the reference state. The peak-to-peak motion was estimated from the 4DCTs to be 6.2 mm on average, with a range of 0.5 mm to 17 mm. A more detailed overview of the patient cohort is shown in table 3.1.

3.4 Treatment planning

In the study of Anderle et al., treatment planning was done on the geometrical ITV, which is generated by the union of the CTVs from all motion phases, extended by 3 mm PTV margins. In case of an overlap between target volumes and critical structures, the overlap is subtracted from the corresponding CTV in all motion phases. The original SBRT plans, which have been used for the radiotherapy treatments of these patients at Champalimaud Center for the Unknown (FC), also used 3 mm PTV margins. In comparison to both, the conventional 4D ITV approach by Anderle et al. and the SBRT photon treatment, the robust optimization is performed on the CTV(s) only. As described in chapter 2, the robust optimization algorithm generates safety margins by considering several uncertainty scenarios during optimization, namely errors in patient positioning and uncertainties in particle ranges. These uncertainties are described by two parameters, the setup uncertainty parameter and the range uncertainty parameter (see section 2.2.0.1 for more details). Hence, the extension of the safety margins depends on these two uncertainty parameters used during robust optimization. To maintain comparability with the 3 mm PTV margins used in Anderle et al., the setup uncertainty was chosen to be ±3 mm and the range uncertainty parameter was set to ±3.5 % for the robust optimization algorithm.

As described in chapter 2, errors in patient positioning can be modeled by shifting the patient's isocenter during treatment planning, more precisely by shifting in direction of the six major axis of CT coordinate system. Since treatment plan optimization is performed in the BEV coordinate system, the effective shift is obtained by calculating the lateral projections of the shifts in the CT coordinate system.

Like the BEV coordinate system itself, the effective shifts in the BEV system also depend on couch and gantry angle; however, in the BEV coordinate system, only planes orthogonal to the BEV axis are affected by the shifts in the CT coordinate system. The particle ranges are only marginally affected by adding or

Patient	Target	Volume [cm^3]	Peak-to-peak motion [mm]	Fractions [Gy(RBE)]	D_{plan} [Gy(RBE)]	N° of IMPT fields	Adjacent OAR
1	a	10.2	3.4	1 × 24.0	25.5	2	
	b	14.4	2.8	1 × 24.0	25.5	2	
3	a	136.0	12.0	1 × 27.0	28.5	3	Heart
	b	12.4	2.5	1 × 20.0	21.0	2	
	c	123.0	14.0	1 × 27.0	28.5	2	Heart
	d	80.7	17.0	1 × 22.0	23.1	3	
	e	86.7	6.6	1 × 20.0	21.0	3	Smaller airways
11	a	2.3	12.0	1 × 24.0	24.5	2	
	b	0.4	11.8	5 × 7.0	7.9	3	Heart, stomach, esophagus
13	a	3.8	5.8	1 × 24.0	24.5	2	
	b	4.3	0.8	1 × 24.0	24.5	2	
	c	2.7	3.4	1 × 24.0	24.5	2	
	d	3.1	2.1	1 × 24.0	24.5	2	
	e	0.5	0.5	1 × 24.0	24.5	2	
20	a	139.0	0.6	1 × 24.0	25.0	3	Smaller airways
	b	9.2	2.0	1 × 24.0	25.0	3	
21	a	4.0	9.0	1 × 27.0	27.5	5	Smaller airways, heart, esophagus
	b	0.8	7.8	1 × 24.0	24.5	2	
22	a	3.4	5.0	1 × 24.0	24.5	3	
	b	2.4	4.4	1 × 24.0	24.5	2	
	c	2.0	6.3	1 × 24.0	24.5	2	Heart
	d	2.4	6.4	1 × 24.0	24.5	2	Heart
23	a	20.6	7.4	1 × 24.0	24.5	4	Smaller airways
	b	27.1	6.0	1 × 24.0	24.5	3	Smaller airways, heart

Table 3.1.: Characteristics of the patient cohort, showing target volumes, peak-to-peak motions, dose fractions used, number of fields used in IMPT and OARs closer than 15 mm to CTV. D_{plan} = planned dose used in robust optimization.

subtracting an additional 3 mm of air while traversing patient tissue in BEV; however, manipulating the CT density by ±3.5 % creates significant particle range changes, as shown in figure 2.4.

The resulting average lateral, proximal, and distal extension of the applied RST grids are stated in table 3.2. These values are averaged over all 61 fields from all 8 patients found in table 3.1. It was found that shifting the patient's isocenter resulted in an average lateral extension of about ±3.0 mm on the RST grids. More precisely, the average shift was ±3.0 mm on the horizontal BEV axis and ±2.8 mm on the vertical BEV axis. Modifying the CT density effectively introduced shifts to particle ranges and extended the average RST grid by −2.5 mm in proximal and 4.1 mm in distal directions of the BEV axis. It should be noted that the proximal and distal extensions to the RST grid in the BEV system are stated in [$\mathrm{mm_{H2O}}$]. This is in contrast to table 2.1, where the range changes are stated in the CT coordinate system in mm.

	Lateral left [mm]	Lateral right [mm]	Lateral down [mm]	Lateral up [mm]	BEV proximal [$\mathrm{mm_{H2O}}$]	BEV distal [$\mathrm{mm_{H2O}}$]
Average	−3.0	3.0	−2.8	2.8	−2.5	4.1
Stddev	0.1	0.1	0.3	0.3	0.9	1.3
Median	−3.0	3.0	−3.0	3.0	−2.4	4.1
Min	−3.0	2.3	−3.0	2.1	−5.4	1.7
Max	−2.3	3.0	−2.1	3.0	−1.1	6.8

Table 3.2.: Average lateral, proximal, and distal extension of the RST grids in BEV system due to the uncertainty parameters used in the robust optimization algorithm (±3 mm setup uncertainty, ±3.5 % range uncertainty). The values are averaged over all 61 fields from all 8 patients (see table 3.1).

The treatment plan optimization was performed separately for each of the lung lobes since the entry channels did not overlap. As in the study from Anderle et al. [2018], due to the low density of lung tissue, an 80 mm PMMA bolus was used to account for the short particle ranges for targets in close proximity to the chest wall. In order to reduce the size of the calculation problem, large OARs, such as the heart or the lung, were each cropped to the volumes intersecting with the treatment fields only. In this study, the same OARs as used in Anderle et al. [2018] were used for the robust optimization. Only for one case, patient 20, which had been originally optimized without OARs, it was necessary to introduce 10 mm shells of lung tissue around the CTVs to reduce the increased normal tissue dose close to the CTVs which was caused by the robust optimization algorithm.

In order to maintain comparability, treatment planning parameters such as number of fields, couch and gantry angles, target points, spacing of RST grid, and size of ripple filter were taken from the treatment plans created in the study by Anderle et al. [2018]. As in the study by Anderle et al., the number of fields per target was selected, depending on the presence of adjacent OARs: (i) two opposing fields were used in absence of an OAR, (ii) two or more opposing or oblique fields were used in presence of critical structures in close proximity.

The RBE was calculated by applying LEM IV [Friedrich et al., 2014; Elsaesser et al., 2010], using the low dose approximation presented in Krämer and Scholz [2006]. Alpha-beta ratios of 6 and 2 were selected for target and normal tissue, respectively [Anderle et al., 2018].

The weight for the max dose term introduced in section 2.2.3 was set to 1.0 for all patients except for patient 1, where the value was set to 1.1. This was necessary in order to account for a higher normal tissue dose, since this patient was optimized without consideration of OARs.

Unlike in Anderle et al. [2018], the use of objective optimization was only necessary for patient 23. Here, a hard constraint was chosen for the smaller airways of the lung in order to reduce the maximum dose which prevented compliance with the dose volume limit defined in Benedict et al. [2010].

Voxel randomization

For further reduction of the calculation problem, random voxel sampling has been used throughout this study. Firstly, the volume V of a structure was split into an interior part V_{interior} and a boundary shell V_{boundary} by using a distance transformation. For both portions of the volume, random sampling parameters x_{interior} and x_{boundary} were chosen. During the setup, all voxels considered were assigned the probability of $1/x_{\text{interior}}$ and $1/x_{\text{boundary}}$, respectively, to be selected for the actual optimization, more precisely, only the fraction of $1/x \times 100\,\%$ of all voxels in V is considered in the optimization. In this study, the random sampling parameters were typically chosen to include more boundary than interior voxel ($x_{\text{interior}} > x_{\text{boundary}}$), due to their close vicinity to the dose gradients.

Quasi-random numbers were used to perform the random voxel sampling. Since these numbers depend on seed numbers, the resulting set of randomly chosen voxel only changes between executions of the same optimization in cases where the seed has changed. In order to maintain comparability between the resulting treatment plans of several executions of the same optimization, always the same seed numbers were used.

Since P3 and P20 both have CTVs larger than $100\,\text{cm}^3$, only a subset of states were considered for the optimization to further reduce the number of optimization voxels. To cover the target motion properly, two extreme states, 0 and 5 (end inhale and end exhale), as well as an intermediate state (7) were considered for the robust 4D ITV optimization. For all other patients, all 10 motion states were used.

For all 24 CTVs, a median of 50 % of all boundary target voxels (range of 25 % to 100 %) and 25 % of all interior voxels (range of 6.25 % to 100 %) were taken into account for the treatment plan optimization. For OARs, less voxels were considered for optimization: For boundary voxels, a median of 25 % with a range of 1.25 % to 50 % and for interior voxels a median of 6.25 % with a range of 1 % to 25 % were selected for optimization.

3.5 4D dose calculation

4D dose distributions were calculated for the robust and the conventional treatment plan from Anderle et al. [2018]. The 4D dose calculations were performed with TRiP4D using a patient specific DIR, to transform all partial state doses to the reference phase (0). Temporal correlations between patient's respiratory motion and the beam delivery was simulated with a dose delivery simulation tool (DSim) [Richter, 2012]. Machine parameters, including average spill duration and spill structure, were taken from the synchrotron accelerator at Heidelberg Ion-Beam Therapy Center (HIT). The DSim also simulated the dynamic intensity control (DIC) beam extraction method implemented at HIT, which creates a step sized spill structure with a flat intensity over time [Schömers et al., 2011]. Compared to the extraction method at GSI, this enables a more homogeneous particle extraction. Breathing motion was modeled with a periodical Lujan function using to different periods T (3.5 s and 5 s), each combined with two different starting phases ϕ (0° and 90°), resulting into four respiratory motion patterns. The Lujan function is

$$\sin^{2n}(t/T + \phi), n \in \mathbb{N}, \tag{3.3}$$

as presented in Lujan et al. [1999].

For each of these four respiratory motions patterns, 21 4D dose distributions were calculated, corresponding to 21 uncertainty scenarios as described in section 2.2.4, consisting of a combination of the nominal range scenario and over- and undershooting ranges, with shifts to the patient's isocenter in 6 major anatomical directions. In total, this results in 84 different 4D dose distributions per treatment plan.

3.6 Analysis

To evaluate the treatment plan quality, a RA, as described in chapter 2, was performed. For the RA, dose volume histograms (DVHs) have been calculated for each of the 84 4D dose distributions. From this set of DVHs, average values for different dose measurements can be determined. The target coverage was evaluated by considering the dose distribution for the CTV and calculating V95, D95, D99, the D50 spread and the homogeneity index (HI).

For critical organs, the volume dose D_{vol} and the maximum dose D_{max}, corresponding to the dose limits defined for different fractionation schemes in Benedict et al. [2010] were calculated. The V5 value was additionally calculated to assess the low dose exposure to OARs. The D_{vol} and D_{max} values were normalized to the limits stated in Benedict et al. [2010]. If a value exceeded 100 %, the constraint was counted as violated.

3.7 Example patient

To evaluate the performance of the robust 4D ITV optimization in a more comprehensive manner, patient 23 is presented in more detail in the following section.

3.7.1 Results

Although patient 23 has only one tumor per lung lobe, this case posed a challenge for the conventional and the robust optimizer, due to the close vicinity between the CTV and the smaller airways in each lung lobe. At some locations, the distance between targets and smaller airways is less than 10 mm, generating a competitive situation between providing sufficient target coverage and adequate OAR sparing. Both the original SBRT treatment plans and the conventional 4D ITV carbon ion plans from Anderle et al. tried to find a compromise between these two opposing objectives. In case of doubt, OAR sparing was favored over target coverage. For the conventional treatment plan, there was the need to sacrifice target coverage of the CTV in the left lung lobe to spare the smaller airways adequately already in the “nominal dose scenario”, which does not consider any additional range or setup errors. The result of this compromise can be seen in figure 3.4(a,c) as an axial dose cut for both the conventional and robust treatment plan. The dose distributions of both plans show a cold spot in target coverage for the medial area of the left CTV, which will further on be called “low dose area”. For the robust plan, the low dose area between the left CTV and smaller airways was already larger than for the conventional case, and in the right lung lobe, the low dose area in the CTV is even more pronounced than for the conventional plan. For the robust treatment plan, this means an additional sacrifice of target dose coverage in order to provide improved sparing of the SA.

The ideal treatment plan would generate a DVH, where the CTV dose curves converge to the ideal step-shape for all considered uncertainty scenarios, and where the CTV dose curves provide a steep dose fall-off shortly after 100 % of the target dose is reached. This would result in a narrow uncertainty bands

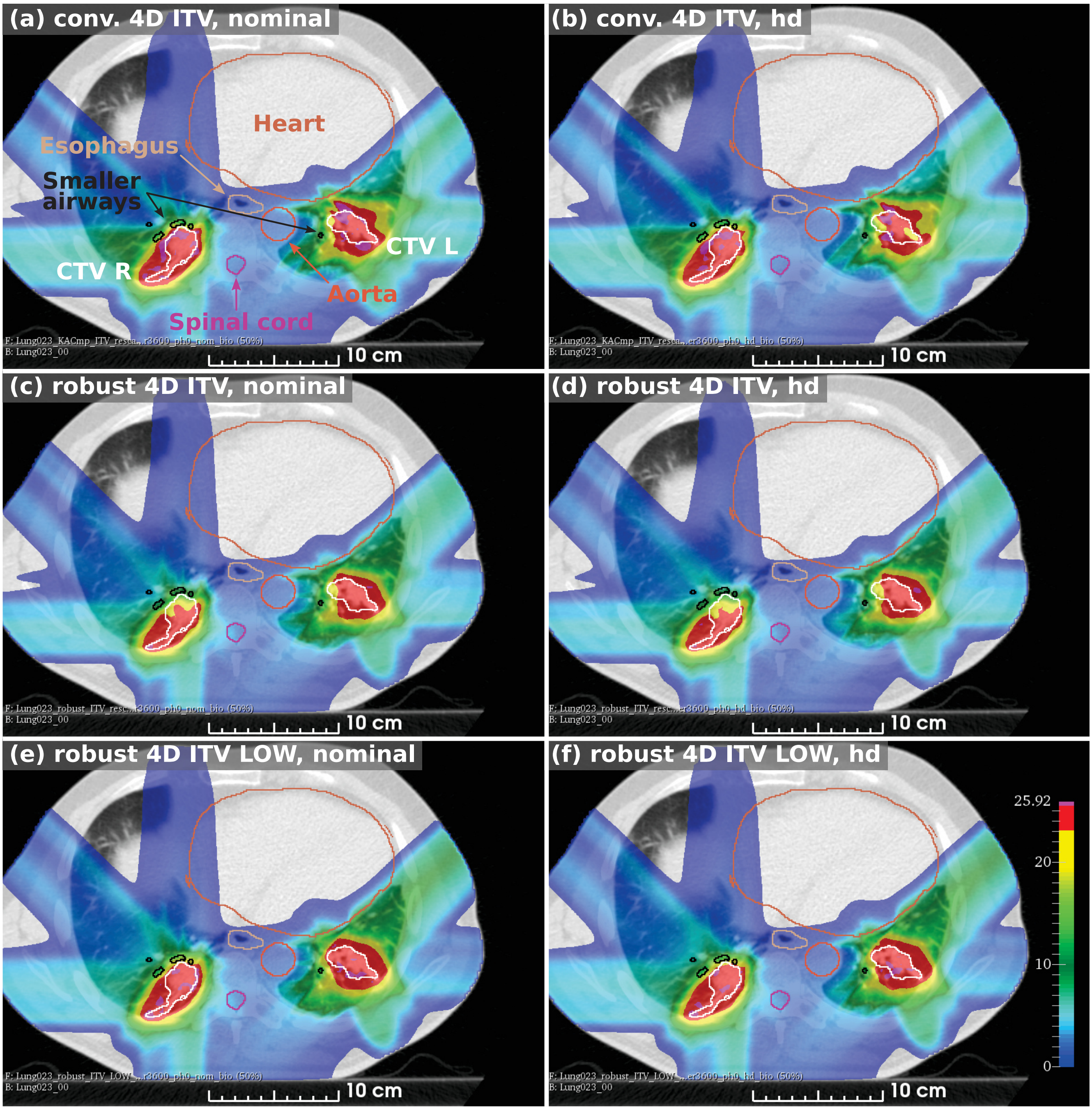

Figure 3.4.: Axial view of 4D dose distribution overlaid on CT reference phase for patient 23 in the nominal (nom) and high density (hd) scenario with Lujan period of 3.6 s and starting phase of 0°. Panel (a) and (b) show the dose distributions resulting from the conventional optimized plan with right and left CTVs (white) as well as the smaller airways (black) and heart (brown) as critical structures. Panels (c) and (d) shows the dose distributions from the robustly optimized treatment plan and panels (e) and (f) show the robust plan with low OAR weights (LOW). Dose is shown in Gy(RBE).

around the average DVH curves and that the CTV objective of $D_{99\%} \geq 100\,\%$ is fulfilled in the majority of cases. At the same time, the ideal plan would meet the DVH constraints for both the volume dose and the maximum delivered dose for each OAR in all uncertainty scenarios under consideration. In the following three figures, the dose volume constraint for the smaller airways is indicated in the DVHs with stars. For the DVH of the ideal treatment plan, all OAR curves would stay left and below of the corresponding star symbols.

Figure 3.5 shows the result of the RA for the plan optimized with conventional IMPT using the 4D ITV approach. The desired target coverage for the right CTV ($D_{99\%} \geq 100\,\%$) was fulfilled in 4 of 84 scenarios as the average $D_{99\%}$ is only $(93.1 \pm 6.7)\,\%$. The target coverage was limited by the competing constraint for smaller airways of $D_{0.5\mathrm{cc}} \leq 12.4$ Gy(RBE) which was met in 31.0 % of the uncertainty scenarios.

For the left lung lobe, there was a large uncertainty band around the average DVH curve of the CTV. This exemplifies the situation of the conventional optimization failing to provide adequate certainty for delivering the planned dose distribution under the presence of patient setup or range uncertainties. The smaller airways in the left lung lobe benefit from the reduced target coverage ($D_{99\%}$ is $(63.0 \pm 8.1)\,\%$), since the corresponding dose volume constraint is fulfilled in 63.1 % whereas the CTV constraint is not met in any uncertainty scenario.

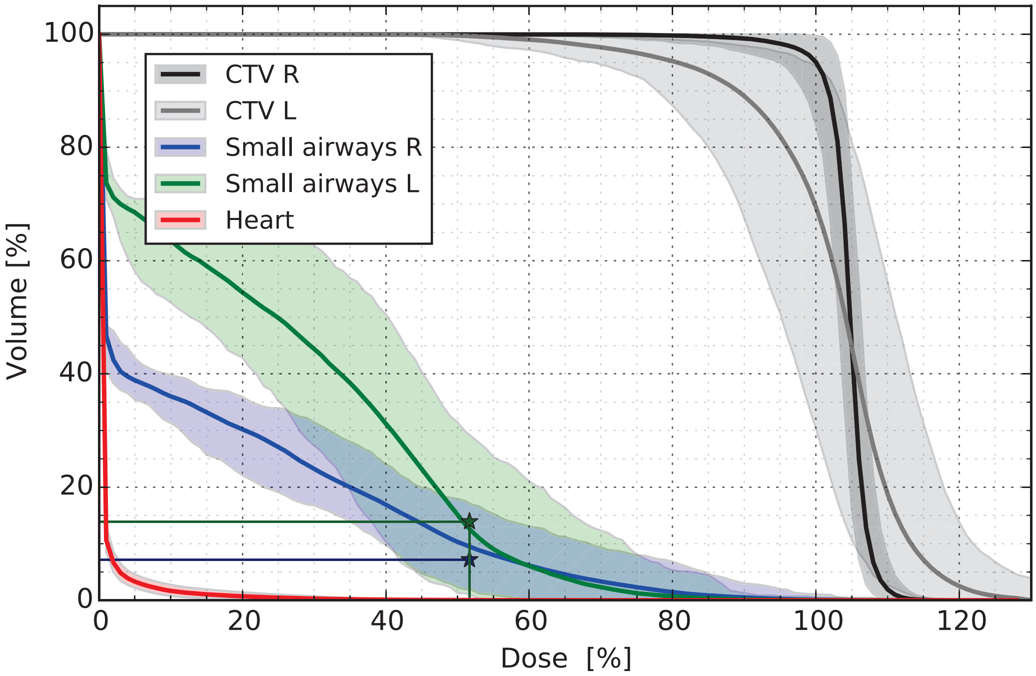

Figure 3.5.: DVH of the conventional treatment plan for patient 23. The bold lines are average DVH curves and the light colored areas are uncertainty bands, depicting the envelope of all 84 4D dose distributions. Star symbols indicate the dose volume constraints for the smaller airways ($D_{0.5\mathrm{cc}} \leq 12.4$ Gy(RBE)). The SA constraint is fulfilled in 31.0 % and 63.1 % of all uncertainty scenarios for the right (blue) and the left smaller airways (green), respectively.

Using robust optimization with similar voxel weights as for the conventional plan can help to meet the desired OAR objectives. The DVH from the RA for the robust plan is shown in figure 3.6. The dose volume constraint of $D_{0.5\mathrm{cc}} \leq 12.4$ Gy(RBE) for the smaller airways was fulfilled in 75.0 % of the cases for the right SA and in 100.0 % for left SA. This constraint reduced target coverage for the both CTVs. The D99 objective for the CTVs could not be accomplished in any of the considered uncertainty scenarios.

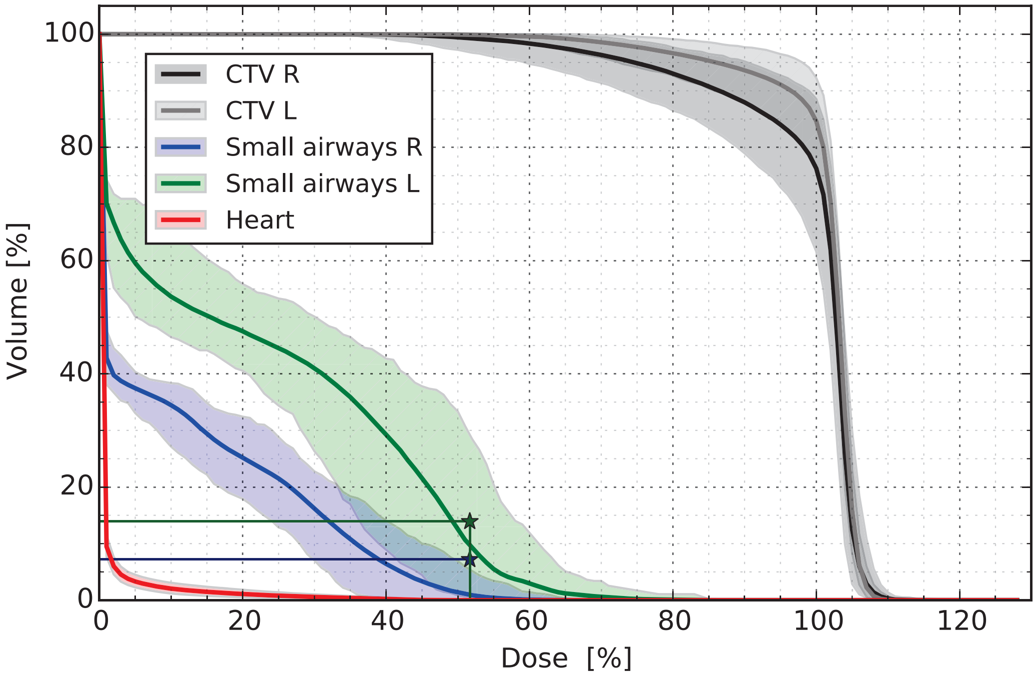

Figure 3.6.: DVH of the robust treatment plan for patient 23. The bold lines are average DVH curves and the light colored areas are uncertainty bands, depicting the envelope of all 84 4D dose distributions. Star symbols indicate the dose volume constraints for the smaller airways ($D_{0.5cc} \leq 12.4$ Gy(RBE)). The SA constraint is fulfilled in 75.0 % and 100.0 % of all uncertainty scenarios for the right (blue) and the left smaller airways (green), respectively.

The DVH for the robust plan with low OAR weights (further on called “robust LOW” plan) is shown in figure 3.7. For the robust LOW plan, the OAR weights were chosen to be smaller than the CTV weights during robust optimization. This enabled an improvement of the robustness to the target coverage by increasing OAR doses, in this case the dose to the smaller airways. In addition to the improved target coverage, the uncertainty band was reduced and the average homogeneity index was increased. Though the DVH of the robust LOW plan almost showed the ideal step-shape, the CTV objective of $D_{99\%} \geq 100\,\%$ was only met in 2.4 % for the right CTV and in 6.0 % for the left CTV. Figure 3.4(e) shows the axial view of the dose distribution for the robust LOW plan.

The right column of figure 3.4 shows the axial cuts of the dose distributions of all three plans where CT density is increased by 3.5 %. The high density (*hd*) scenarios exemplary demonstrates the performance of the robust optimization algorithm under the presence of uncertainties. Since increasing CT density will result in a range undershoot of the planned treatment fields, the impact on the dose distribution can be drastic as seen in the increased number of hot and cold spots. When comparing the nominal and the *hd* dose distribution for the conventional plan, both CTVs contain hot spots. Especially the left target sustains extensive cold spots which is in the order of several Gy(RBE) in some areas.

Apart from the deliberately created cold spots close to the smaller airways, the robust dose distribution is much more homogeneous and only contain small hot spots, as seen in the dose distribution in figure 3.4(c) and (d).

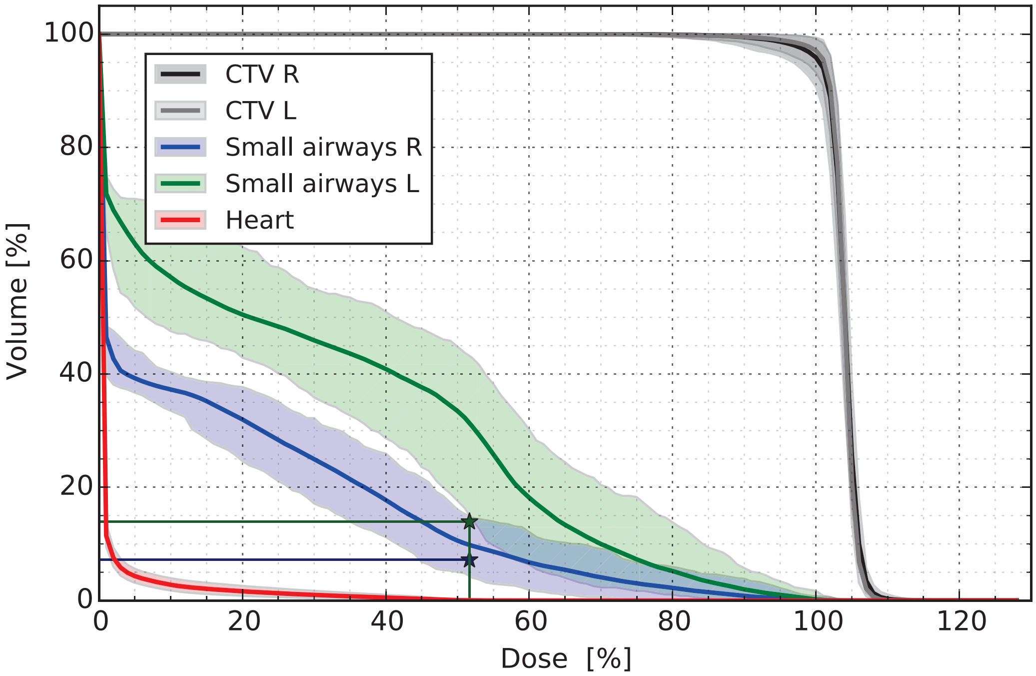

Figure 3.7.: DVH of the robust LOW treatment plan for patient 23, where the OAR voxel weights were smaller than CTV voxel weights during optimization. The bold lines are average DVH curves and the light colored areas are uncertainty bands, depicting the envelope of all 84 4D dose distributions. Star symbols indicate the dose volume constraints for the smaller airways ($D_{0.5cc} \leq 12.4\,\mathrm{Gy(RBE)}$). The SA constraint is fulfilled in 0.0 % and 28.6 % of all uncertainty scenarios for the right (blue) and the left smaller airways (green), respectively.

The major difference between the robust LOW plan and the robust plan can be seen around the boundary areas of the target volume, next to the smaller airways. Since the weights for the target voxels were set to be larger than the weights for the OAR voxels for the robust LOW plan, the cold spots in the target vanish. A similar effect can be seen in the presence of uncertainties, which can be exemplarily seen in figure 3.4(f) for the axial dose distribution with an increased CT density by 3.5 %. Especially when compared to the conventional and the robust plan, the robust LOW plan shows almost no deterioration of the dose distribution for the *hd* scenario.

CTV coverage

The results for all the dose measurements of the target, including all 21 uncertainty scenarios and all 4 patient motions, are summarized as boxplots in figure 3.8, resulting in 84 values per boxplot. In the boxplots, the black lines indicate the median values, and the black X's symbols denote the average values. The boxes describe the 1$^{\mathrm{st}}$ and 3$^{\mathrm{rd}}$ quantiles, and the whiskers represent 3 standard deviations, including approximately 1 % to 99 % of all values in the distribution of a dose measurement. Outliers are represented by crosses. Since the distribution of these values is not Gaussian, statistical significance has been calculated by using an unsigned rank test. The resulting p-values are divided into three different classes: $^{*} \mapsto p < 0.05$, $^{**} \mapsto p < 0.01$, $^{***} \mapsto p < 0.001$.

The boxplots for the conventional, the robust and the robust LOW plan are presented adjacent to each other. Both robust plans show distributions of dose measurements V95, D95 and D99 which are significantly different from the conventional plan, having p-values smaller 0.001. Considering the plan quality, the robust LOW plan leads to the best target coverage, followed by the conventional and the robust plan in descending order. These results are in agreement with the results described in previous paragraphs and the DVH figures. The objective of $D_{99\%} \geq 100\,\%$ is fulfilled in 4.2 % of the uncertainty scenarios for the conventional plan, in 0.0 % of the scenarios for the robust plan and in 10.7 % for the robust LOW plan.

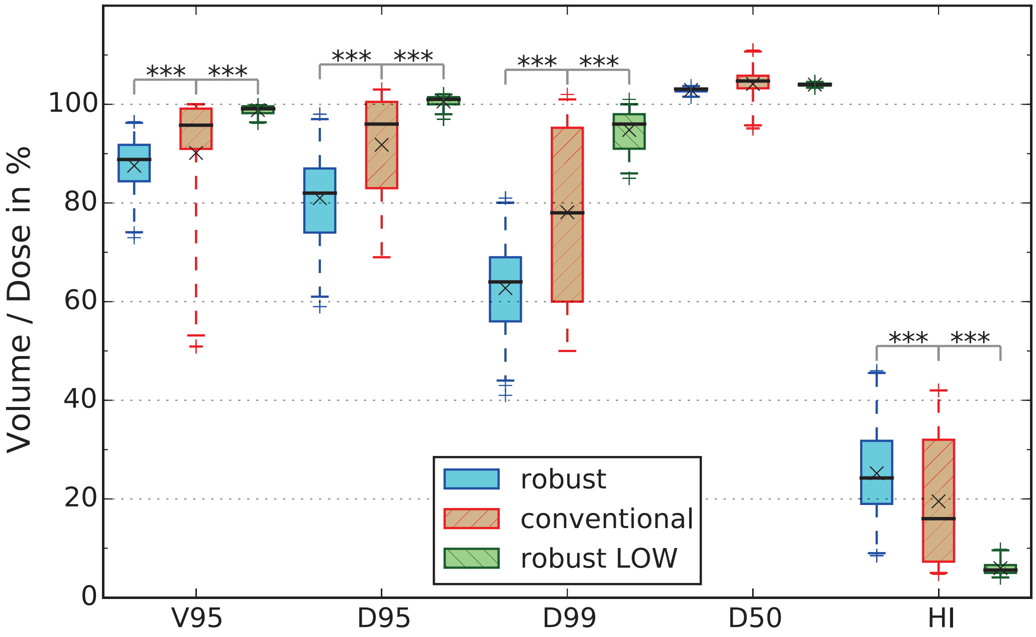

Figure 3.8.: CTV coverage of patient 23 shown as boxplots of V95, D95, D99, D5 and HI for the conventional, the robust and the robust with low OAR weights plan. The black line indicates the median value whereas the black X denotes the average value. The boxes represent the 1st and 3rd quantiles, while the whiskers represent the environment of 3 standard deviations. Statistical significance is tested between the conventional and the two robust plans and is indicated by a p-value calculated with an unsigned rank test ($^{*} \mapsto p < 0.05$, $^{**} \mapsto p < 0.01$, $^{***} \mapsto p < 0.001$).

The width of the D50 distribution describes the width of the uncertainty band around the 100.0 % target dose level. As described in chapter 2, it is a suitable measure to assess plan robustness. Hence, the width of the D50 distribution is more important to assess plan robustness, than the median or average value of the D50 distribution. For both robust plans, the D50 width was considerably reduced. For the robust plan, the complete distribution of D50 values lies around the median value of 103.1 %, and falls within an interval range of 2.3 %. For the robust LOW plan, the total width of the distribution is further reduced to 1.3 % around a median value of 104.0 %. The conventional plan has a D50 median value of 104.7 % with a interval width of 16 %.

In an ideal DVH, with a step-shaped target dose distribution, values for the homogeneity index would be very small, almost approaching zero. The values for homogeneity index are significantly worse for the robust plan than for to the conventional plan, whereas the robust LOW plan yields significantly better HI values. The p-values, in both cases, are smaller than 0.001.

OAR exposure

The evaluation of the dose measurements for treatment targets must always be considered with the dose delivered to surrounding critical organs. Values for dose exposure to the most important organs (smaller airways, heart, esophagus, spinal cord, aorta and ipsilateral lung) are summarized for all 84 uncertainty scenarios in figure 3.9 as boxplots. The ipsilateral lung consists of the volume of the affected lung lobes subtracted by the volumes of the corresponding CTVs. Both, patients 20 and 22, have only one lung lobe which is affected by a tumor. For theses two cases, the corresponding ipsilateral lung volumes do not include the healthy lung lobes. The values for the dose volume, D_{vol}, and the maximum dose delivered, D_{max}, are all normalized to their corresponding limits from Benedict et al. [2010]. This means that a constraint is violated if the D_{vol} or D_{max} values exceeds 100 %.

The presented patient cohort was originally treated with photons using a stereo tactic radio therapy (SBRT). For SBRT, almost the entire patient is covered by the huge number of photon treatment fields, also generating areas of tissue volume which receive low levels of photon radiation dose. As in Anderle, the V5 value is used here to assess the amount of low dose delivered to the OARs .

For patient 23, the boxplot of the smaller airways includes the dose values of the smaller airways of the right and left lung lobes. In this plot, the average dose volume, D_{vol}, for the conventional plan was 102.6 % with a range of 84.2 % to 129.7 %. The constraint for the SA of $D_{0.5cc} < 12.4\,\mathrm{Gy(RBE)}$ was only fulfilled in 38.1 % of the 84 uncertainty scenarios. For the robust plan, the D_{vol} is 84.8 % with a range of 66.8 % to 101.6 % which met the SA constraint in 96.4 % of the scenarios. The D_{vol} for the robust LOW plan is 117.6 % with a range of 97.7 % to 144.2 %, which fulfilled the SA constraint in 10.7 % of the uncertainty scenarios.

As for the D_{vol} values, the robust plan yielded the smallest D_{max} values. The distribution of the maximum dose values of the conventional plan were significantly higher than for the robust plan. The highest D_{max} values were generated by the robust LOW plan. For all three plans, the limit for the D_{max} value was exceeded for all uncertainty scenarios; however, according to Anderle [2016], the maximum dose constraint had already been deliberately violated for the actual photon treatment with SBRT. The V5 values, which were used to assess the low dose exposure, were significantly lower for the robust and robust LOW plan compared to the conventional plan. As the V5 values of both robust plans were even smaller than for the conventional plan, they were considered as uncritical.

For the remaining OARs, the dose measurements did not show a noticeable pattern. Nonetheless, the dose values all fell within the constraints.

The D_{vol} values for the heart were significantly higher for the two robust plans. For the conventional plan, the median D_{vol} was 15.0 %. In contrast, the median D_{vol} was 19.5 % and 30.0 % for the robust and the robust LOW plans, respectively. However, the maximal doses were significantly smaller for the two robust plans. While the conventional plan had a median D_{max} of 76.3 %, the robust and the robust LOW plans yielded median D_{max} values of 52.4 % and 62.7 %, respectively. The V5 values were below 5 % for all plans and therefore uncritical. The corresponding p-values were smaller 0.001.

The volume dose and maximal dose of the esophagus were below 20 % for all plans. Nonetheless, the values of D_{vol} were significantly smaller for both robust plans. The D_{max} values of the robust plan were significantly smaller than those of the conventional plan, but for the robust LOW plan, they were

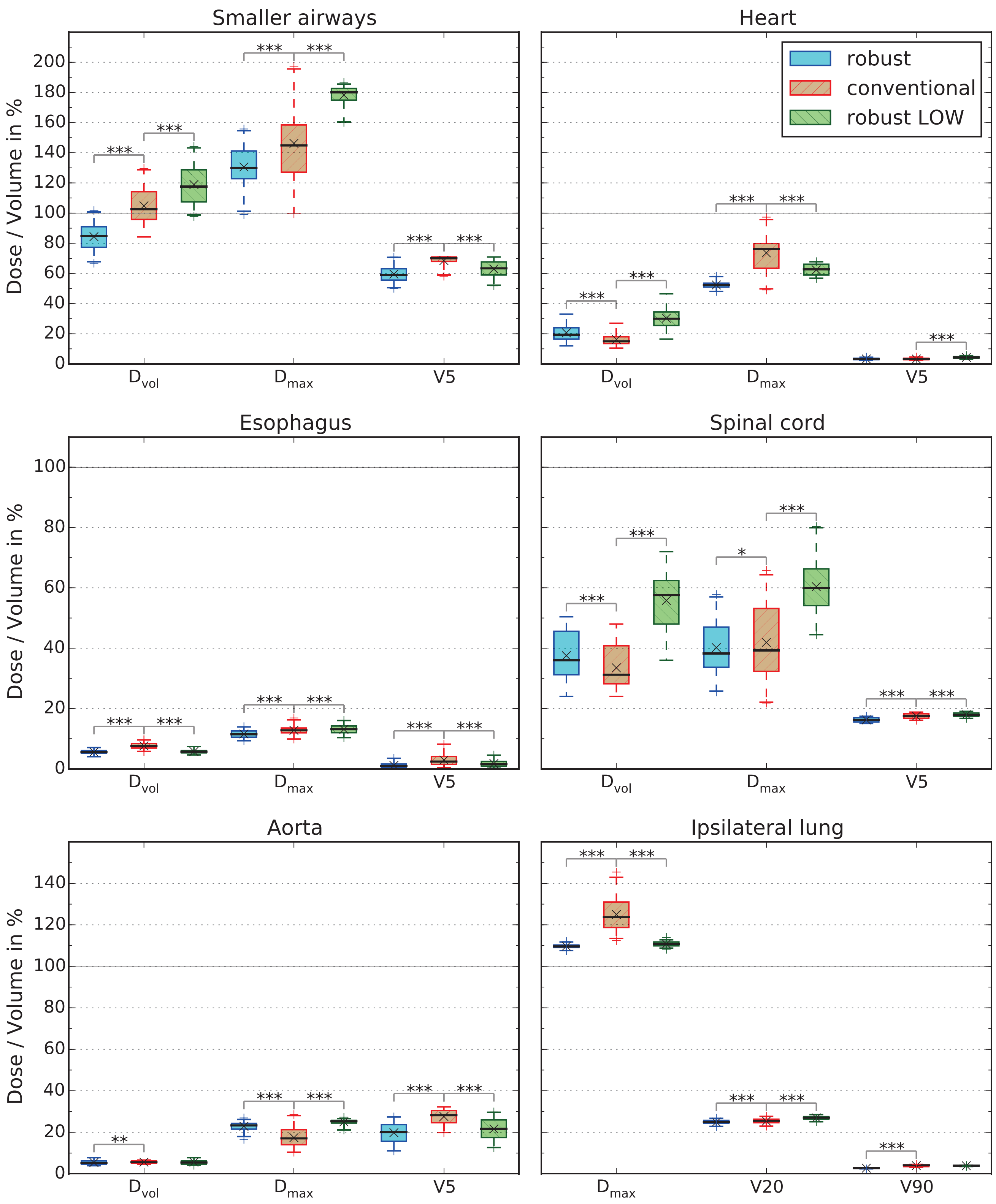

Figure 3.9.: OAR doses of patient 23 shown as boxplots of D_{vol}, D_{max}, V5 as well as D_{max}, V20 and V90 for the ipsilateral lung. Results are shown for the conventional, the robust and the robust with low OAR weights plan. The black line indicates the median value whereas the black X denotes the average value. The boxes represent the 1^{st} and 3^{rd} quantiles, while the whiskers represent the environment of 3 standard deviations. Statistical significance is tested between the conventional and the two robust plans and is indicated by a p-value calculated with an unsigned rank test ($^{*} \mapsto p < 0.05$, $^{**} \mapsto p < 0.01$, $^{***} \mapsto p < 0.001$).

significantly higher. The V5 values were below 10 % for all plans, but the two robust plans yielded significantly smaller V5 values. The p-values were all less than 0.001.

Larger variations can be seen for the spinal cord. The D_{vol} values for the conventional plan were significantly lower than for the two robust plans where median values were 31.2 % for the conventional and 36.0 % for the robust plan. Additionally, the D_{vol} values of the robust LOW plan were even higher than for the two remaining plans, with a median value of 57.6 %. The D_{max} values for the robust LOW plan were significantly higher than for the conventional or the robust plan. The median value was 59.9 %, whereas the median values for the conventional and robust plan were 39.3 % and 38.3 %, respectively. The statistical significance between the distribution of D_{max} values of the conventional and the robust plan was less pronounced (p-value < 0.05).

The volume dose values for the aorta were below 10 % for all three plans. The D_{vol} values for the robust plan were slightly lower than for the conventional plan, but differed significantly with a p-value below 0.01. The maximal dose for the conventional plan was significantly smaller than for the two robust plans. The median value was 17.1 % for the conventional plan, and for the robust and robust LOW plan, the median values were 23.3 % and 25.3 %, respectively. Concerning the V5 values, the situation was opposite here; the median values for the robust and the robust LOW plan were significantly smaller at 20.1 % and 21.7 %, and the conventional plan had a median V5 at 28.2 %.

As there was no limit stated for the maximal point dose for the lung, the D_{max} value was normalized to the target dose of the tumor in the affected lung lobe. All dose measurements for the lung were evaluated for the volume of the lung lobe minus the clinical target volume(s). V20 and V90 values were calculated to assess the low and the high dose exposure of the ipsilateral lung lobe, respectively. For both robust plans, the median maximal dose was significantly smaller, measuring at 109.6 % and 110.8 % for the robust and the robust LOW plans, respectively, as compared to 123.7 % maximal dose for the conventional plan. The V20 values lied around 25.0 % for all three plans. Nonetheless, compared to the conventional plan, the V20 distribution was significantly smaller for the robust plan and significantly larger for the robust LOW plan. The V90 values were smaller than 5.0 % for all three plans, and the robust plan was significantly smaller than the conventional plan. The p-values were all smaller than 0.001.

3.7.2 Discussion

Low dose area

The dose areas, as exemplarily shown for the robust plan in figure 3.4(c & d), are a consequence of the choice of voxel weights and the current implementation of the optimization algorithm. Overlaps of the target volume with adjacent critical organs, result in both structures sharing the same voxels in the CT image. The implementation of the voxel-based optimizer in TRiP4D requires that any give voxel may only be assigned as a target *or* an OAR exclusively. The decision whether to classify a voxel as target or OAR is determined by the voxel weights which are a manual input of the treatment planner. If the OAR weights are larger than the target weights, the corresponding overlap voxels between target and OAR are counted as OAR, and vice versa.

During the robust optimization, uncertainty scenarios such as shifting the patient's isocenter, do not exclusively affect the CTV(s), but also critical organs such as the smaller airways in case of patient 23, are shifted. Having adopted the same relation between target and OAR weights as described in Anderle et al., moving the CTV in direction of an OAR and an OAR in direction of the CTV, will result in at least a low dose area of about the doubled size as compared to conventional plan. The extension of the low dose area depends on the setup uncertainty parameter initially used in the robust optimization. In this study, a shift of ±3 mm resulted in a extension of the low dose area in the order of about 6 mm. Depending on the choice of the beam angles, the shift caused by setup error scenario and the shift due to range overshoot may superpose, resulting in a even larger extension of the low dose area.

This situation occurred in patient 23 for the right CTV (see figure 3.4(c)). As described above, the emergence of these low dose areas can be interpreted as an inherent effect of the current implementation of robust optimizer with its exclusive assignment of voxels as target *or* OAR; however, the voxel-wise worst-case optimization also generates unrealistic dose distributions consisting of different uncertainty scenarios for adjacent voxels, which are highly unlikely to occur at the same time. For example, a setup error which shifts the patient's isocenter in direction of the OAR can not at the same time shift the OAR in the opposite direction. An extension to the worst-case method which can discriminate unrealistic cases could be implemented, which would neglect one of the two shifts and would result in a low dose area of just 3 mm.

CTV coverage

The low fulfillment rates of the $D_{99\%}$ objective for all three plans are due to several factors. First, for the conventional and the robust plans the focus was to find a balance between target coverage and OAR sparing (in case of patient 23 the adjacent smaller airways). To achieve this, overlapping areas of the target and the smaller airways were cropped from the CTV volume and higher voxel weights were used for the smaller airways than for the target voxels. Compared to the robust algorithm, the conventional IMPT algorithm only optimized a 4D ITV plan on the nominal scenario. As the robust optimizer functions by trying to fulfill the OAR objective in all 9 uncertainty scenarios, sacrificing target coverage is inherently necessary. This also explains why the robust plan cannot meet the CTV objective at all, whereas the conventional plan can fulfill it in at least 4.2 % of the uncertainty scenarios.

Compared to the conventional and robust plans, using the robust LOW plan led to an average DVH curve which converged more to the ideal step-shape and to a considerable reduction of the uncertainty bands, as can be seen in figure 3.7. Nonetheless, with 10.7 % of all uncertainty scenarios, the CTV objective was fulfilled in less scenarios than expected. This is due to the usage of the same planned target dose values during optimization as for the robust plan. Since the dose fall-off in the DVH for the robust LOW plan was steeper than for the two other plans, the fulfillment rate for the CTV objective could be straightforwardly improved by increasing the planned target dose at the cost of additional dose to normal tissue.

Robustness of CTV coverage

The gain in robustness is best described by the reduced whisker lengths in the boxplots for the D50 values of the two robust plans (as seen in figures 3.6 and 3.7). The whiskers contain all values within the 3σ-interval from approximately 1 % to 99 %. Compared to the conventional plan, the whiskers were very close to the median value for both robust plans. In combination with small HI values, this describes a considerable reduction of the uncertainty band around the dose fall-off in the DVH, as can be seen for the robust LOW plan. For the robust and the conventional plans, the HI values were increased due to the close proximity of the tumor and the smaller airways. Although the uncertainty band was smaller for the robust plan, than for the conventional plan, this reduced HI values caused, that the D99 constraint could not be fulfilled; however, when voxel weights are increased to favor the target voxels during the optimization, the HI value improves appreciably for the robust LOW plan, as described above.

Increased robustness of the robust and robust LOW plans was also expressed in dose distributions which were less prone to hot or cold spots compared to the conventional plan. This is due to the smoothing of internal dose gradients by the robust optimizer. Compared to the robust LOW plan, this refers to the portion of the CTV dose distribution of the robust plan which was not deliberately reduced due to the choice of target and OAR voxel weights in order to increase OAR sparing. Expressed mathematically, the robust dose distributions can be described as more convex on the 100 % iso-dose value.

OAR exposure

Since the OAR exposure differs for each organ in consideration, it is not possible to universally describe one of the three plans as superior to the others. The advantages and disadvantages of each plan type must be carefully weighed against each other on a case by case basis.

When considering the heart, none of the three plans violated the volume or maximal dose constraint. For the robust or robust LOW plans, the volume dose was slightly increased compared to the conventional plan, but the maximal dose was therefore significantly reduced. The difference between the conventional and the two robust plans was most pronounced in the overall reduction of the maximal point dose measurements. Although the heart has not been considered during the treatment plan optimization, the robust plans yield reduced maximal point heart doses as described above, which prefers the robust plans over the conventional plan.

For the spinal cord, all three plans likewise do not violate the given constraints. As for the heart, the spinal cord was not explicitly considered as an OAR during optimization. The robust LOW plan consequently produces significantly more volume and maximal dose. Between the conventional and robust plan, in this situation the conventional plan is preferred. Hence, in cases where the spinal cord is critical, the robust LOW plan is less preferable.

Interestingly, there was a large reduction in maximal dose to the healthy lung tissue for both robust plans. Although the robust LOW plan yielded a superior target coverage, it did not increase the dose delivered to the lung. The D_{max} stayed more or less at the same level as the maximal dose distribution of the robust plan. This could be due to the higher convexity of the dose distributions for the robust plans, as described above for the increased robustness of the CTV coverage. When less hot spots are produced, less hot spots can lie outside of the CTV in healthy lung tissue.

The creation of cold spots in close vicinity to the OARs was an inherent consequence of the robust optimization when target weights were chosen to be smaller than the OAR weights. This choice of voxel weights ensured meeting the dose volume constraints in the majority of considered uncertainty scenarios. For patient 23, the difference between the conventional and robust plan was very pronounced for the smaller airways. Averaging the smaller airways in both lung lobes, the robust plan fulfilled the DVH constraint in 96.4 % of the uncertainty scenarios, whereas the conventional plan only in 38.1 % of the scenarios. The robust LOW plan ensured a superior dose coverage, as compared to the conventional and robust plans, but did so by neglecting smaller airways sparing. The conventional plan is a compromise between the two extremes of the robust plan, which focused on OAR sparing, and the robust LOW plan, which focused on target coverage. However, the conventional plan quality was reduced by large uncertainty bands, especially for the left CTV. Apart from the nominal case, safe delivery of the planned dose distribution could not be ensured in presence of uncertainties. As patient 23 is the most complex patient from the cohort, there is no clear indication on which plan is the most beneficial. Further changes would need to be made to the robust optimization algorithm to produce dose distributions more like that of the conventional plan. Potentially, voxels which represent both target and critical organ would need to be assigned as target voxel *and* OAR voxel during robust optimization. This capability is currently not available in TRiP4D.

In conclusion, robust optimization enables a reduction of uncertainty of the delivered dose distribution also for a wide range of different optimization weights. This also enables a range of clinical choices which can be personalized to each patient.

3.8 Results — patient study

CTV dose coverage

In this section, the resulting robust treatment plans are compared against the conventionally optimized plans for all eight patients. Figure 3.10 describes the target coverage for all 24 tumors as boxplots of different dose measures. For each patient 21 uncertainty scenarios and 4 different patient motions are considered, resulting in each boxplot consisting of $24 \cdot 21 \cdot 4 = 2016$ values. In the boxplots, the black lines indicate the median values, and the black X's symbols denote the average values. The boxes describe the 1st and 3rd quantiles, and the whiskers represent 3 standard deviations, including approximately 1 % to 99 % of all values in the distribution of a dose measurement. This environment will further on be referred to as 3σ-interval. Outliers are represented by crosses. Since the distribution of these values is not Gaussian, statistical significance has been calculated by using an unsigned rank test. The resulting p-values are divided into three different classes: $^{*} \mapsto p < 0.05$, $^{**} \mapsto p < 0.01$, $^{***} \mapsto p < 0.001$.

The dose coverage of the CTVs is described by V95, D95 and D99 values. Considering the volume receiving 95 % of the target dose (V95), there was no significant difference between the robust and the conventional 4D ITV plan. Nevertheless, it is worth noting that the 3σ-interval contained values down to 28.2 % of the volume for the conventional plan, compared to the robust plan, where the lower limit of this environment was 60.0 % of the volume. The D95 distribution, which describes the dose given to 95 % of the CTV volume, looked similar for both optimization types, but was slightly in favor of the conventional plans. For the D99 values, the median values were identical at 98.0 %, but the average values were slightly different with (93.1 ± 12.1) % for the robust and (94.0 ± 11.6) % for the conventional plans, respectively. The bottom limit of the 3σ-interval was 6.0 % lower for the robust plans, and with a p-value smaller than 0.001 in favor of the conventional 4D ITV plans. Additionally, the conventional plans could fulfill the objective of D99 $\geq$ 100 % in 38.5 %, whereas the robust plans could only fulfill the objective in 31.9 % of cases.

The D50 and HI values are used to measure plan robustness against patient setup errors and range uncertainties. The width of the 3σ-interval is used to determine the width of the D50 values, as it also

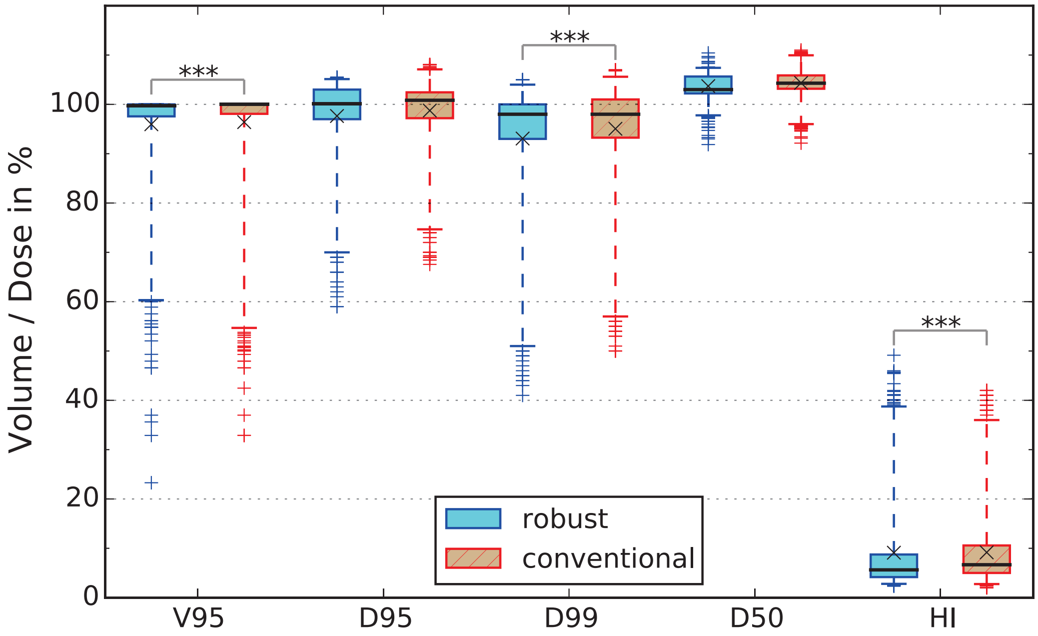

Figure 3.10.: CTV coverage summarized for all patients, shown as boxplots of V95, D95, D99, D5 and HI for the conventional and the robust plan. The black line indicates the median value whereas the black X denotes the average value. The boxes represent the 1^{st} and 3^{rd} quantiles, while the whiskers represent the environment of 3 standard deviations. Statistical significance is indicated by a p-value calculated with an unsigned rank test ($^{*} \mapsto p < 0.05$, $^{**} \mapsto p < 0.01$, $^{***} \mapsto p < 0.001$).

describes the width of the uncertainty bands at the steep dose fall-off in the DVHs around 100 % mark of the target dose. For the conventional plans, the D50 width was 37.9 % whereas for the robust plans this width was reduced to 9.7 %. The width of the D50 3σ-interval must be considered in conjunction with the HI value, as the HI describes how close the dose fall-off in the DVH is to the ideal step-shape. The median values for the HI were 5.6 % for the robust and 7.4 % for the conventional plans, respectively. The distribution of the HI values for the robust plans was significantly different from the conventional plans.

OAR exposure

The results for the dose measurements for the most important critical organs are summarized for all 8 patients in figure 3.11. For smaller airways, heart, esophagus, spinal cord, aorta and trachea, the volume dose D_{vol}, the maximal dose D_{max} and V5 values are shown. The values for D_{vol} and D_{max} were normalized to their corresponding limits as stated in [Benedict et al., 2010]. Due to the normalization, a constraint was counted as violated, when the value exceeded 100 %. Since the volume dose to the lungs is low for all cases and the constraint was never violated, the D_{vol} lung data is not shown. As lung tissue is counted as parallel tissue and Benedict et al. [2010] states no limit for the maximal lung dose, in this study, the maximal lung dose was normalized to the target dose. To asses the low dose and high dose exposure, V20 and V90 values were stated for the affected lung lobes. Except for trachea and smaller airways, each boxplot consists of 672 values. The numbers correspond to all 8 patient dose distributions for 4 different breathing motions combined with 21 uncertainty scenarios. Due to missing contours for trachea in patient 13 and for smaller airways in patient 22, the corresponding boxplots consist of only 588 values.

For heart, esophagus, spinal cord and aorta, D_{vol}, D_{max} and V5 were significantly smaller for the robust plans. The corresponding p-values were below 0.001, apart from D_{vol} and D_{max} values for the spinal cord, where the p-values were only below 0.01. It is to mention that for both kinds of treatment plans, the maximal dose for the heart was violated in 9.1 % and 8.3 % for the robust and the conventional plans, respectively. Similarly for the esophagus, the D_{max} constraint was violated in 2.8 % and 10.1 % of scenarios for the robust and conventional plans, respectively.

In case of the trachea, all dose measurements were very low and no constraints were violated. D_{max} and V5 values were significantly lower for the robust plans with p-values below 0.05 and 0.01, respectively. Concerning the volume dose, the median value was 0.0 % for both plans. Due to the upper limit of the whiskers being higher for the robust plans (41.6 % vs. 32.2 %), the unsigned rank test resulted in a statistical significance in favor of the conventional plans.

As already described by Anderle et al. [2018], the smaller airways were the most critical organ for this patient cohort. The differences between the three dose measurements were statistically significant, and p-values were far below 0.001. The robust plans yielded smaller values for D_{max} and V5, since median, average and upper whisker limits were always lower than for the conventional plans. There is no clear trend for the D_{vol} distributions: the median D_{vol} value was smaller for the conventional plans (52.1 % vs. 55.9 %) whereas the average D_{vol} value was larger (57.1 % vs. 50.4 %). The largest difference could be found in the height of the whiskers with the upper limit at only 100.6 % for the robust plans but at 126.9 % for the conventional plans. Given that the OAR constraints were counted as violated if the dose value is above 100 %, and the upper limit of the whiskers was much closer to the 100 %, the robust plans met the dose volume constraint in many more uncertainty scenarios than the conventional plans. For robust optimization, this constraint was fulfilled in 98.8 % of the uncertainty scenarios, whereas, for the conventional plans, it was only fulfilled in 79.8 % of cases. For the maximal dose constraint, the robust plans were below the limit in 62.4 % of uncertainty scenarios, compared to 46.3 % of cases for the conventional plans.

Dose exposure of the lung is shown in figure 3.12. Since in patients 20 and 22 only the left lung lobes were affected by tumors, the healthy right lung lobes were neglected for the evaluation of the lung exposure. In the remaining patients both lung lobes were affected. Thus, the affected lung lobes are further referred to as the 'ipsilateral lung'. For carbon ion therapy, the number of treatment fields is less than those needed for IMRT and the entry channels receive less dose, so the volume dose constraint from Benedict et al. [2010] was always fulfilled for the lung and is therefore not shown. To assess the high and low dose exposure, D_{max}, V90 and V20 were evaluated. As the lung is considered as a parallel tissue, which can tolerate partial radiation induced damage without directly affecting the function of the lung, no maximal dose constraint is stated in Benedict et al. [2010]. In order to allow reasonable evaluation, the maximal dose was normalized to the planned target dose.

For the ipsilateral lung, all three dose measurements were significantly smaller for the robust plans with p-values far below 0.001. The difference was greatest for the maximal doses, where the median value was reduced from 113.8 % to 110.2 % of the target dose. More importantly, there was a reduction to the upper limit of the whiskers from 147.4 % to 122.9 %.

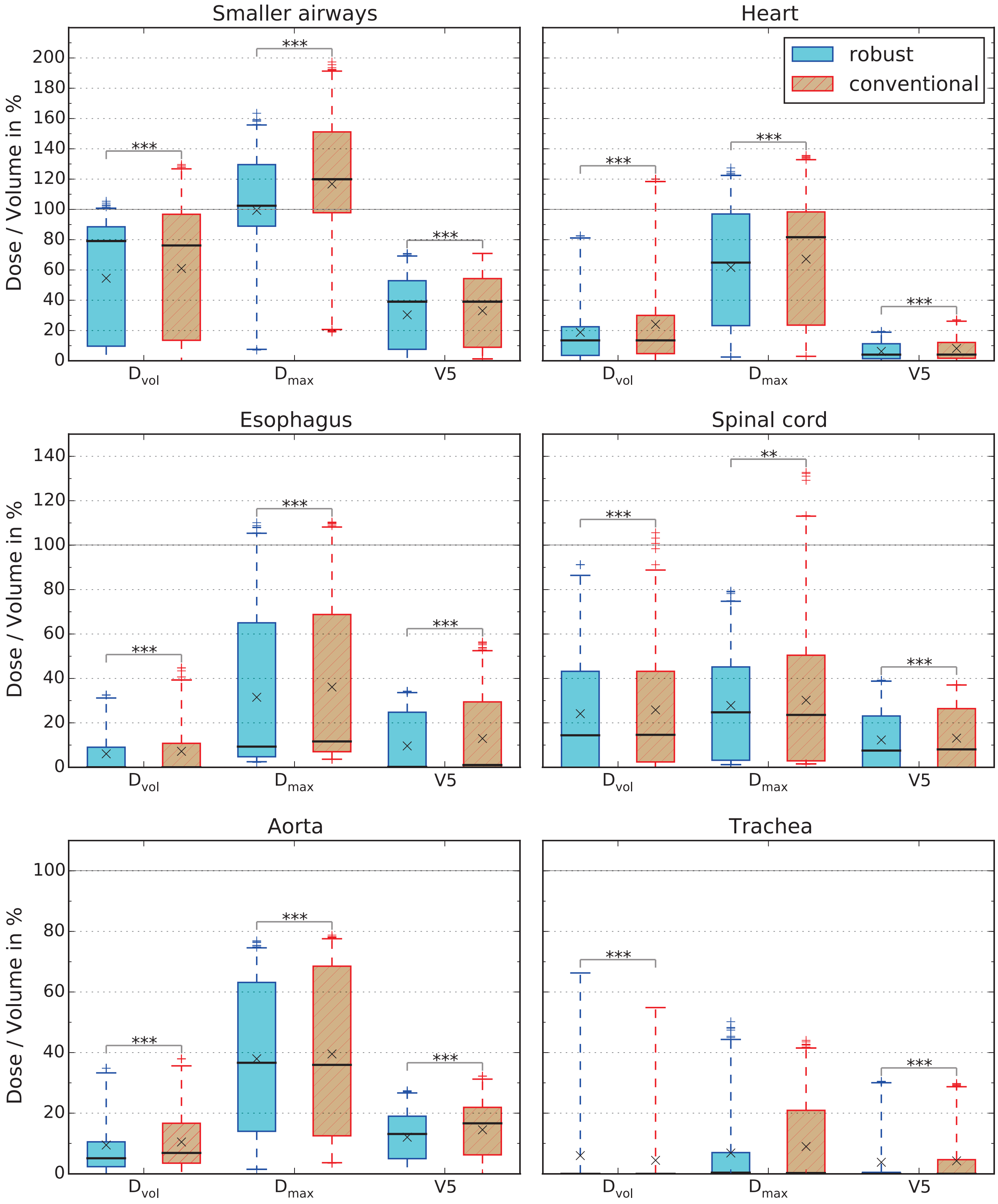

Figure 3.11.: OAR doses summarized for all patients shown as boxplots of D_{vol}, D_{max} and V5. Results are shown for the conventional and the robust plan. The black line indicates the median value whereas the black X denotes the average value. The boxes represent the 1^{st} and 3^{rd} quantiles, while the whiskers represent the environment of 3 standard deviations. P-values of unsigned rank test. Statistical significance is indicated by a p-value calculated with an unsigned rank test ($^{*} \mapsto p < 0.05$, $^{**} \mapsto p < 0.01$, $^{***} \mapsto p < 0.001$).

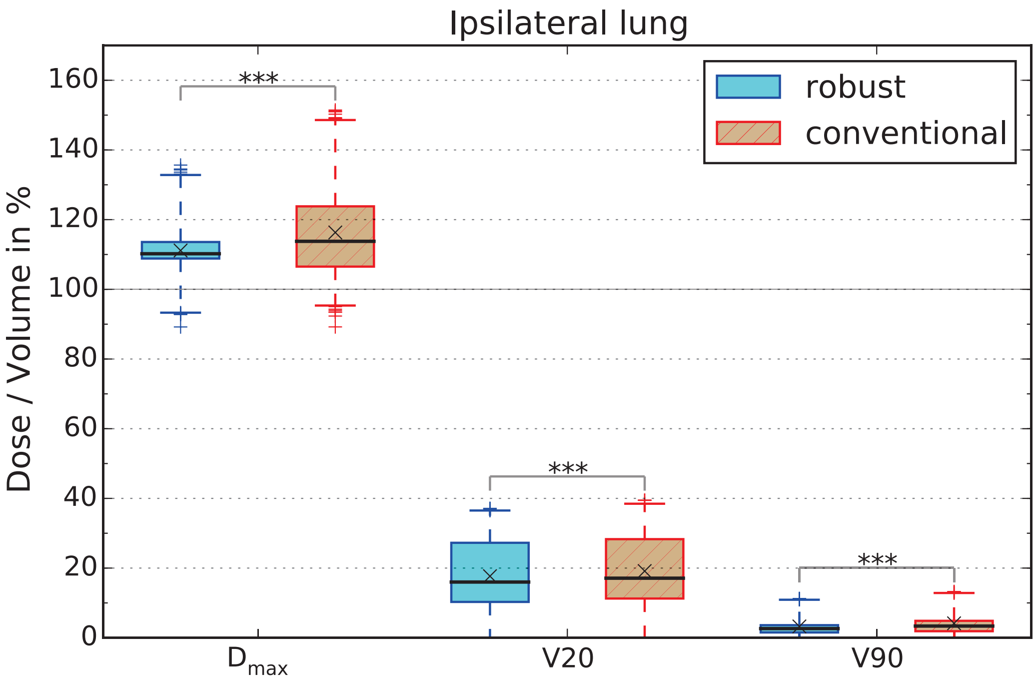

Figure 3.12.: Dose exposure of the ipisilateral lung as boxplots of D_{max}, V20 and V90. Results are shown for the conventional and the robust plan. The black line indicates the median value whereas the black X denotes the average value. The boxes represent the 1^{st} and 3^{rd} quantiles, while the whiskers represent the environment of 3 standard deviations. P-values of unsigned rank test. Statistical significance is indicated by a p-value calculated with an unsigned rank test ($^{*} \mapsto p < 0.05$, $^{**} \mapsto p < 0.01$, $^{***} \mapsto p < 0.001$).

3.9 Discussion — patient study

Robustness

The summarized results for the CTV coverage in figure 3.10 show that the robust optimization leads to a gain in robustness against patient setup errors and range uncertainties. This is described by the considerable reduction to the width of the 3σ-interval for the D50 values and by significantly smaller HI values. So, even if the dose delivery was influenced by shifting the patient's isocenter and/or manipulating CT density, the robust treatment plans provided a more homogeneous dose distribution with a narrower uncertainty band. This confirms the first hypothesis that the robust 4D ITV optimization leads to a general increase in robustness against range changes and patient positioning uncertainties. The same holds true for the robust LOW plans.

Nevertheless, in some cases, the homogeneity of a plan was compromised by the objective of increasing robustness of OAR sparing. This can be seen for the case of patient 23 (see section 3.7). Although there was a considerable drop in target coverage, when focus was set on robust sparing of the smaller airways, the uncertainty bands of the DVH curves of the CTV remained narrow on the dose fall-off around 100 % of the target dose. This can be interpreted in such a way, that even the robustness of an unfavorable dose distributions can be increased. As desired, robust optimization allowed the dose distribution for the smaller airways to become more robust. In contrast to the impact of the robust optimization on the CTV, the increased robustness does not become apparent through a reduction of the uncertainty band. The uncertainty bands of the DVH curves for the smaller airways stayed more or less the same (as seen in figures 3.5 and 3.6). The only visible difference was that the both DVH curves for the smaller airways were shifted to lower dose values, converging towards the dose volume constraint (indicated by stars in the DVH plots) for the robust plans. So, the robust plan allowed meeting this constraints in more uncertainty scenarios than the conventional plan allowed. In the case of patient 23, the dose volume constraint for the smaller airways was fulfilled in 96.4 % of the considered uncertainty scenarios for the robust plan, averaged over the smaller airways in both lung lobes. This is in contrast to the conventional plan, where the same constraint was fulfilled in only 38.1 % of cases.

It is important to note that the current implementation of the worst-case for the robust optimization can increase general robustness for either the target volume *or* critical organs. The objectives of increasing robustness for the target volume *and* the OARs are prohibitively opposing to lead to a optimal solution. In the case of close distances between targets and OARs (smaller than 10 mm to 15 mm), the conventional optimization may more effectively unify the two opposing objectives. This may occur because the conventional optimization takes into account a single nominal scenario only, whereas the robust optimizer currently accounts for nine uncertainty scenarios simultaneously.

The described behavior of the robust optimizer not being able to find solutions which can fulfill opposing objectives is potentially owed to the utilization of the worst-case method and might be avoided with the probabilistic approach proposed by Unkelbach et al. [2007] or the *minimax* approach proposed by Fredriksson et al. [2011]. For the latter approach, cost functions are evaluated for each uncertainty scenarios, minimizing the cost function with the highest value in each iteration step. This ensures that only scenarios are considered which can occur in reality. Such a discrimination is not possible for the voxel-wise worst-case method.

The way how the different motions phases are considered in the implementation of 4D optimization in TRiP4D [Graeff, 2014], as used in the patient study presented in this chapter, could serve as a new implementation of robust optimization. For the conventional 4D optimization, there is typically a set of 10 FDC matrices, one for each motion phase (see section 3.2). However, all FDC matrices are referring to the same beam spot grid, representing different motion scenarios. A similar approach should be feasible for robust optimization by considering the uncertainty scenarios as independent possibilities with equal weights. This approach should be still compatible to 4D optimization, since it would expand the set of FDC matrices per motion state only.

Target coverage

Target coverage must be considered in the context of the dose exposure to the OARs. Since, in figure 3.10, the summarized results for the 24 CTVs for the entire patient cohort are presented, suboptimal results of individual patients are not visible. Patient 23, which was selected to be described in more detail, is a good example of this as there is a significant loss in target coverage for the robust plan as seen in the distributions of the V95, D95 and D99 values in figure 3.8. As for the robust and conventional plans, the sparing of the smaller airways were prioritized, the loss of target coverage is a direct consequence of the superior sparing of the smaller airways provided by the robust treatment plan (see figure 3.9).

Although, there was no significant difference in the distribution of the V95 values, the robust optimization is preferable, as the interval width of the whiskers was narrower for the robust plans than for the conventional plans. Disregarding outliers, the absolute difference in the lower limits of the whiskers was more than 30.0 %, favoring the robustly optimized plans (see figure 3.8). For the D95 values, the discernible difference between robust and conventional plans was less distinct, but slightly higher average and median dose values than for the robust plans, and the absence of a statistically significant difference, favor the conventional plans.

The statistical significance of the D99 values was more evident in the boxplots. Apart from the identical median D99 values, the average values were higher for the conventional plans. In combination with both the lower and the upper whisker limits being higher than for the robust plans, the conventional plans were favorable. However, accomplishing the objective of D99 ≥ 100.0 % posed a challenge to both optimization approaches, especially when aiming to fulfill this objective in large number of uncertainty scenarios. Though the focus of the robust treatment planning was set on sparing adjacent OARs, the percentage of scenarios which fulfilled the CTV objective was still comparable to the results of the conventional plans (31.9 % and 38.5 % for robust and conventional plans, respectively).

Despite the low dose areas of the robust plans, the remaining portions of the dose distributions are more convex than for the conventional plans, resulting in less hot and cold spots. This can be explained by the reduced internal dose gradients, which reduces the susceptibility to interplay patterns for the robust dose distributions. In the most extreme case, patient 23 presents strongly enhanced interplay patterns, which result from increased CT densities. This is illustrated in the transversal dose cuts of patient 23 for nominal and HD scenarios in figure 3.4.

OAR exposure

When comparing the robust and conventional 4D ITV optimizations, it is clear that critical organs do, in general, profit from the robust approach, as they receive less dose. The differences in OAR dose exposure between the robust and the conventional plans were not as pronounced as between SBRT and carbon ion therapy, as described in Anderle et al. [2016, 2018]. In fact, for most critical structures, the differences between the results of the conventional and robust plans were marginal but the dose exposure is reduced for the robust plans in most cases. Although, there are patients where the OAR doses were higher for the robust plan than the conventional plan, the volume and maximal doses were still within the limits stated by Benedict et al. [2010]. Hence, the robust plan should be still selected, if the objective is to improve target coverage.

For the robust optimization, the exact same number of treatment fields with the same beam angles and similar voxel weights as in the conventional optimization were used, so the improvement to OAR sparing was quite small. During treatment planning, the largest difference between both optimization types, was the choice of increases planned target doses for the robust optimization, as stated in table 3.1. This step was necessary to reach acceptable D99 values, since the shape of the dose fall-off region of the robust DVH curve was narrow in width but less steep than the conventional DVH curves.

Using the objective optimization, introduced into TRiP4D by Anderle et al. [2018], was only necessary the robust optimization of patient 23. This is a remarkable result, since conventional planing required the use of objective optimization in 4 of the 8 patients in order to create treatment plans with sufficient OAR sparing (see [Anderle et al., 2018]). The remaining patients were optimized with only the basic robust 4D optimization algorithm and still yielded a small improvement in OAR exposure. Less computational effort was needed to meet the required OAR constraints, and the robust optimizer generally performed well in sparing critical structures.

The enhanced performance was especially true for OARs which are further from the CTVs (distances larger than 10 mm to 15 mm). The OARs were also spared with robust optimization, although they were not explicitly considered in the optimization. This behavior may result from the more convex and compact dose distributions to the target which avoid unnecessary margins. This effect was especially prominent for the heart, though it has been only considered in optimization for 2 of 8 patients; for all patients slight improvements to the volume doses, and significant reductions to the median maximal doses were seen. As reported by Gagliardi et al. [2010], reduced heart doses are beneficial as they reduce the relative risk for radiation induced heart diseases, such as pericarditis. Also in Benedict et al. [2010], the recommended limit values for the dose volume constraint and the maximal delivered dose to the heart for single fraction treatments are considerably lower then for 3 or 5 fractions (see table B.1), which further emphasizes the importance of reduced heart doses for high dose single fraction treatments as investigated in this thesis.

For critical structures in close vicinity to the target, such as the smaller airways, robust optimization can also provide beneficial results. The smaller airways can be particularly close to lung tumor lesions, as they are found as smaller bronchial ramifications in the lung. As mentioned, the robust plan optimization was generally conducted with the same voxel weights as used for the conventional plan optimization by Anderle et al. When during robust optimization the OAR voxel weights were larger than the CTV voxel weights, this led to low dose areas between the target and the critical organ. As described in section 3.7, this was an intrinsic consequence of the current implementation of the robust optimization in TRiP4D. Although the dose exposure of the smaller airways is significantly reduced, the superior OAR sparing causes a reduction to the target coverage. By changing the weights to be larger for CTV voxels than for the OAR voxels, dose distributions like those of the robust LOW plan for patient 23 would be created. These reversed voxel weights create a significantly more robust target coverage but also significantly increase the OAR dose exposure.

As discussed for patient 23, the strict assignment of voxels as OAR *or* target voxel strongly contributed to the decrease of target coverage, especially when target volumes overlapped with critical organs in the planning image set and the OAR voxel weights were chosen to be larger as the CTV voxel weights. Without changing the implementation of the optimization algorithm, it would be challenging to create a plan which does not sacrifice as much target dose but is still robust against uncertainty scenarios. Compared to robust optimization, the conventional optimization considers a single scenario only. Hence, the RST grid is not laterally and longitudinally shifted as for robust optimization, and tumor and OAR overlaps consequently produce only small low dose areas. The conventionally optimized plan can be considered as an intermediate plan, between the robust and the robust LOW plan. For more complex cases, such as patient 23, However, for patient 23, the conventional planning has a lack in plan robustness and robust planning should be considered to create acceptable plans.

A notable result of the robust plannin was that, although the plan robustness was increased, the maximal dose exposure to the lung was significantly reduced for all patients. The initial expectation was that a gain in robustness to target coverage would create higher doses to the lungs, since features present in the robust optimization, such as accounting for range uncertainties, could increase the created margins. The reduced maximal lung dose shows, that the manner in which robust optimization increases plan robustness is not only done by creating patient and field specific margins. In addition, the robust plan avoids large internal dose gradients which could lead to hot and cold spots under presence of position or range uncertainties. In summary, plan optimization on set of several uncertainty scenarios simultaneously creates an averaged mixture of all possible plans for each corresponding uncertainty scenario.

General remarks on treatment planning

While, for the conventional optimization, it was not necessary to explicitly account for normal lung tissue during the optimization, the case can be different for the robust optimization. Since the RST grid is effectively shifted laterally and longitudinally within the patient geometry by accounting for patient setup errors and range uncertainties, and the difference in density between the solid tumor and the lung tissue is high, this can lead to unrestricted dose exposure to the lung. This effect was seen in patient 20. A straightforward approach to reduce normal lung dose exposures was to add the lung as a critical organ to the optimization. It was sufficient to simply add a shell of lung tissue around the tumor to the optimization with a thickness of about 10 mm. The OAR voxel weights were chosen to be smaller than the CTV voxel weights, in order to avoid a cropping of the CTV volume due to the strict assignment of voxels as OAR or target. Further, it was sufficient only to consider every 80th voxel of the considered 'lung shell'. With this approach, the normal lung dose exposure could be reduced to acceptable levels.

The results of this patient study have shown that a robustness analysis is a very powerful tool. Although, a 'robustness' analysis with respect to patient motion was performed by Anderle et al., by evaluating the 4D dose distributions of the conventional plans for 4 respiratory curves, the RA presented here which analyzed patient setup errors and range changes, revealed considerable lacks in plan robustness for the conventional optimization. For example, interplay was visibly higher in patient 23 for the left CTV when the CT density was increased by 3.5 %.

3.10 Conclusion

The main goal of introducing robust optimization methods into TRiP4D was to improve OAR sparing while maintaining sufficient target coverage. With the help of the robustness analysis (RA), the impact of various uncertainty scenarios on target coverage and OAR sparing for both robustly and conventionally 4D optimized plans was investigated. For the RA, 84 uncertainty scenarios have been taken into consideration, accounting for patient setup uncertainties, range changes and various respiratory motion patterns.

For the patient cohort presented in this chapter, the smaller airways stood out has the most critical OAR. As described by Anderle [2016], the smaller airways are limiting factor for the treatment planning for photon 3D SBRT plans. During the treatment planning at Champalimaud Center for the Unknown, in Portugal, the OAR constraints presented in Benedict et al. [2010] were used strictly. For the treatment plans using scanned carbon ions, it was possible to significantly reduce the dose exposure of the smaller airways using robust 4D ITV optimization, and the overall CTV coverage was still comparable to 4D ITV treatment plans, as seen in Anderle et al. [2018].

For the target coverage, a general improvement to the robustness due to the robust 4D optimization was most visible through the reduced width of the D50 distributions, which represent a small uncertainty band in the DVH curves for the targets (see figure 3.10). Moreover, the significantly lower HI values depicted an additional increase to robustness compared to the conventional optimization, describing a convergence of the target DVH curves to the ideal step-shape.

When target or OAR objectives are considered on their own, the plans created with the robust 4D ITV approach confirmed the first hypothesis stated in section 3.1. However, in some cases it was not possible for the robust optimizer to find robust solutions for both target and OAR objectives at the same time. This tended to occur when the two objectives opposed each other too much for an optimal plan result, as, in case of patient 23, caused by an partial overlap between the smaller airways and the tumor volume. A possible solution to this case would be a revision to the optimization algorithm, to allow for voxels to be assigned as both target and OAR voxels simultaneously. Such a possibility is not currently present in TRiP4D.

The second hypothesis was only conditionally confirmed, as the results in figures 3.11 and 3.12 showed indeed less dose delivered to the majority of the considered critical structures for the robust plans, but to achieve the superior OAR sparing, the target dose needed to be compromised. This was especially true for OARs close to the target. Although, a patient could benefit from single fraction treatments due to the higher biological effective dose (BED), there is a great deal of uncertainty to whether so much target coverage could be sacrificed. When the smaller airways dose exposure was dramatically decreased and the tumor could not be controlled, the benefit to the patient is marginal at least.

Nonetheless, as the robustness analysis has shown, conventional plans can be highly affected from not being robust. This was seen in patient 23, where the conventional plan looked reasonable in the nominal scenario, but the results from a RA revealed that target coverage had actually been impeded and the dose volume limit of the smaller airways was violated for a majority of uncertainty scenarios. Like the robust approach, the 4D ITV method with conventional IMPT had its advantages and disadvantages. Yet, for the robust 4D ITV optimization, as stated in the hypothesis, the nominal dose distribution might be compromised, it does not degrade as much as the conventional plan in cases where setup or range uncertainties exist. Additionally, the inherent possibility of OAR avoidance of carbon ions over photon can still be exploited. But for particular patients this could require sacrificing some target coverage. In the clinical setting, the requirements of the physician would need further deciding whether the robust optimization approach would be beneficial to the patient treatment.

In contrast to the Champalimaud Center for the Unknown, lung cancer patients at the university hospital in Marburg, Germany, are treated with stereo-tactic photon therapy without even considering the smaller airways during treatment planning [Personal correspondence with Dr. Stefan Lautenschläger]. The different approaches of how and whether critical organs are take into consideration for plan optimization, exemplify discrepancies in the best practices for treatment planning at radiation oncology centers.

If the smaller airways could truly be ignored as critical structures during optimization, there is even more reason to use a treatment planning strategy such as the robust LOW optimization for patients, such as patient 23, as this method significantly improves robustness of the target coverage in the majority of considered uncertainty scenarios.

4 Robust conformal 4D optimization

Contents

4.1 Introduction

In this chapter, a robust version of conformal 4D optimization strategy is presented for a selected patient. The approach is an extension of the 4D rescanning method described by Graeff [2014]. The basic idea is to avoid the increased ITV-like volume which is necessary to cover the target in all motion states for both the robust and the conventional version of the 4D ITV optimization presented in chapter 3. This can be accomplished by creating a library of plans which consists of a conformal plan for each motion phase of a 4DCT. This library of plans is further on called 4D RST.

For each motion phase, a conformal plan is optimized, which delivers the complete target dose . Using a 4DCT with 10 motion states during treatment planning results in 10 corresponding *phase* treatment plans. The irradiation of this 4D RST on a patient would result in a dose distribution 10 times higher than the prescribed dose. In order to deliver the prescribed dose only, the particle numbers of the phase plans need to be downscaled. The scaling factor is determined by the number of motion states of the used 4DCT, which would result in a scaling factor of 1/10 for the given example. This downscaled 4D RST creates a conformal dose distribution to the target volume, also when target motion is present. As each of the unscaled phase plans would deliver the complete prescribed dose to the target, conformal 4D optimization is fully compatible with biological dose optimization and the concept of RBE, as the accumulated particle spectra of all downscaled phase plans is similar to the particle spectra generated by one of the unscaled phase plans.

Compared to the 4D ITV method presented in chapter 3, the conformal 4D optimization has the disadvantage, that the delivery of a 4D RST requires synchronization of the irradiation with the patient motion. Figure 4.1 schematically illustrates a 4D RST for a single IES, depicting how specific RST slices from the 4D RST are assigned to the IES of the corresponding motion state.

In Graeff [2014], a combination of 4D rescanning with multiple SFUD fields is proposed in order to increase robustness by avoiding inter-field dose gradients. The range ITV, as described by Graeff et al.

4D RST for 10 phases, single IES

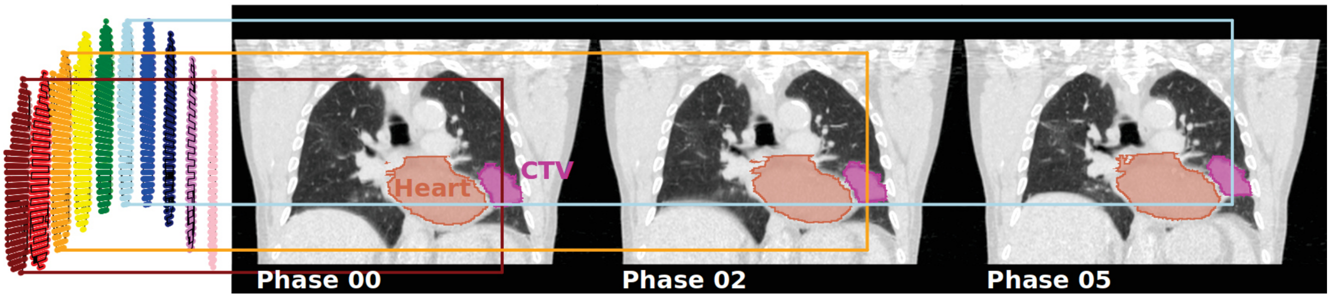

Figure 4.1.: Illustration of a 4D RST for a single IES. For the considered IES, a corresponding RST slice exists for each motion phase. Here, only 3 out of 10 CT phases are shown. During treatment, the delivery is synchronized to the respiratory motion of the patient, which requires a dedicated TCS with a fast real-time motion monitoring. Courtesy for 4D RST illustration: A. Eichhorn.

[2012], is used prior to the optimization in order to estimate the required size of the *base RST* which serves as the starting point for further setup of the phase plans (a more detailed description of the base RST is given in section 4.2). During the optimization of the phase plans, the target is set to the CTV of the corresponding motion state plus additional isotropic safety margins. The described approach is capable of accounting for range changes caused by patient motion. Within this approach, it is possible to accomplish rudimentary OAR sparing by using a super-position of two or more SFUD fields, which, however, requires further down scaling of the particle numbers in each phase plan. The scaling factor is given by multiplying the number of treatment fields by the number of motion phases. For example, using 3 SFUD fields on the same target with 10 motions states results in a scaling factor of 1/30.

The drawbacks of this method are, that the use of intensity modulated particle therapy (IMPT) is prevented and the inclusion of additional field specific range margins is not possible. Here, the robust optimization could provide new opportunities, as it enables the consideration of additional range changes while keeping the target volumes constant which is required for a multiple field IMPT optimization [Lomax, 1999]. Thus, robust IMPT within 4D rescanning should be able to account for field-specific range uncertainties beyond those depicted in the 4DCT. Further details on the implementation of the robust 4D rescanning approach are described in the following section.

For the treatment delivery of a 4D RST, a dedicated TCS which is capable of handling a plan library, and a fast real-time motion monitoring system are required. So far, this system exists as a prototype at GSI only and has been validated in 2D film experiments [Graeff, 2014].

4.2 Optimization method

For the 4D rescanning method each phase plan is optimized separately and independently of the remaining phase plans. However, due to the design of GSI's TCS and the implementation of the 4D dose calculation, the initial dimension of each phase RST grid has to be the same for all motion phases in order to create a valid 4D RST. To provide an RST which is large enough and which contains the target structure in all motion states, an empty *base RST*, containing zero particle numbers for each spot, is created, which serves as the starting point for the further setup of the phase plans. This is done by creating a range ITV of the target volume, extended by isotropic PTV margins. The resulting range ITV is used to set up the initial base RST. This procedure ensures that the dimensions of the base RST are large enough to contain the target volume in all motion phases.

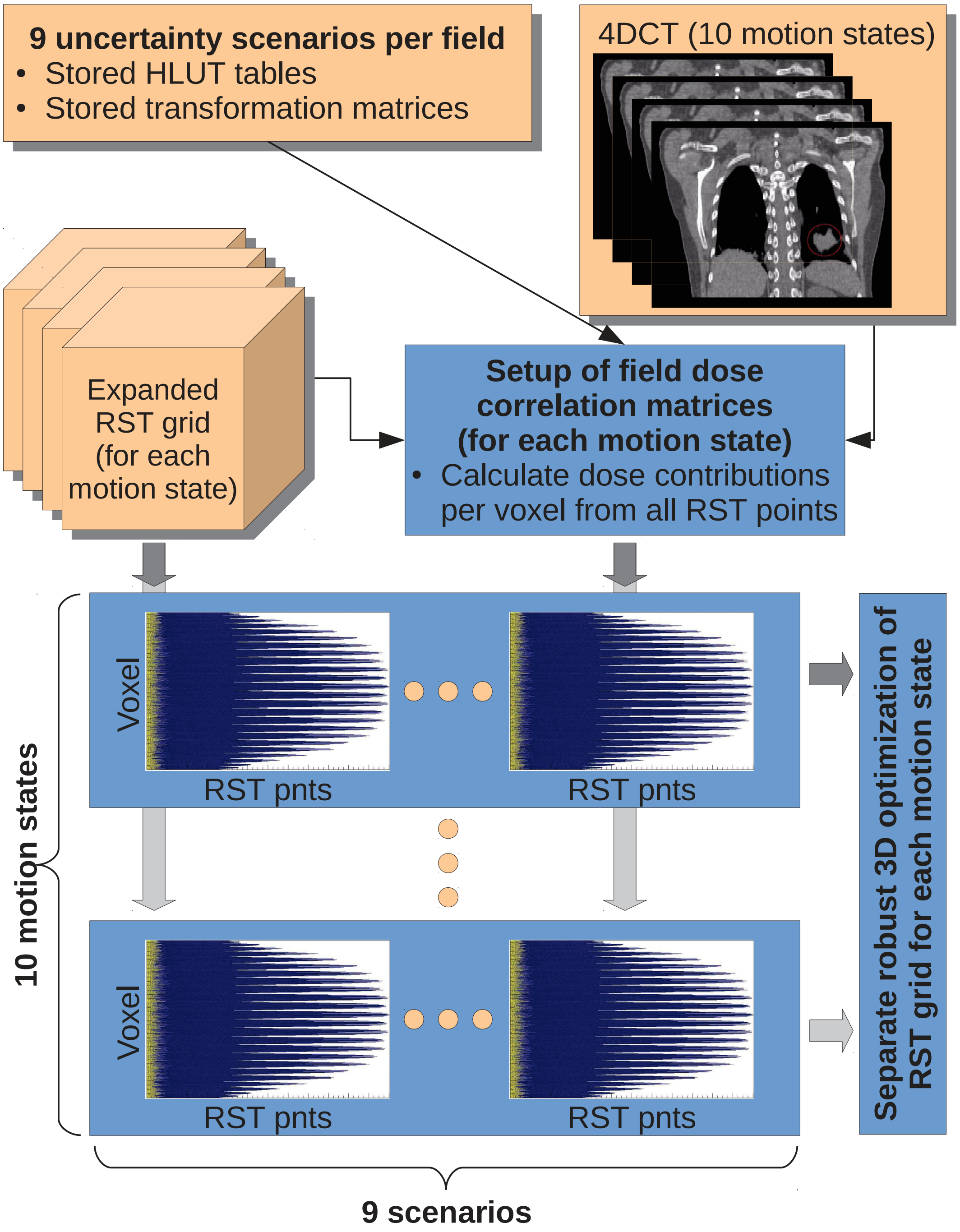

Figure 4.2.: The flowchart schematically shows the setup of the field dose correlations (FDC) matrices for the robust conformal 4D optimization. For each of the 10 motion states of a 4DCT, the FDCs for each pencil beam are calculated and stored, based on 9 uncertainty scenarios (as shown in fig. 2.5) and the expanded base RST. This approach results in 10 separate robust optimization problems, each consisting of 9 FDC matrices from which different dose scenarios can be calculated.

The schematic procedure of the optimization is shown in figure 4.2. The robust treatment fields are set up as described in chapter 2 (see figure 2.5). The 9 uncertainty scenarios, including the stored HLUT tables and transformation matrices (WEPL space ⟷ patient CT), are used for the setup of the

FDC matrices. In contrast to the 4D ITV approach, as described in chapter 3, each of the phase raster grids (RSTs) corresponds to one motion state of the 4DCT only. As mentioned, this typically leads to 10 independent optimization problems, which each consist of 9 corresponding FDC matrices, in case of robust optimization on 9 uncertainty scenarios. The final plan library is created by applying the scaling factor, which was introduced in the introduction of this chapter.

It is to be noted, that the 4D rescanning method requires the minimum particle number to be increased in order to generate valid phase treatment plans. As described in section 1.6.3, at GSI, the default value for the minimum particle number N_{min} is set to 5000. To maintain plan validity after downscaling of the optimized particle numbers, N_{min} needs to be increased to 50 000 during optimization. For low target doses, in the order of some Gy, a minimal particle number of 50 000 can lead to suboptimal optimization results, as the lowest possible dose value generated by a single beam spot is increased; however, for single fraction doses beyond 20 Gy(RBE) this effect becomes negligible.

4.3 Treatment planning

For treatment planning with the conformal 4D optimization, the same parameters as for the 4D ITV optimization were used, including target weights, OAR weights, and target doses as stated in table 3.1. For the conventional optimization, 3 mm PTV margins were used as described in chapter 3. For the robust optimization, the robust parameters were set to ±3 mm for setup uncertainty and to ±3.5 % for range uncertainty. As described above, plan optimization of the 10 phase RSTs was performed separately. The separate optimization of these phase plans also enables the handling of large CTVs by allowing to increase the number of target voxels considered in the optimization of each phase plan. Compared with 4D ITV optimization, a similar increase in considered target voxels would exceed the working memory.

This was the case for patient 3, whose left lung lobe was afflicted with two tumors with volumes of $123\,\mathrm{cm}^3$ and $136\,\mathrm{cm}^3$). As described in chapter 3, including voxels from all 10 motion phases during 4D ITV optimization for patient 3, exceeded the allowed working memory and led to abortion of the calculation. Only by reducing the number of considered motion states from 10 to 3, allowed for regular execution of the 4D ITV optimization. In addition to the reduction of considered motion states, random voxel subsampling was necessary for both the conventional and robust 4D ITV optimization. Especially for the robust 4D ITV optimization, omitting the random voxel subsampling exceeded the assigned working memory which led to an abortion of the optimization algorithm. In order to maintain comparability with the results from chapter 3, random voxel subsampling was also used for conventional and robust 4D rescanning.

As presented in the study in chapter 3, plans for the left and right lung lobes were optimized separately, since the treatment fields, assigned to each lung lobe, overlapped only marginally.

4.4 4D dose calculation

In the ideal case of 4D rescanning, each motion phase is irradiated with a conformal dose distribution provided by the corresponding phase plan. Thus, acting on the assumption of having perfect synchronization between treatment delivery and respiratory motion, no further correlation between organ motion and the scanned beam is considered. The contributions of all pencil beams from all motion states are transformed to the reference state of the 4DCT, on which the RBE-weighted LEM-based dose is calculated from the accumulated particle spectra.

As in chapter 3, plan quality of the dose distributions was assessed with a RA which considered 21 different uncertainty scenarios, which resulted in a total of 21 different dose distributions. Dose measures, such as V95, D95, D99, D5, and HI were used to asses target coverage, and D_{max}, D_{vol}, and V5 were used to determine dose exposure to critical structures. The statistical significance between different treatment plans was calculated by performing an unsigned paired rank test. The resulting p-values are divided into three different classes: $^{*} \mapsto p < 0.05$, $^{**} \mapsto p < 0.01$, $^{***} \mapsto p < 0.001$.

4.5 Results

Patient 3 was selected for the 4D rescanning method, as this patient showed the highest motion amplitude of up to 17 mm, in combination with large tumor volumes in the left lung lobe (123 cm^3 and 136 cm^3) (see table 3.1). Hence, patient 3 was a promising candidate to benefit from the conformal treatment delivery provided by the 4D rescanning approach, as less normal tissue would be harmed.

Dose distributions

To illustrate the differences between robust 4D rescanning and robust 4D ITV optimization, axial and coronal dose distributions of the nominal dose scenario are presented in figure 4.3, for the left lung lobe of patient 3. In general, the margins generated by the robust 4D rescanning plan were smaller as those generated by the robust 4D ITV plan. The reduced margins due to the more conformal irradiation by robust 4D rescanning, were most pronounced in CTV1. This can be seen in the coronal view of patient 3 in figure 4.3(a) and (c), where especially the margins on the superior and (patient) left portion of the target volume are visibly smaller (indicated by red arrows).

The conformal irradiation with the robust 4D rescanning plan also enabled superior target coverage of the medial area between CTV1 and the heart. Although CTV1 was in close proximity to the heart, which was considered as critical organ during the optimization, the robust 4D rescanning approach was able to generate at least small safety margins. For the robust 4D ITV plan, a similar low dose area, as described for patient 23 in chapter 3, was visible between the heart and CTV1. Since there was no overlap between heart and CTV1, this low dose area did not impede the target coverage as much as for patient 23; however, not much safety margin was left to handle potential patient setup or range errors. The reduced heart dose due to the robust 4D rescanning plan can also be seen in figure 4.6, where the DVHs for the left lung lobe of patient 3 are depicted for robust 4D ITV plan and the robust 4D rescanning plan.

figure 4.4 shows the deteriorated dose distributions for the robust and the conventional 4D rescanning plans, caused by the presence of setup and range uncertainties. The depicted uncertainty scenario is a superposition of increased CT density, which causes range undershoots, and a setup error, which shifts the patient's isocenter in direction of the heart. Comparison between the resulting dose distributions of both plans showed cold spots in the dose distribution of the conventional 4D rescanning plan, whereas the dose distribution of the robust 4D rescanning plan still provided sufficient target coverage.

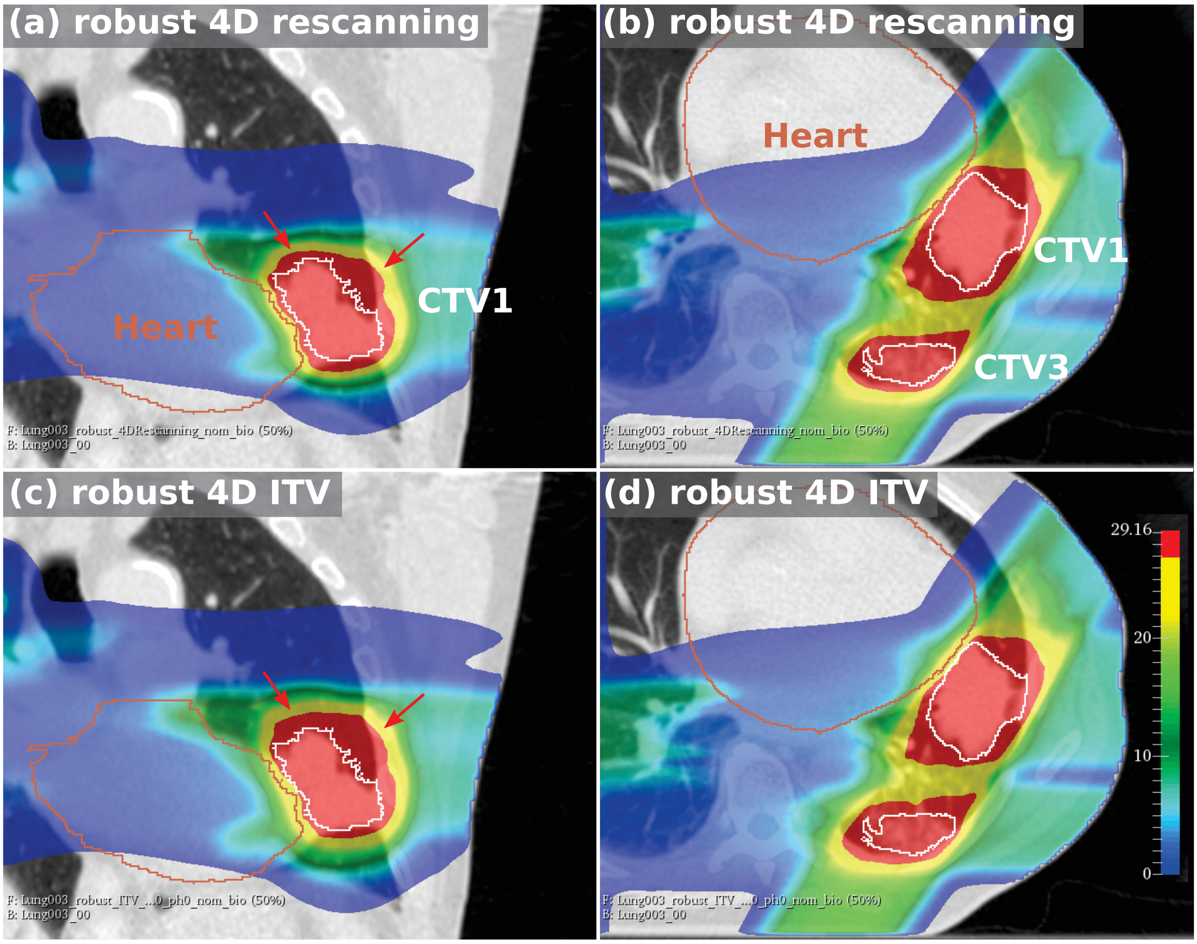

Figure 4.3.: Dose distribution of the nominal dose scenario for patient 3, showing (a) the axial view and (b) the coronal view of the robust 4D rescanning plan, whereas (c) shows the axial view and (d) the coronal view of the robust 4D ITV plan.

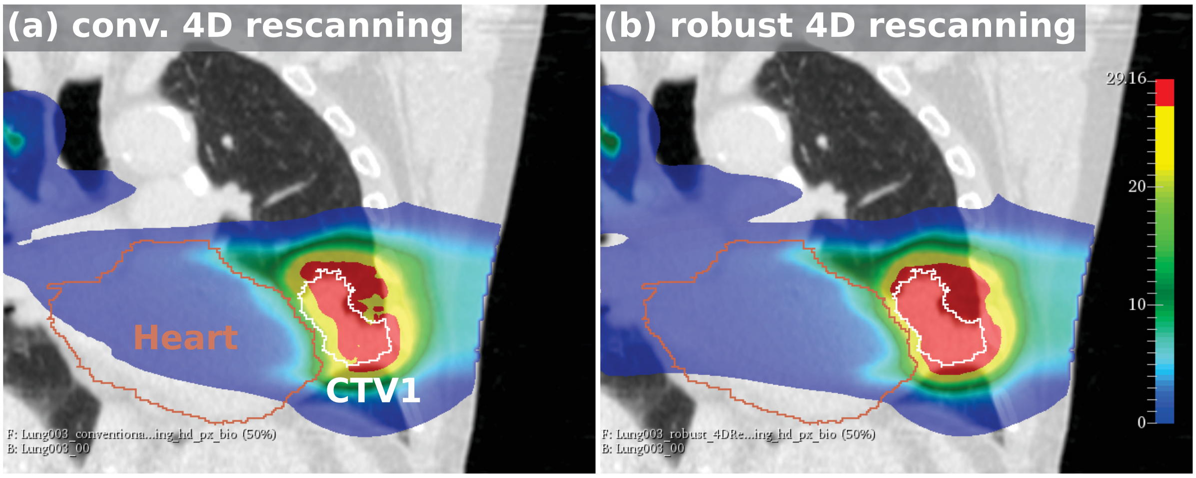

Figure 4.4.: Coronal dose distribution of patient 3, exemplarily showing the deteriorated dose distribution of the conventional 4D rescanning plan (a), compared to the robust 4D rescanning plan (b), in the presence of range undershoot (increased CT density) and a horizontal setup shift in direction of the heart. The conventional 4D rescanning plan produces cold spots and fails to cover the complete target with dose.

As these dose cuts depict examples of the generated dose distributions only, the DVHs shown in the next section give a more comprehensive picture of how dose coverage and OAR exposure are affected by range and setup uncertainties.

DVHs

The DVHs for the conventional 4D rescanning plan for patient 3 are shown in figure 4.5, for the left and the right lung lobe separately. For the conventional 4D rescanning approach, IMPT with 3 mm PTV margins was used. The RA on 21 uncertainty scenarios revealed a huge uncertainty in target coverage. For the left lung lobe of patient 3, conventional 4D rescanning generated excessive overdose, especially for CTV3, while in the right lung lobe, underdosage of the target was the major issue, in particular for CTV2. For the right lung lobe, a dose volume constraint of $D_{0.5cc} < 12.4\,\mathrm{Gy(RBE)}$ was used for the smaller airways. As described in chapter 3, the D_{vol} was normalized to the above stated limit and the constraint was counted as violated, when the 100 % mark was exceeded. For conventional 4D rescanning, the constraint is fulfilled in 90.5 % of the uncertainty scenarios, with $D_{0.5cc} = (77.0 \pm 12.0)\,\%$.

To assess the size of the uncertainty bands, the D50 spread is stated for all 5 CTVs of patient 3 in table 4.1. When compared to robust 4D rescanning plan, the average D50 spread is larger for the conventional 4D rescanning plan by a factor of about 14 . The table also shows the D50 values for the conventional and the robust 4D ITV plan. In comparison to robust 4D rescanning, the increase in average dose spread is less than a factor 2. Compared to the conventional 4D rescanning plan, the D50 spread of the conventional 4D ITV plan is 1/3 smaller, but is still considerably larger than for the two robust plans.

Target	D50 spread in [%]			
	conventional		robust	
	4D rescanning	4D ITV	4D rescanning	4D ITV
CTV 1	10.90	6.33	0.64	1.20
CTV 3	8.01	6.52	0.70	1.14
CTV 2	7.28	4.60	0.73	0.96
CTV 4	7.75	5.15	0.46	1.09
CTV 5	8.88	4.81	0.55	1.03
$CTV_{avg \pm std}$	8.6 ± 1.4	5.5 ± 0.9	0.6 ± 0.1	1.1 ± 0.1

Table 4.1.: Width of D50 dose spread for all 5 targets of patient 3, stating results for 4 different 4D optimization approaches.

The DVHs of the robust 4D ITV plan for patient 3 are shown in figure 4.6(a) for the left lung lobe and in figure 4.7(a) for the right lung lobe. Figures 4.6(b) and 4.7(b) show the DVHs of the robust 4D rescanning plan for the left and right lung lobe of patient 3. When compared to the robust 4D ITV plan, the robust 4D rescanning plan reduced target overdose, as steeper dose fall-offs were generated. The reduction of target overdose due to robust 4D rescanning was more pronounced for the right lung lobe, whereas the width of the uncertainty band around 100 % of the target dose was on a similar level. For the left lung lobe, the dose distributions generated from the robust 4D rescanning plan improved the avoidance of target underdosage, as can be seen in the tighter curvature of the uncertainty band in figure 4.6(b).

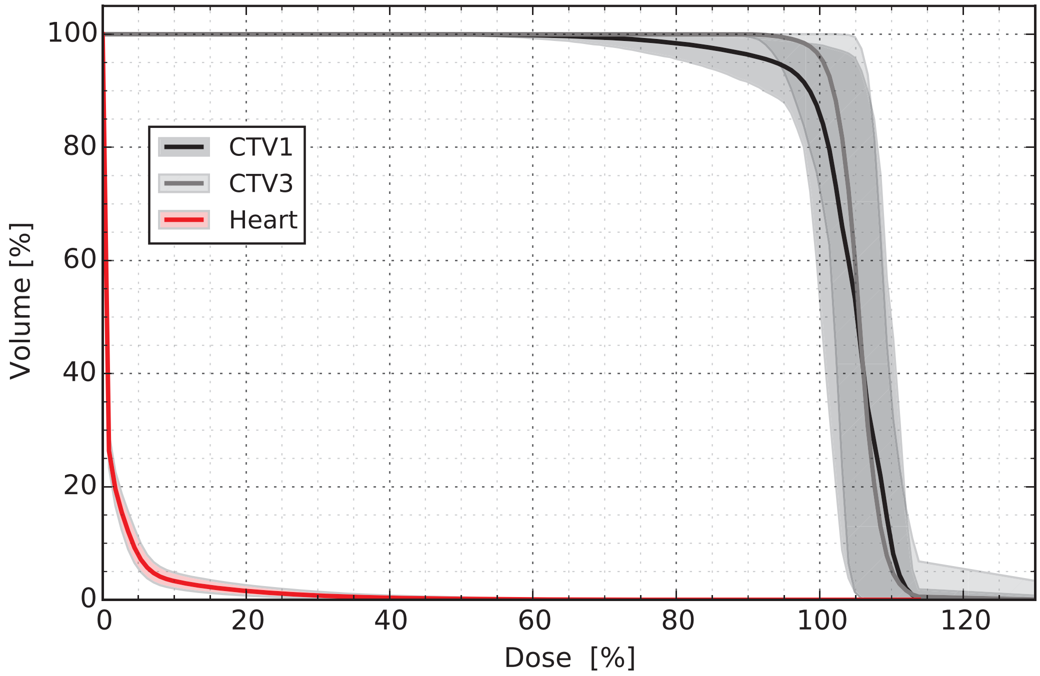

(a) Left lung lobe.

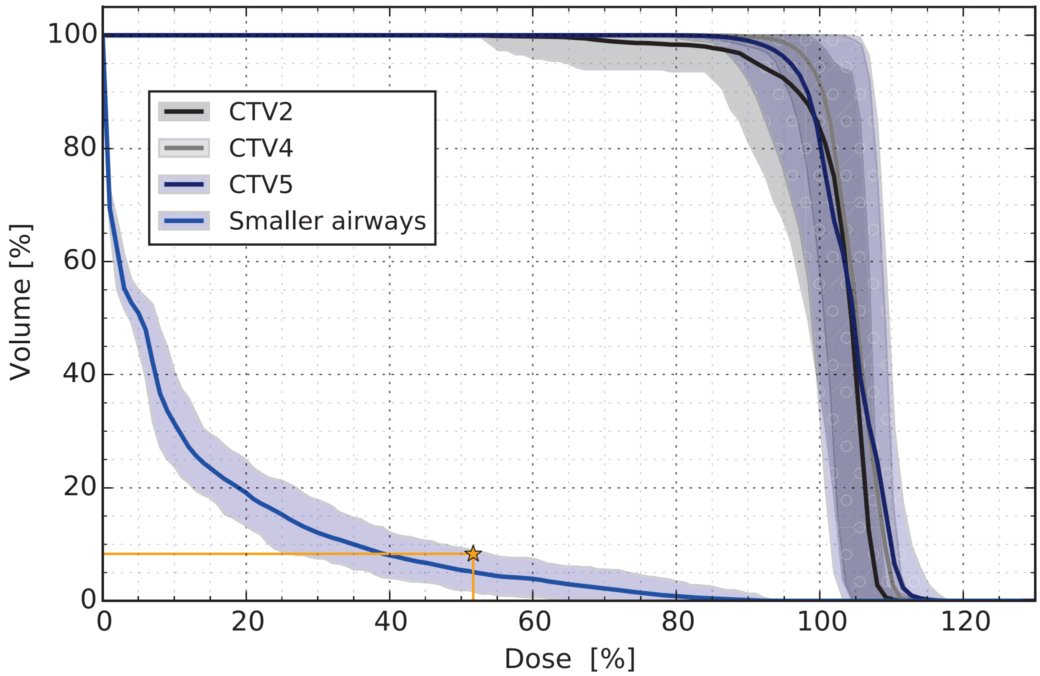

(b) Right lung lobe. Star symbol denotes the dose volume constraint for the smaller airways ($D_{0.5cc} \leq 12.4\,\mathrm{GyE}$), which is fulfilled in 90.5 % of uncertainty scenarios.

Figure 4.5.: DVHs with uncertainty bands resulting from robustness analysis for patient 3, using conformal 4D rescanning with conventional IMPT with 3 mm PTV margins. The solid lines are average DVH curves and the light colored areas are uncertainty bands, depicting the envelope of all 21 4D dose distributions. All target DVHs are normalized to respective target doses and OAR DVHs are normalized to the corresponding limit value of the DVH constraints from Benedict et al. [2010].

Comparing the dose exposure to the smaller airways in the right lung lobe, robust 4D rescanning could further reduce the volume dose from (84.9 ± 6.5) % to (76.3 ± 7.5) % of the corresponding limit, which led to a fulfillment of the OAR constraint in 98.8 % and 100.0 % of the scenarios, respectively. Although both robust optimization methods fulfilled the volume dose constraint for the smaller airways in the majority of uncertainty scenarios, only the robust 4D rescanning plan allowed for an additional improvement to the dose exposure by shifting the DVH curves to lower dose values (for values below about 30 % of the target dose).

CTV coverage

Figure 4.8 shows the summarized CTV coverage for patient 3 as boxplots for the 4 aforementioned optimization approaches. The same dose measurements as in chapter 3 were evaluated, namely V95, D95, D99, D50 and the homogeneity index (HI). In the boxplots, the black lines indicate the median values, and the black X's symbols denote the average values. The boxes describe the 1st and 3rd quantiles, and the whiskers represent 3 standard deviations, including approximately 1 % to 99 % of all values in the distribution of a dose measurement. Outliers are represented by crosses. Since the distribution of these values is not Gaussian, statistical significance has been calculated by using an unsigned rank test. The resulting p-values are divided into three different classes: $^{*} \mapsto p < 0.05$, $^{**} \mapsto p < 0.01$, $^{***} \mapsto p < 0.001$.

As already shown in the DVH plots, for the conventional 4D rescanning plan, the RA revealed a significantly reduced dose coverage. In comparison to the two robust plans and the conventional 4D ITV plan, especially the median values for V95, D95 and D95 were considerably lower for the conventional 4D rescanning. The conventional 4D rescanning plan also showed significantly longer bottom whiskers.

Considering V95, the two 4D ITV plans and the robust 4D rescanning plan yielded similar results. For the D95 values, the robust 4D rescanning plan was significantly better than all other plans. For the D99 values, the robust 4D rescanning yielded significantly better results compared to the conventional 4D rescanning plan and robust 4D ITV plan. Compared to the conventional 4D ITV, the distribution of D99 values was at least on a similar level. Although, the bottom whisker limit was slightly lower at 90.5 %, compared to the robust and conventional 4D ITV plans, with 92.6 % and 93.6 %, respectively.

Compared to the conventional 4D rescanning plan, the two robust approaches showed narrower distributions of the D50 values and smaller HI values, which illustrates the efficacy of robust optimization against dose deterioration due to potential error scenarios. Smaller uncertainty bands and improved homogeneity are also visible in the DVH plots of both robust plans in figures 4.6 and 4.7, compared to the DVH of the conventional 4D rescanning plan in figure 4.5. While for both robust plans, the whiskers were close to the D50 median value, the width of D50 distribution for conventional 4D rescanning plan was 12.9 %, and the distribution contained values from 97.7 % to 110.6 %. For the conventional 4D ITV plan, the width of the D50 distribution was slightly smaller at 6.4 %, and contained values from 103.4 % and 109.8 %.

For the HI values, the difference between the conventional 4D rescanning plan and the 3 other plans was even more pronounced: apart from the increased upper limit of the whisker above 45 %, also the median HI value was significantly higher at 11.6 % for the conventional 4D rescanning plan. The other plans resulted in HI median values of 3.4 %, 3.4 % and 5.8 % for the robust 4D rescanning plan, the

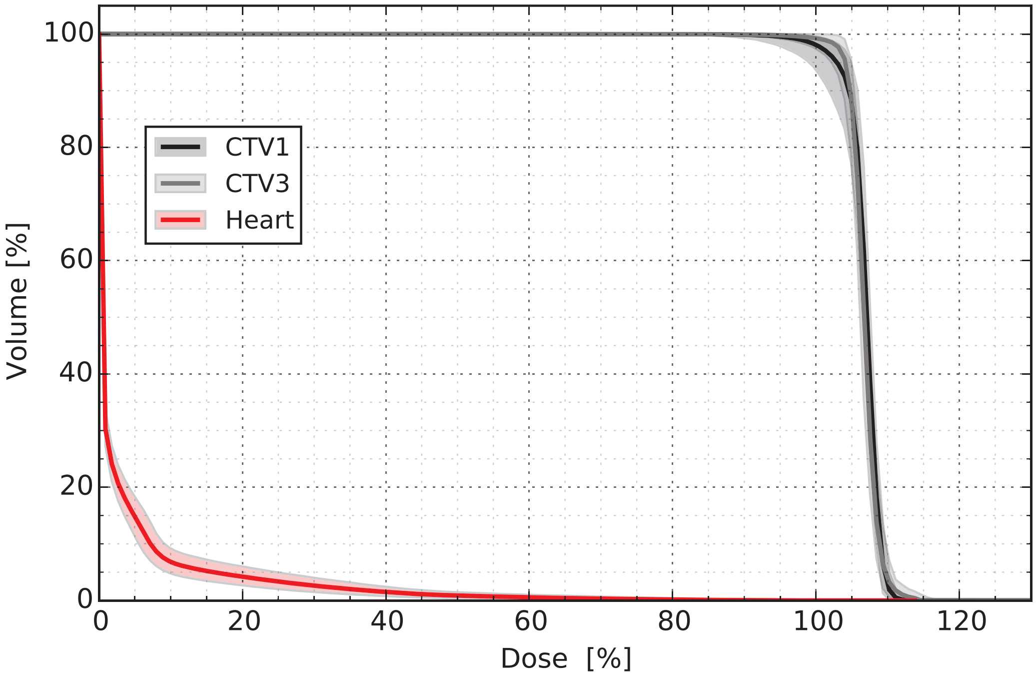

(a) Robust 4D ITV plan.

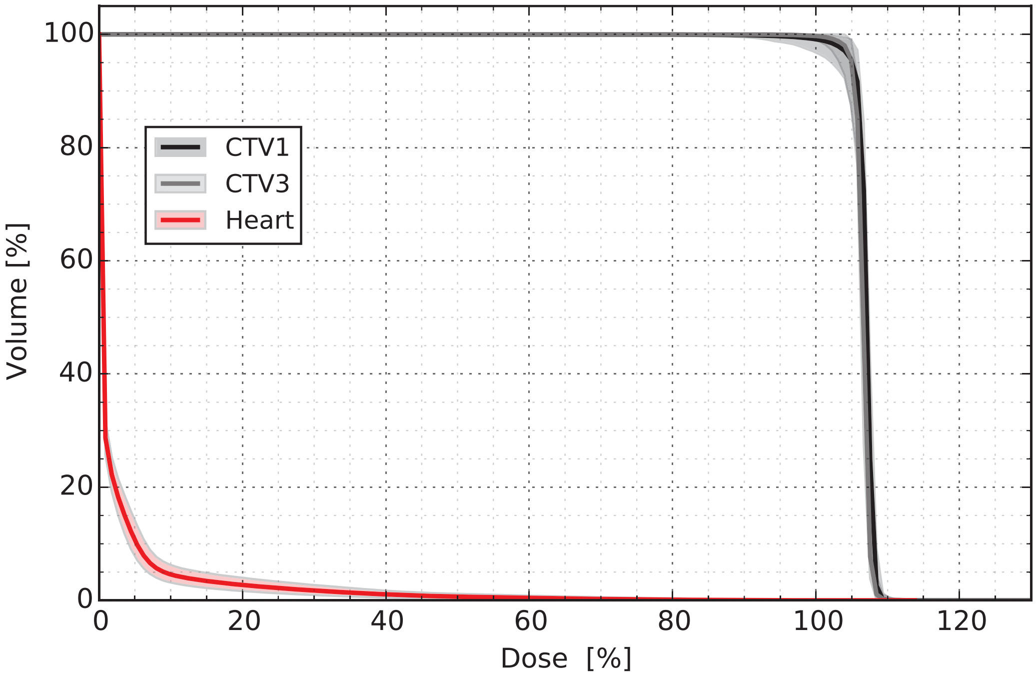

(b) Robust 4D rescanning plan.

Figure 4.6.: DVHs with uncertainty bands for the left lung lobe of patient 3, comparing robust 4D ITV and robust 4D rescanning. Robustness parameters were in both cases ±3 mm setup and ±3.5 % range uncertainty. The solid lines are average DVH curves and the light colored areas are uncertainty bands, depicting the envelope of all 21 4D dose distributions. All target DVHs are normalized to respective target doses and OAR DVHs are normalized to the corresponding limit value of the DVH constraints from Benedict et al. [2010].

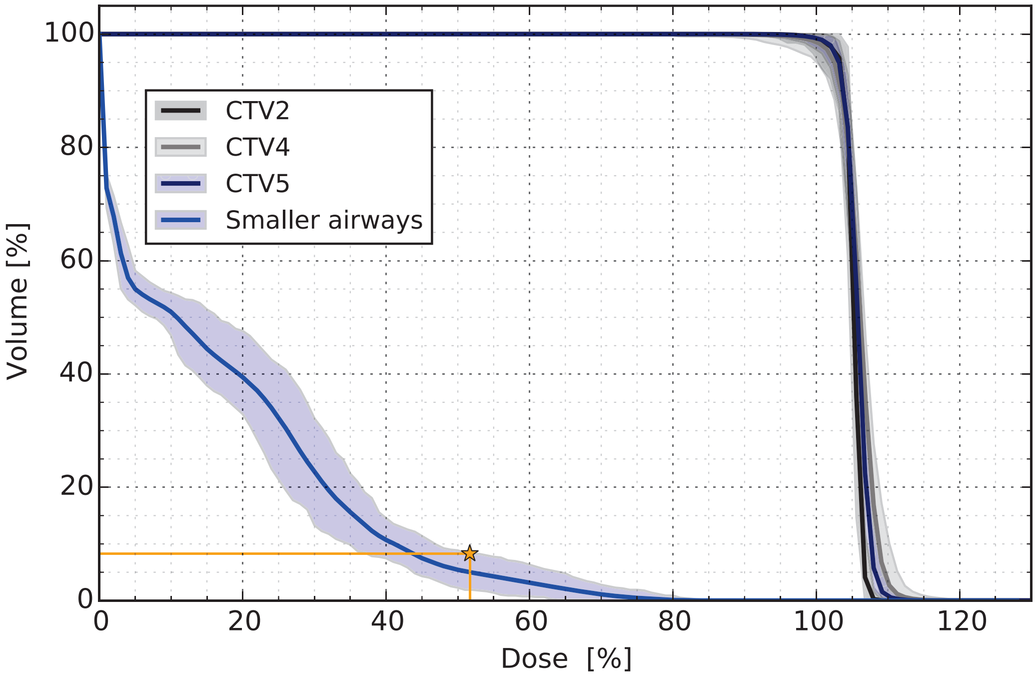

(a) Robust 4D ITV plan. The SA dose volume constraint is fulfilled in 98.8 % of uncertainty scenarios.

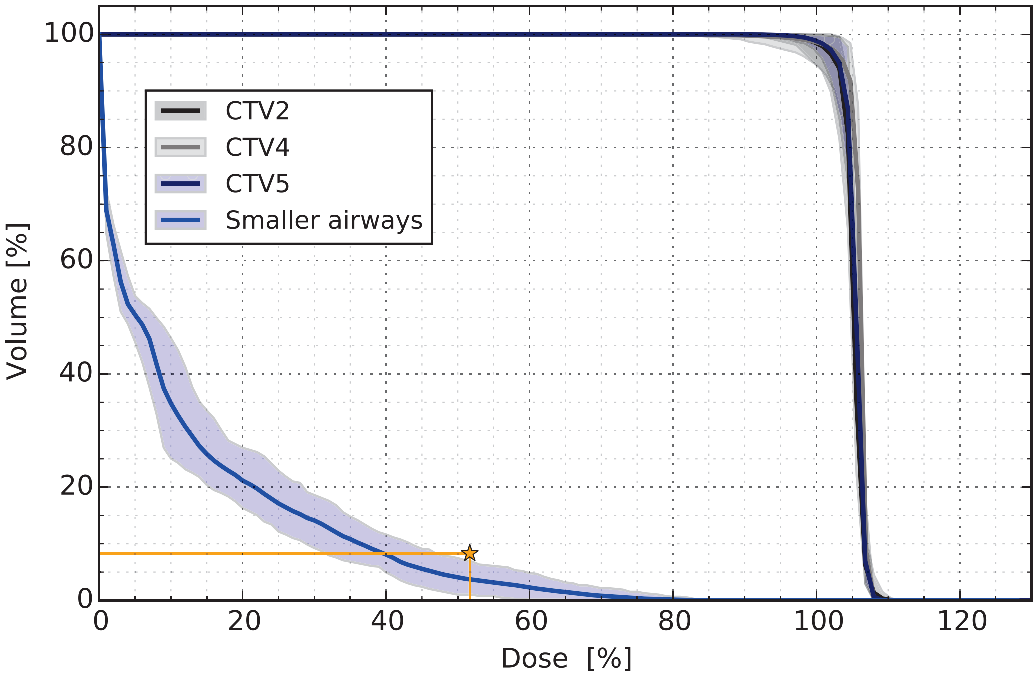

(b) Robust 4D rescanning plan. The SA dose volume constraint is fulfilled in 100.0 % of uncertainty scenarios.

Figure 4.7.: DVHs with uncertainty bands for the right lung lobe of patient 3, comparing (a) robust 4D ITV and (b) robust 4D rescanning. Robustness parameters were in both cases ±3 mm setup and ±3.5 % range uncertainty. The solid lines are average DVH curves and the light colored areas are uncertainty bands, depicting the envelope of all 21 4D dose distributions. Star symbols denote the dose volume constraint for the smaller airways ($D_{0.5cc} \leq 12.4$ GyE). All target DVHs are normalized to respective target doses and OAR DVHs are normalized to the corresponding limit value of the DVH constraints from Benedict et al. [2010].

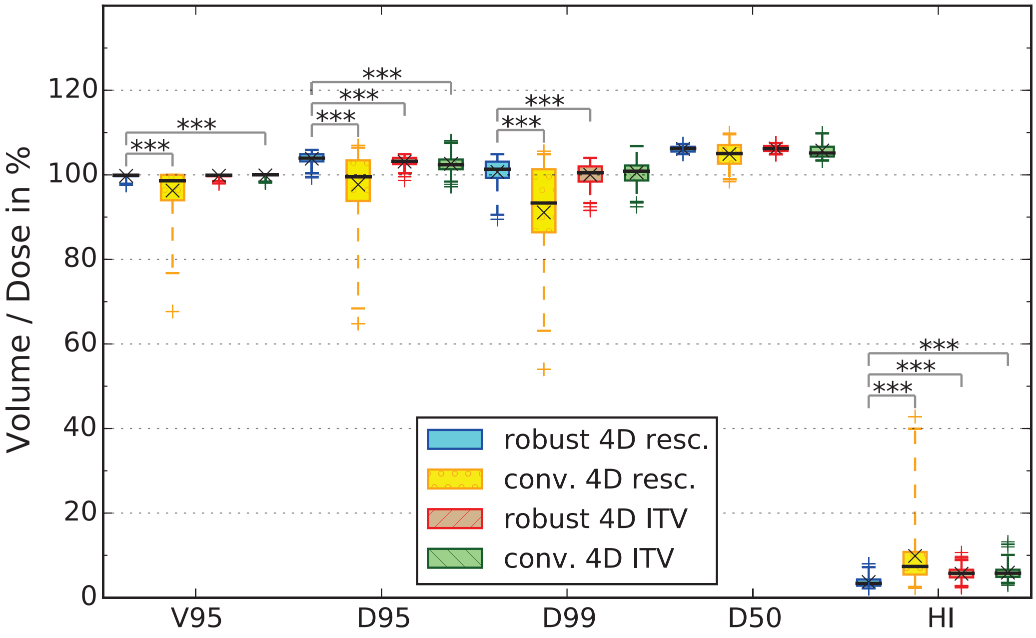

Figure 4.8.: Summarized CTV coverage of patient 3 shown as boxplots of V95, D95, D99, D5 and HI for the robust and conventional 4D ITV plans and for the robust and conventional 4D rescanning plans. The black lines indicate the median values, whereas the black X's denote the average values. The boxes represent the 1^{st} and 3^{rd} quantiles, while the whiskers represent the environment of 3 standard deviations. Statistical significance, calculated with an unsigned rank test, is indicated by a p-value ($^{*} \mapsto p < 0.05$, $^{**} \mapsto p < 0.01$, $^{***} \mapsto p < 0.001$).

robust 4D ITV plan, and the conventional 4D ITV plan, respectively. The significantly smallest distribution of HI values was generated by the robust 4D rescanning plan. In summary, the robust 4D rescanning plan provides the most robust target coverage, as also the D50 dose spread was the smallest.

OAR exposure

For patient 3, the dose exposure to several OARs is depicted in figures 4.9 and 4.10. The distributions of volume dose values D_{vol}, maximal point dose values D_{max}, and V5 values are shown as boxplots. Since D_{vol} and D_{max} were normalized to the limit values of the corresponding DVH constraints from Benedict et al. [2010], a constraint was counted as violated, when the value did exceed the 100 % mark. As can be seen in figure 4.9, no constraints were violated for esophagus, aorta, and trachea. For the majority of dose measurements and OARs, the conventional 4D rescanning plan yielded the lowest dose values, followed by the robust 4D rescanning plan, which yielded the second lowest dose values. There was no discernible trend for the robust and conventional 4D ITV plans, whose dose distributions consisted of higher values than for the two 4D rescanning plans for most of the OARs.

For the smaller airways, only the robust 4D rescanning plan could fulfill the dose volume constraint in all uncertainty scenarios, whereas the remaining plans violated the DVH constraint in at least some uncertainty scenarios: for the conventional 4D rescanning plan the DVH constraint was violated in 8.5 % of the scenarios and in 1.2 % for both the robust and the conventional 4D ITV plans. Although the maximal dose constraint was neglected for the original SBRT treatments of patient 3, both robust plans yielded lower D_{max} distributions than both conventional plans.

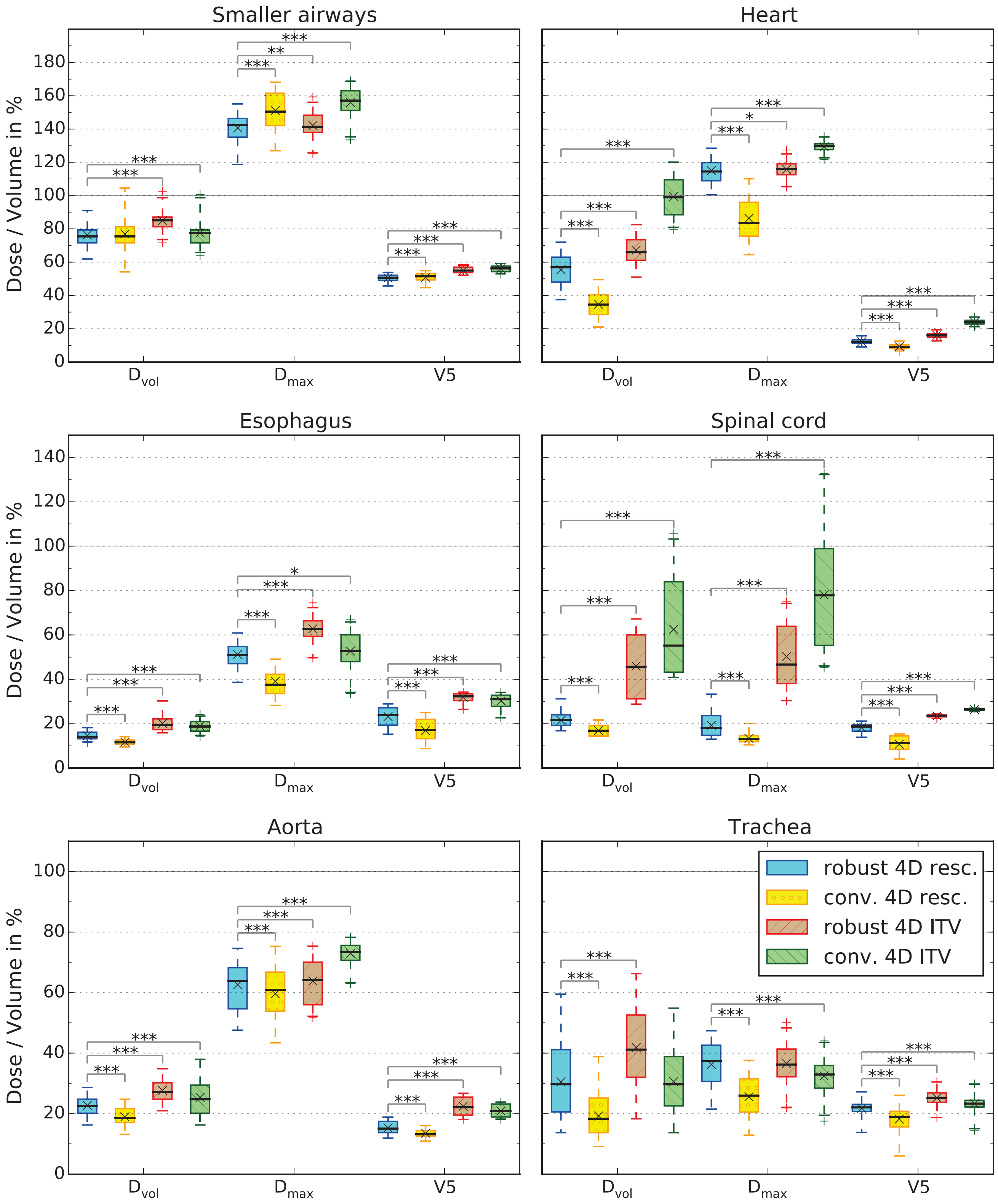

Figure 4.9.: OAR doses of patient 3 shown as boxplots of D_{vol}, D_{max} and V5. Results are shown for the robust 4D ITV plan and for the robust and conventional 4D rescanning plan. The black lines indicate the median values, whereas the black X's denote the average values. The boxes represent the 1^{st} and 3^{rd} quantiles, while the whiskers represent the environment of 3 standard deviations. Statistical significance, calculated with an unsigned rank test, is indicated by a p-value ($^{*} \mapsto p < 0.05$, $^{**} \mapsto p < 0.01$, $^{***} \mapsto p < 0.001$).

Apart from the conventional 4D ITV plan, the volume dose values of the heart were below the constraint for all three remaining methods, where the conventional 4D rescanning plan achieved the lowest values at a median D_{vol} of 34.5 %, followed by 57.0 % and 66.0 % for the robust 4D rescanning and the robust 4D ITV plans, respectively. The conventional 4D ITV plan violated the dose volume constraint for the heart in 52.4 % of the uncertainty scenarios, with a median D_{vol} value at 99.0 %. Except for the conventional 4D rescanning plan, the maximal dose constraint for the heart was violated for all three remaining plans in all considered uncertainty scenarios. It is to note, that the robust 4D rescanning plan, though violating the D_{max} constraint, still generated a significantly lower dose distribution than both the robust and the conventional 4D ITV plans.

For the spinal cord, the most unfavorable dose distribution was generated by the conventional 4D ITV plan. For conventional 4D ITV plan, the DVH constraints for D_{vol} and D_{max} were violated in 3.6 % and 23.8 % of the uncertainty scenarios, respectively. All other plans fulfilled the DVH constraints in all considered uncertainty scenarios with dose distributions significantly below the 100 % mark. The lowest dose exposures to the spinal cord were provided by both the conventional and the robust 4D rescanning plans, where the conventional 4D rescanning plan provided even lower dose values.

In absence of a maximal dose limit for the lung, the D_{max} values were normalized to the highest target dose in the corresponding lung lobe, which resulted in the following distributions as shown in figure 4.10. The lung doses were calculated for the lung volume minus the CTV volumes. In addition, values for V20 and V90 were stated in order to assess the low and high dose exposure to the lung. Since, as mentioned in chapter 3, the lung is a parallel organ, no limit is stated for the D_{max} values in Benedict et al. [2010], and the D_{max} values were normalized to the target doses. Although D_{max} values are not that important, the most favorable distribution of D_{max} values was generated by the conventional 4D ITV plan, while the most unfavorable distribution was yielded by the conventional 4D ITV plan. The V20 distributions were on similar levels for both the robust and the conventional 4D rescanning plans at about 25 %, and ther were significantly lower than both the robust and the conventional 4D ITV plans. Nonetheless, the significantly lowest distribution was generated by the robust 4D rescanning plan. The V90 values were on similar low levels for all 4 plans, where both 4D rescanning plans yielded the lowest values.

4.6 Discussion

Regarding the results for target coverage in context with OAR exposure, the use of 4D rescanning with conventional IMPT could not be recommended for patient 3. The uncertainty bands, as can be seen in the DVH in figure 4.5, were too large to ensure safe delivery of the prescribed dose to the target in presence of setup of range uncertainties. Although, compared to both robust plans and the conventional 4D ITV plan, the dose exposure to the critical organs was significantly lower for the conventional 4D rescanning plan, the huge uncertainties in target coverage neutralized this advantage. For the smaller airways, which have been the most critical organ in the studies performed by Anderle et al., both 4D rescanning methods fulfilled the volume dose constraint in more than 90 % of the considered uncertainty scenarios. When taking into account the significantly better target coverage provided by the robust 4D rescanning plan, patient 3 would profit even more from the robust 4D rescanning plan.

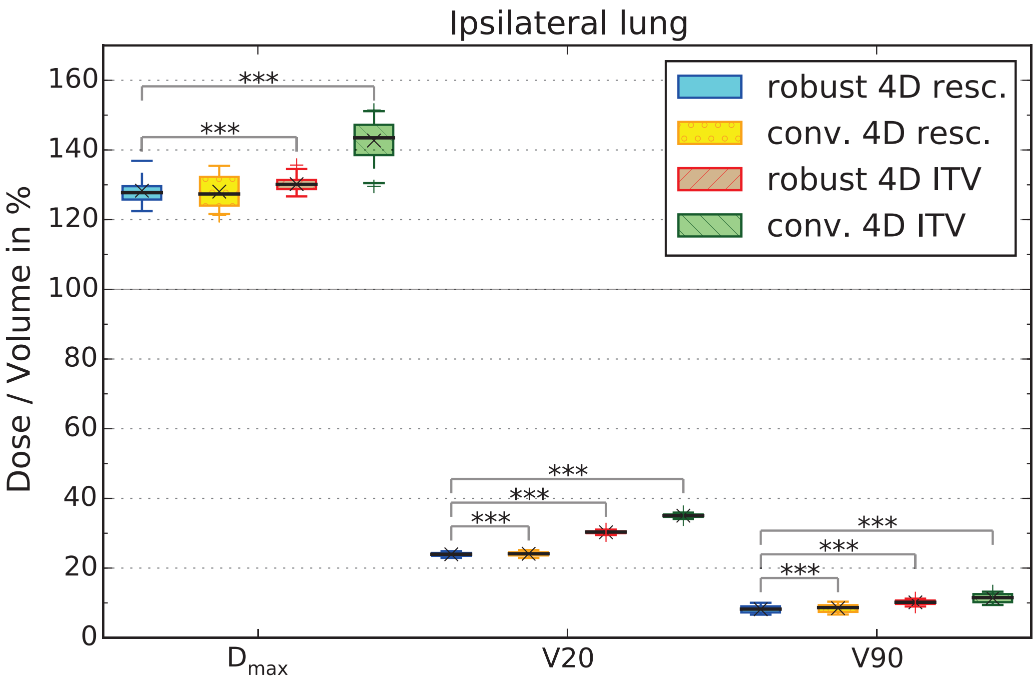

Figure 4.10.: Dose exposure of the ipisilateral lung of patient 3 as boxplots of D_{max}, V20 and V90. Results are shown for the robust 4D ITV plan and for the robust and conventional 4D rescanning plan. The black lines indicate the median values, whereas the black X's denote the average values. The boxes represent the 1st and 3rd quantiles, while the whiskers represent the environment of 3 standard deviations. Statistical significance, calculated with an unsigned rank test, is indicated by a p-value ($^{*} \mapsto p < 0.05$, $^{**} \mapsto p < 0.01$, $^{***} \mapsto p < 0.001$).

As shown in figure 4.3, the application of the conformal 4D rescanning strategy resulted in reduced safety margins around the CTVs, which led to reduced normal tissue dose. For the right lung lobe of patient 3, the shape of DVH curves of the smaller airways were even further improved, since there was a visible shift of the dose curves towards lower doses below 40 % of the target dose. As target coverage was almost not affected by the improved OAR sparing, robust 4D rescanning yielded a more favorable plan than robust 4D ITV optimization.

For the 4D dose calculations for the 4D rescanning plans, further consideration of residual motion is neglected, which could mean an overestimation of the plan quality. Nevertheless, for patient 3, the comparison between the robust 4D ITV plan and the robust 4D rescanning plan, showed only a small difference in D50 dose spread (as can be seen in table 4.1). This suggests, that including residual motion into 4D dose calculation for robust 4D rescanning plans would only increase the extension of the uncertainty bands to the level of D50 values yielde with the robust 4D ITV plan, which was still considerably lower than for both conventional plans.

The large values for the maximal point dose delivered to the heart were an issue for all 4 treatment planning strategies. In comparison to patient 23 presented in chapter 3, treatment planning for patient 3 showed a similar level of complexity: Due to the close proximity of the 2 left-sided tumors to the heart, the two objectives to reach high target coverage with D99 > 100 %, and to stay below the D_{max} limit for the heart, were found to be competitive. It was not possible to sufficiently accomplish both objectives simultaneously. Except for the conventional 4D rescanning plan, the corresponding DVH constraint was violated for the other 3 plans in all uncertainty scenarios considered in the robustness analysis. Even for the conventional 4D rescanning plan, the D_{max} limit was still exceeded in 14.3 % of the uncertainty scenarios. As the chosen voxel weights were smaller for CTV voxels than for heart voxels, and the OAR dose limit D_{limit} was set to 88 % of the prescribed dose, the sparing of the heart was expected to improve; however, the optimization resulted in treatment plans, which favored the fulfillment of the CTV objective. To maintain comparability, the same voxel weights and D_{limit} were used for all 4 optimization strategies, but as only the conventional plan generated reasonable sparing for the heart, further reduction of the OAR dose limit and higher heart voxel weights must be considered. However, as already suggested by the conventional 4D rescanning plan, further improvement of the heart spearing will be possibly achievable at the cost of CTV target coverage only. It is to mention, that both robust treatment planning strategies still yielded lower maximal heart doses than the conventional 4D ITV approach, given the same voxel weights and the for robust optimization empirically increased planned dose (as shown in table 3.1); however, the use of a fractionated treatment might be reasonable, at least for the left lung lobe of patient 3 with a prescribed dose of 27 Gy.

4.7 Conclusion

The robust 4D rescanning method, which relies on a library of robust treatment plans for each motion phase, enabled an increase of target coverage of moving tumors due to a more conformal irradiation, while simultaneously improving OAR sparing. Using the 4D rescanning approach with conventional IMPT, which relies on PTV margins, failed to provide sufficient target coverage, since large uncertainty bands were emanating in the DVHs in presence of patient setup errors or range uncertainties.

That conventional IMPT without range correction will tend to fail target coverage, was already shown by Graeff et al. This conclusion was the rationale for the proposal of 4D rescanning with SFUD on range specific ITVs [Graeff et al., 2012]. Robust 4D rescanning provides the benefit of straightforwardly using IMPT optimization, which allows to account for additional range uncertainties beyond the motion induced range changes implicitly considered via the different motion states of a 4DCT. In addition, robust optimization enables the reduction of dose gradients between treatment fields, which considerably increases treatment plan robustness against patient setup errors or particle range changes.

Although, the method has been only tested in-silico for a single patient, the trend for improved plan quality is already evident. Compared to the robust 4D ITV method, the translation of 4D rescanning to be used in a clinical setting is more complicated, since also changes to the treatment control system are required. So far, this method has been only implemented at GSI [Graeff et al., 2013]; however, there is an ongoing cooperation with National Center of Oncological Hadrontherapy, Pavia, Italy (CNAO) to update the medical cave at GSI with the latest TCS of the CNAO facility, and to implement 4D rescanning into the CNAO TCS. On a long-term view, this cooperation could facilitate the use of 4D rescanning in clinical trials.

In particular, when a particle therapy facility does not have an exceptional accelerator, such as HIMAC (in Chiba, Japan), which provides extremely fast gating and rescanning, the approach of robust 4D rescanning could be a promising method to treat moving tumors. As shown in this chapter, robust 4D rescanning could accomplish beneficial treatment delivery with significantly improved OAR sparing, while providing sufficient target coverage.

5 Discussion

In this chapter, the results of the previous chapters 2, 3 and 4 are discussed in a comprehensive perspective.

5.1 Robust optimization for carbon ions

As described in the introduction of chapter 2, a variety of different robust optimization methods currently exists for proton therapy. That carbon therapy shares the same susceptibilities to patient setup errors and particle range changes as proton therapy, was the main rationale of transferring those robust optimization methods to carbon ion therapy. In addition, robust optimization methods provide smoothing of internal dose gradients, which can occur when MFO IMPT optimization is used.

Although the physical principals are the same for proton and carbon ion therapy, the consideration of a variable RBE during treatment planning for carbon ion therapy does increase the complexity of the biological dose calculation, and requires the use of nonlinear optimization algorithms. Thus, compatibility with biological dose optimization led to the decision of adapting a voxel-wise worst-case optimization method for the GSI in-house TPS, TRiP4D. The implemented worst-case optimization is currently based on the consideration of 9 uncertainty scenarios in total, including a nominal scenario, two range uncertainty scenarios with rang overshoots and range undershoots, and six setup error scenarios where the patient's isocenter is shifted in direction of the major anatomical axis.

As shown for a RA in chapter 2, the treatment plans generated with robust optimization showed increased robustness, not only against the 9 uncertainty scenarios, which were already considered in the worst-case optimization, but also against the superposition of range changes and setup errors, which resulted in a total of 21 uncertainty scenarios. Compared to conventional optimization, robust optimization increased the robustness of the target dose distribution, which was expressed by a considerable reduction of the uncertainty bands around the average DVH curve and an improvement of the HI values, showing convergence of the DVHs to the ideal step shape. These results were expected, as the worst-case method has already been successfully used for proton plan optimization. Nonetheless, using the plain worst-case cost function as proposed for robust optimization of proton treatment plans, led to considerable overdosage of the target volume for carbon ions. In the basic version of the worst-case cost function, as shown in equation (2.2), the scenario with the lowest dose is selected for target voxels and the scenario with the highest dose is selected for OAR voxels. The explanation for the generation of overdosage in the target volume was found to be the absence of a correction term for the maximum dose in the robust cost function. Due to the selection of the scenario delivering the lowest dose to a corresponding target on a voxel-wise basis, the robust optimizer only adapts particle numbers for underdosed target voxels, which will typically result in an increase of particle numbers, and therefore in an increase of dose delivered to the target volume. At least for the conjugate gradient optimization algorithm used in TRiP4D, the robust cost function presented in equation (2.2) prevents a reasonable limitation of the maximum dose delivered to the target volume.

The generation of target overdosage can be suppressed by introducing an additional maximum dose term into the robust cost function, as described in equation (2.3). For robust proton plan optimization, such a maximum dose term has been originally proposed by Liu et al. [2012] as an optional measure to avoid hot spots within the target dose distribution. For the robust optimization of carbon ion treatment plans, this maximum dose term is no longer optional and becomes vital in order to generate robust treatment plans without unrestricted overdosage, and is therefore highly recommended. Consequently, the maximum dose term was used for robust 4D ITV optimization in the patient study presented in chapter 3, and for robust 4D rescanning in chapter 4.

5.2 Robust optimization with opposing objectives

In chapter 3, a robust version of the 4D ITV optimization approach, as proposed by [Anderle, 2016], based on the work of [Graeff, 2014], was presented. The robust 4D ITV strategy used the worst-case cost function as presented in chapter 2, including the maximum dose term and was tested on a cohort of 8 complex lung cancer patients. These patients were the same 8 lung cancer patients as described in the study by Anderle et al. [2018]. To maintain compatibility, the same objectives for target coverage and OAR sparing have been adopted from Anderle et al. [2018]. For target volumes, the objective was to provide D99 values $\geq 100\,\%$, and for critical organs, the objective was to meet the OAR dose limits described by [Benedict et al., 2010].

Huge effort was put by Anderle et al. into the treatment planning, and into the treatment planning software TRiP4D, in order to achieve these objectives as best as possible. This included the implementation of multiple target optimization and the implementation of objective optimization, where the entire optimization is repeated several times adapting weights and planned dose on a voxel-wise basis, until the desired objective is fulfilled. In the study of Anderle et al., plan robustness was tested for 4 respiratory motin patterns only. Although 4D dose calculation implicitly considered temporal changes of patient anatomy, the dose calculation was performed on a nominal case only, not considering any further uncertainties. A robustness analysis, as described in chapter 2, revealed that in presence of patient setup errors and range uncertainties, the delivered dose distributions can be considerably deteriorated.

Using the robust 4D ITV planning strategy, uncertainty in dose distributions could be reduced in many cases, improving target coverage and OAR sparing simultaneously. Over all patients, the plan acceptance rate for fulfillment of the smaller airways DVH constraint could be raised from 79.8 % of the considered uncertainty scenarios for the conventional 4D ITV plans to 98.8 % for the robust 4D ITV plans. It is to note, that there are cases, where the robust 4D ITV approach reaches its limits, for example when a target volume overlaps with a critical organ. This situation was found in patient 23, where the tumor volume overlapped with the smaller airways. Here, the current implementation of the robust optimization was only able to fulfill one of the two required objectives: when robustness was increased for the target coverage, the OAR exposure was considerably increased simultaneously and vice versa. Unless this issue is overcome, for complex cases, the robust treatment planning using the worst-case method will result in two extreme kinds of treatment plans, one favoring robust target coverage, the other providing robust OAR sparing. Here, the experienced decision of a physician, on which of both objectives it to prioritize, is required. Possible improvements to the presented robust optimization algorithms are mentioned in the outlook chapter.

5.3 Study limitations

The 4D dose calculations presented in chapter 3, were based on regular respiratory motion patterns, which are typically not present during real patient treatments, where respiratory amplitude and period are most likely to vary over time, between 4DCT acquisition and actual treatment, and during the treatment delivery itself. The topic of irregular patient motion is currently investigated at GSI: an adapted 4D dose calculation algorithm has recently been implemented and is currently undergoing tests. This algorithm relies on a huge series of 4DCT data, which represent the temporal changes in patient anatomy over numerous respiration cycles. So far, it is still unclear how to reasonably produce comparable data for real patients. As a substitute for current testing purposes, these image data sets are artificially generated with the XCAT phantom. A potential solution for the generation of real patient data could be the use of 4D MRI images which are registered on a CT image [Boye et al., 2013]. Hence, the results of the robust 4D ITV optimization are so far only valid for regular motion.

A further limitation of this study is caused by the deformable image registration (DIR), which is used for contour propagation or transformation of pencil beam contributions of different motion phases to the reference phase. As shown in [Anderle, 2016], DIR can generate errors such as deficient inverse consistency, where the initial starting point is not recovered, when first using the forward transformation map, which leads from the moving frame to the reference frame, and subsequent use of the corresponding backward transformation map, which leads from the reference frame to the moving frame. When comparing conventional and robust treatment plans which used the same deformation maps during optimization and 4D dose calculation, those errors due to DIR should be marginal extent; however, this has to be kept in mind, when results of carbon ion treatment planning is compared to photon therapy, as done in Anderle et al. [2018]. To mitigate these potential errors, Kristjan Anderle proposed a strategy for quality assurance of image registrations, which is already published as a module for Slicer3D [Anderle, 2016].

5.4 Robust methods for conformal 4D optimization

The use of the worst-case method to optimize robust carbon ion treatment plans was successfully used for the 4D ITV and for the 4D rescanning approach. For both strategies, robustness against patient positioning errors and range changes could be increased. Both strategies allowed for generation of field-specific range margins which were beyond the motion induced range changes, which are implicitly accounted for by using the information on temporal changes of a patient's anatomy provided by 4DCTs.

For the patient study presented in chapter 3, where the 4D ITV approach was compared for robust and conventional optimization, the issue with opposing objectives (as described in the previous section) appeared in cases of close proximity between target volumes and critical structures. In these cases, the robust 4D ITV approach reached its limits.

This is where robust 4D rescanning could be advantageous due to the more conformal irradiation of the moving target. At least for patient 3, which was exemplarily presented in chapter 4, the robust 4D rescanning plan yielded a similar target coverage while OAR doses were decreased in the majority of critical organs, compared to the robust 4D ITV method. The dose reduction was especially pronounced for the smaller airways and the heart. It is to note that, although robust 4D rescanning yielded promising results, the 4D dose calculation for this method assumes perfect delivery of each phase RST to the corresponding motion state. As perfect delivery is unlikely to occur, further degradation of the dose distributions for real patient treatments must be expected.

5.5 Robust optimization allows safe IMPT for complex patients

As shown in chapters 2, 3 and 4, the assumption of a static dose cloud is not given. In presence of patient setup errors and range uncertainties, the deterioration of the delivered dose distribution can not be mitigated by conventional, isotropic PTV margins, as used in photon radiotherapy. In these cases, robust optimization allows for the safe application of IMPT in carbon ion therapy, also when dose gradients are present in the target area.

In case of 4D treatment planning, the use of robust optimization is even more beneficial, as conventional 4D optimization enables the consideration of motion induced range changes, but leads to field-specific changes of the treatment volume at the same time, when range margins are applied; however, congruent treatment volumes are a requirement for safe IMPT. The robust optimization algorithm allows for the incorporation of field-specific range changes and simultaneous IMPT optimization on congruent target volumes. Robust 4D optimization additionally enables the consideration of global range changes due to respiratory motion.

Only with robust 4D optimization strategies, as presented in this thesis, it is possible to safely plan carbon ion treatments with IMPT for complex lung cancer patients with large tumor motion and OARs in close proximity.

6 Outlook

A first topic, which could be investigated in further studies, is the elimination of the exclusive assignment of voxel as target or OAR in TRiP4D. This approach could improve the robustness of treatment plans in patient cases, were the target is in close proximity to a critical structure. Potentially, this modification could also enable multi criteria objective optimization with opposing objectives, as presented in chapter 3 and 4.

Similar effects could be tested by implementing an *all-plan* or *minimax* optimization, which would avoid the overly conservative plans which are generated by the worst-case method. Especially the implementation of a minimax approach, as proposed by Fredriksson et al. [2011], should be fairly straightforward to implement into TRiP4D by a rearrangement of sub parts of the optimization algorithm. To achieve a minimax optimization, the step in the algorithm, where the worst-case is selected from a set of scenarios on a voxel-wise basis, would need to be shifted to the level of the cost function itself. For a set of cost functions, which are established from a set of uncertainty scenarios, the worst-case is the cost function generating the highest value. When in each iteration step of the optimization the cost-function with the highest value is selected, this leads to a minimization of the maximum value of the cost-function, which also describes the name origin of this method.

The all-plan approach would base on the 4D optimization introduced into TRiP4D by Graeff et al. Already in the non-robust 4D optimization, there is a distinctive field dose correlation (FDC) matrix for each motion state, set to be independent and of equal weights. These motion-state-specific FDC matrices are co-existing during the optimization, all contributing to the calculation of gradient of the cost function which determines the next optimization step. By also considering all uncertainty scenarios per motion phase as equal and independent possibilities, a (robust) all-plan optimization could be achieved.

An interesting approach has been proposed by Engwall et al. [2018], where temporal uncertainties during delivery are already accounted for during the plan optimization. Partial doses of pencil beams in different motion states are calculated and transformed to a reference phase, using the transformation maps from a deformable image registration, which is done for different respiratory cycles. Further on, these results are used as input for a robust optimization using the minimax method. Engwall et al. have shown for 3 NSCLC stage IV patients, that their proposed method can reduce the dose degradation caused by interplay. Due to the nonlinearity of the RBE-weighted biological dose calculation in TRiP and the complexity of the temporal correlation between treatment delivery and respiratory motion, the implementation of the approach proposed by Engwall et al. into TRiP4D could become difficult.

Eventually, the robust optimization methods could be tested on consecutive patient data sets, such as weekly re-CTs, which describe anatomical variations of the patient in a more realistic manner. In particular, when compared to the simplified approach of shifting the isocenter or globally manipulating CT density to generate range changes. Weekly 4DCTs with clinical high precision patient positioning are currently quite rare; however, by future cooperation with the particle therapy center in Marburg and Dresden, suitable patient data sets should be soon available.

A Appendix of Chapter 2

A.1 TRiP commands for robust optimization

A.1.1 Robust field setup

Before performing a robust optimization in TRiP4D, the uncertainty parameters for the robust fields which will include the different uncertainty scenarios have to be stated. This step is done during the normal field setup. There are two basic commands (the *-symbol indicates the minimum characters required for TRiP4D to identify the command):

- **robustrange*shift($\Delta_{\mathbf{range}}$):** add 2 range scenarios with shifted CT density (by $\pm\Delta_{\mathrm{range}}\,[\%]$).
- **robustrange*shift($\Delta_{\mathbf{position}}$):** add 6 position scenarios with a shifted iso-center in all major directions (by $\pm\Delta_{\mathrm{position}}\,[\%]$)

If these two commands are appended to the normal field commands with typical parameters like $\Delta_{\mathrm{range}} = 3.5\,\%$ $\Delta_{\mathrm{position}} = 3\,\mathrm{mm}$, 8 additional uncertainty scenarios are generated on top of the nominal case, resulting in 9 possible scenarios per field. It is important, that **all** treatment fields used in an optimization contain the **same number** of scenarios. Otherwise the optimization will interrupt. The combination of robust and non-robust fields is not possible in TRiP4D so far, although the question arises if it would be reasonable at all. It is also recommended to use the same robust parameters for all field targeting the same CTV.

Besides the basic setup of robust fields the commands already mentioned have also the ability of processing additional parameters: The additional parameters for the **robustrangeshift** command is a systematic H2O offset in mm, which gets added onto the H2O range of the high CT density scenario and gets subtracted from the low CT density scenario:

- **robustrange*shift($\Delta_{\mathbf{range}}, \Delta_{\mathbf{H2O}}$):** add 2 range scenarios with shifted CT density (by $\pm\Delta_{\mathrm{range}}\,[\%]$) with an additional H2O offset of $\pm\Delta_{\mathrm{H2O}}\,[\mathrm{mm}_{\mathrm{H2O}}]$.

The **robustpositionshift** command generates an isotropic shift of the iso-center in all major directions. If more anisotropic shifts are desired, this can be done by append more parameters, affecting the major CT directions independently:

- **robustpos*itionshift($\Delta x, \Delta y, \Delta z$):** add 6 position scenarios with a shifted iso-center by $\pm\Delta x$ in x-, $\pm\Delta y$ in y- and $\pm\Delta z$ in z-direction, respectively.

For completely independent anisotropic position shifts, the parameters for each direction can also be split up in two values, one in the positive direction of the chosen axis, the other in negative direction:

- **robustpos*itionshift($-\Delta x, +\Delta' x, -\Delta y, +\Delta' y, -\Delta z, +\Delta' z$):** add 6 position scenarios with a shifted iso-center by $-\Delta x$ and $+\Delta' x$ in x-, $-\Delta y$ and $+\Delta' y$ in y- and $-\Delta z$ and $+\Delta' z$ in z-direction, respectively.

As described in chapter 2 it is also possible to create an additional RBE scenario for the robust optimization, which is generated by the following command:

- **robustRBE*uncertainty(Δ_{RBE}):** adds a robust scenario with RBE uncertainty, scaling the RBE values by $+\Delta_{\mathrm{RBE}}[\%]$ for OAR voxel and $-\Delta_{\mathrm{RBE}}[\%]$ for target voxel.

A.1.2 Robust optimization

If robust treatment fields are set up, TRiP4D automatically performs a robust optimization. Robust optimization is available for physical and biological plan optimization using the Fletcher-Reeves conjugate gradient algorithm (FR) or the most recent and faster implementation of Fletcher-Reeves (FDCS).

The robust optimization supports multi threading, which is recommended to use, to save computation time. The number of threads can be requested by the already existing command **maxthreads(N_{max})**. The default value is 1 thread.

An additional parameter for robust optimization is the dose weight for the *maximal dose term* of the cost function (as described in section 2.2.3):

- **maxdosew*eightfactor(w_{MDW}):** which can be any positive real number. The default value is 1.0.

As described in chapter 2 it is recommended to always use the maximal dose term in the cost function for the robust optimization, since it significantly reduces over dose in the target volume.

A.1.3 Additional commands for robustness analysis

For the insertion of patient setup errors or range uncertainties into the dose calculation, the following commands can be used.

To affect the particle ranges, the CT density can be altered by shifting the value of the Hounsfield unit lookup (as described in chapter 2). After the HLUT is loaded for a dose calculation, it can be shifted by the following command:

- **hlut / s*hift(Δ_{range}):**, which shifts the value by Δ_{range} [%].

To model a patient setup error, the target point of the assigned field is shifted, i.e. the patient's iso-center, while the treatment fields are loaded:

- **field / sh*ifttarget($\Delta x, \Delta y, \Delta z$)** shifts the patient's iso-center in the field by $\Delta x, \Delta y$ and Δz in [mm].

So far the shifttarget command is field specific, meaning, that in the case of a multiple field optimization, the same shift must be applied in all corresponding fields.

B Appendix of Chapter 3

B.1 Dose limits for organs at risk

OAR dose limits used in SBRT and PT treatment planning for different fractionation schemes are shown in table B.1. Two limits were used: The first limitation was a maximum dose to single voxel D_{Max} and the second a maximum dose deposited to a specific OAR volume D_{Volume}.

Organ	**Critical volume [cc]**	**Volume dose [Gy]**			**Maximum point dose [Gy]**		
		1	**3**	**5**	**1**	**3**	**5**
Heart	15.0	16.0	22.0	24.0	30.0	32.0	38.0
Spinal cord	0.35	10.0	14.0	18.0	21.9	23.0	30.0
Smaller airways	0.5	12.4	13.3	18.9	23.1	21.0	33.0
Esophagus	5.0	11.9	15.4	17.7	25.2	19.5	35.0
Trachea	4.0	10.5	20.2	15.0	30.0	16.5	40.0
Aorta	10.0	31.0	37.0	39.0	45.0	47.0	53.0
Stomach	10.0	11.2	12.4	16.5	22.2	18.0	32.0

Table B.1.: Dose constraints for various OARs for 1, 3 and 5 fractions, denoted as respective numbers. Limits were used in SBRT and PT treatment planning. Data taken from [Benedict et al., 2010].

References

AACR (2012). American Association for Cancer Research – Cancer Progress Report 2012. *Clin. Cancer Res.*, 18(Supplement 1):S1–S100.

ACS (2017). NSCLC 5-year survival rates by staging. https://www.cancer.org/cancer/non-small-cell-lung-cancer/detection-diagnosis-staging/survival-rates.html, accessed 2018-09-04.

Ahlen, S. (1980). Theoretical and experimental aspects of the enery loss of relativistic heavily ionizing particles. *Rev. Mod. Phys.*, 52(1):121.

Anderle, K. (2016). *In-silico comparison of photons versus carbon ions in single fraction therapy of lung cancer*. PhD thesis, TU Darmstadt.

Anderle, K., Stroom, J., Pimentel, N., Greco, C., Durante, M., and Graeff, C. (2016). In silico comparison of photons versus carbon ions in single fraction therapy of lung cancer. *Phys. Med.*, 32(9):1118–1123.

Anderle, K., Stroom, J., Vieira, S., Pimentel, N., Greco, C., Durante, M., and Graeff, C. (2018). Treatment planning with intensity modulated particle therapy for multiple targets in stage IV non-small cell lung cancer. *Phys. Med. Biol.*, 63(2):025034 (10pp).

Baumann, M., Appold, S., Petersen, C., Zips, D., and Herrmann, T. (2001). Dose and fractionation concepts in the primary radiotherapy of non-small cell lung cancer. *Lung Cancer*, 33:S35–S45.

Belderbos, J., Heemsbergen, W., Hoogeman, M., Pengel, K., Rossi, M., and Lebesque, J. (2005). Acute esophageal toxicity in non-small cell lung cancer patients after high dose conformal radiotherapy. *Radiother. Oncol.*, 75(2):157–164.

Benedict, S. H., Yenice, K. M., Followill, D., Galvin, J. M., Hinson, W., Kavanagh, B., Keall, P., Lovelock, M., Meeks, S., Papiez, L., Purdie, T., Sadagopan, R., Schell, M. C., Salter, B., Schlesinger, D. J., Shiu, A. S., Solberg, T., Song, D. Y., Stieber, V., Timmerman, R., Tome, W. A., Verellen, D., Wang, L., and Yin, F. F. (2010). Stereotactic body radiation therapy: the report of AAPM Task Group 101. *Med. Phys.*, 37(8):4078–4101.

Bert, C., Gemmel, A., Chaudhri, N., Lüchtenborg, R., Saito, N., Durante, M., and Rietzel, E. (2009). Rescanning to mitigate the impact of motion in scanned particle therapy. In *GSI Sci. Rep.*

Bert, C., Gemmel, A., Saito, N., Chaudhri, N., Schardt, D., Durante, M., Kraft, G., and Rietzel, E. (2010). Dosimetric precision of an ion beam tracking system. *Radiat. Oncol.*, 5(1):61.

Bert, C., Groezinger, S. O., and Rietzel, E. (2008). Quantification of interplay effects of scanned particle beams and moving targets. *Phys. Med. Biol.*, 53(9):2253–2265.

Bert, C. and Rietzel, E. (2007). 4D treatment planning for scanned ion beams. *Radiat. Oncol.*, 2(1):24–34.

Bethe, H. (1930). Zur Theorie des Durchgangs schneller Korpuskularstrahlung durch Materie. *Ann. Phys.*, 5(5):325–400.

Bloch, F. (1933). Zur Bremsung rasch bewegter Teilchen beim Durchgang durch Materie. *Ann. Phys.*, 5(16):285–321.

Bohr, N. (1940). Scattering and stopping of fission fragments. *Phys . Rev.*, 58(7):654 – 655.

Boye, D., Lomax, T., and Knopf, A. (2013). Mapping motion from 4D-MRI to 3D-CT for use in 4D dose calculations: a technical feasibility study. *Med. Phys.*, 40(6):061702.

Bragg, W. H. and Kleeman, R. (1904). LXXIV. on the ionization curves of radium. *Lond. Edinb. Dubl. Phil. Mag. J. Sci.*, 8(48):726–738.

Britton, K. R., Starkschall, G., Tucker, S. L., Pan, T., Nelson, C., Chang, J. Y., Cox, J. D., Mohan, R., and Komaki, R. (2007). Assessment of gross tumor volume regression and motion changes during radiotherapy for non-small-cell lung cancer as measured by four-dimensional computed tomography. *Int. J. Radiat. Oncol. Biol. Phys.*, 68(4):1036–1046.

Brock, K. K. (2010). Results of a multi-institution deformable registration accuracy study (MIDRAS). *Int. J. Radiat. Oncol. Biol. Phys.*, 76(2):583–596.

Brock, K. K., Dawson, L. A., Sharpe, M. B., Moseley, D. J., and Jaffray, D. A. (2006). Feasibility of a novel deformable image registration technique to facilitate classification, targeting and monitoring of tumor and normal tissue. *Int. J. Radiat. Oncol. Biol. Phys.*, 64(4):1245–1254.

Brown, W. T., Wu, X., Fayad, F., Fowler, J. F., Amendola, B. E., Garcia, S., Han, H., de la, Z. A., Bossart, E., Huang, Z., and Schwade, J. G. (2007). Cyberknife radiosurgery for stage I lung cancer: results at 36 months. *Clin. Lung Cancer.*, 8(8):488–492.

Chatterjee, A. and Schaefer, H. J. (1976). Microdosimetric structure of heavy ion tracks in tissue. *Radiat. Environ. Biophys.*, 13:215–227.

Chu, W. T., Ludewigt, B. A., and Renner, T. R. (1993). Instrumentation for treatment of cancer using proton and light-ion beams. *Rev. Sci. Instrum.*, 64(8):2055–2122.

Connell, P. P. and Hellman, S. (2009). Advances in radiotherapy and implications for the next century: A historical perspective. *Cancer Res.*, 69(2):383–392.

Coolidge, W. D. (1913). A powerful Röntgen ray tube with a pure electron discharge. *Phys. Rev.*, 2:409–430.

CRUK (2015). Lung cancer stages I and IV, cancer research uk [cc by-sa 4.0 (`http://creativecommons.org/licenses/by-sa/4.0`)], via wikimedia commons.

Ebner, D. K., Tsuji, H., Yasuda, S., Yamamoto, N., Mori, S., and Kamada, T. (2017). Respiration-gated fast-rescanning carbon-ion radiotherapy. *Jpn. J. Clin. Oncol.*, 47(1):80–83.

Elsaesser, T. and Scholz, M. (2006). Improvement of the local effect model (LEM)–implications of clustered DNA damage. *Radiat. Prot. Dosimetry*, 122(1-4):475–477.

Elsaesser, T. and Scholz, M. (2007). Cluster effects within the local effect model. *Radiat. Res.*, 167(3):319–329.

Elsaesser, T., Weyrather, W. K., Friedrich, T., Durante, M., Iancu, G., Krämer, M., Kragl, G., Brons, S., Winter, M., Weber, K. J., and Scholz, M. (2010). Quantification of the relative biological effectiveness for ion beam radiotherapy: direct experimental comparison of proton and carbon ion beams and a novel approach for treatment planning. *Int. J. Radiat. Oncol. Biol. Phys.*, 78(4):1177–1183.

Engwall, E., Fredriksson, A., and Glimelius, L. (2018). 4D robust optimization including uncertainties in time structures can reduce the interplay effect in proton pencil beam scanning radiation therapy. *Med. Phys.*

Fakiris, A. J., McGarry, R. C., Yiannoutsos, C. T., Papiez, L., Williams, M., Henderson, M. A., and Timmerman, R. (2009). Stereotactic body radiation therapy for early-stage non–small-cell lung carcinoma: four-year results of a prospective phase II study. *Int. J. Radiat. Oncol. Biol. Phys.*, 75(3):677–682.

Fowler, J. F. (1989). The Linear-Quadratic formula and progress in fractionated radiotherapy. *Brit. J. Radiol.*, 62(740):679–694.

Fredriksson, A., Forsgren, A., and Hårdemark, B. (2011). Minimax optimization for handling range and setup uncertainties in proton therapy. *Med. Phys.*, 38(3):1672–1684.

Freund, L. (1897). Ein mit Röntgen-Strahlen behandelter Fall von Naevus pigmentosus piliferus. *Wien. Med. Wochenschr.*, 47:428–434.

Friedrich, T., Grün, R., Scholz, U., Elsässer, T., Durante, M., and Scholz, M. (2013). Sensitivity analysis of the relative biological effectiveness predicted by the local effect model. *Phys. Med. Biol.*, 58(19):6827.

Friedrich, T., Scholz, U., Durante, M., and Scholz, M. (2014). RBE of ion beams in hypofractionated radiotherapy (SBRT). *Phys. Med.*, 30(5):588–591.

Friedrich, T., Scholz, U., Elsässer, T., Durante, M., and Scholz, M. (2012). Calculation of the biological effects of ion beams based on the microscopic spatial damage distribution pattern. *Int. J. Radiat. Biol.*, 88(1-2):103–107.

Furukawa, T., Inaniwa, T., Sato, S., Shirai, T., Mori, S., Takeshita, E., Mizushima, K., Himukai, T., and Noda, K. (2010). Moving target irradiation with fast rescanning and gating in particle therapy. *Med. Phys.*, 37(9):4874–4879.

Gagliardi, G., Constine, L. S., Moiseenko, V., Correa, C., Pierce, L. J., Allen, A. M., and Marks, L. B. (2010). Radiation dose–volume effects in the heart. *Int. J. Radiat. Oncol. Biol. Phys.*, 76(3):S77–S85.

Gemmel, A., Rietzel, E., Kraft, G., Durante, M., and Bert, C. (2011). Calculation and experimental verification of the RBE-weighted dose for scanned ion beams in the presence of target motion. *Phys. Med. Biol.*, 56:7337–7351.

Goldhaber, A. S. and Heckman, H. H. (1978). High energy interactions of nuclei. *Ann. Rev. Nucl. Part. Sci.*, 28(1):161–205.

Goldstraw, P., Chansky, K., Crowley, J., Rami-Porta, R., Asamura, H., Eberhardt, W. E., Nicholson, A. G., Groome, P., Mitchell, A., and Bolejack, V. (2016). The IASLC lung cancer staging project: Proposals for revision of the TNM stage groupings in the forthcoming (eighth) edition of the TNM classification for lung cancer. *J. Thorac. Oncol.*, 11(1):39–51.

Gottschalk, B., Koehler, A., Schneider, R., Sisterson, J., and Wagner, M. (1993). Multiple coulomb scattering of 160 MeV protons. *Nucl. Instrum. Methods Phys. Res., Sect. B*, 74(4):467–490.

Gottschalk, B. and Wagner, M. (1989). Contoured scatterer for proton dose flattening. Techreport, Harvard Cyclotron Laboratory.

Graeff, C. (2014). Motion mitigation in scanned ion beam therapy through 4D-optimization. *Phys. Med.*, 30(5):570–577.

Graeff, C., Constantinescu, A., Lüchtenborg, R., Durante, M., and Bert, C. (2014). Multigating, a 4D optimized beam tracking in scanned ion beam therapy. *Technol. Cancer Res. Treat.*, 13:497–504.

Graeff, C., Durante, M., and Bert, C. (2012). Motion mitigation in intensity modulated particle therapy by internal target volumes covering range changes. *Med. Phys.*, 39(10):6004–6013.

Graeff, C., Lüchtenborg, R., Eley, J. G., Durante, M., and Bert, C. (2013). A 4D-optimization concept for scanned ion beam therapy. *Radiother. Oncol.*, 109(3):419 – 424.

Greco, C., Zelefsky, M. J., Lovelock, M., Fuks, Z., Hunt, M., Rosenzweig, K., Zatcky, J., Kim, B., and Yamada, Y. (2011). Predictors of local control after single-dose stereotactic image-guided intensity-modulated radiotherapy for extracranial metastases. *Int. J. Radiat. Oncol. Biol. Phys.*, 79(4):1151–1157.

Groezinger, S. O. (2004). *Volume conformal irradiation of moving target volumes with scanned ion beams*. PhD Thesis, TU Darmstadt.

Grutters, J. P. C., Kessels, A. G. H., Pijls-Johannesma, M., Ruysscher, D., oore, M. A. ., and Lambin, P. (2010). Comparison of the effectiveness of radiotherapy with photons, protons and carbon-ions for non-small cell lung cancer: A meta-analysis. *Radiother. Oncol.*, 95(1):32–40.

Haberer, T., Becher, W., Schardt, D., and Kraft, G. (1993). Magnetic scanning system for heavy ion therapy. *Nucl. Instrum. Meth. A*, 330:296–305.

Haettner, E., Iwase, H., and Schardt, D. (2006). Experimental fragmentation studies with 12C therapy beams. *Radiat. Prot. Dosim.*, 122(1-4):485–487.

Hall, E. J. and Giaccia, A. J. (2012). *Radiobiology for the Radiologist*. Lippincott Williams & Wilkins, seventh edition.

Hayman, J. (2007). Squamous-cell bronchial carcinoma. https://commons.wikimedia.org/w/index.php?curid=2340342, accessed 2018/09/01.

Heeg, P., Eickhoff, H., and Haberer, T. (2004). Conception of heavy ion beam therapy at Heidelberg University (HICAT). *Z. Med. Phys.*, 14(1):17–24.

Hill, D. L., Batchelor, P. G., Holden, M., and Hawkes, D. J. (2001). Medical image registration. *Phys. Med. Biol.*, 46(3):R1–45.

Hirao, Y., Ogawa, H., Yamada, S., Sato, Y., Yamada, T., Sato, K., Itano, A., Kanazawa, M., Noda, K., Kawachi, K., Endo, M., Kanai, T., Kohno, T., Sudou, M., Minohara, S., Kitagawa, A., Soga, F., Takada, E., Watanabe, S., Endo, K., Kumada, M., and Matsumoto, S. (1992). Heavy ion synchrotron for medical use – HIMAC project at NIRS, Japan. *Nucl. Phys. A*, 538:541–550.

Horcicka, M. (2011). Theorie und Numerik zur nichtlinearen Dosisoptimierung in der Schwerionentherapie. M.Sc. Thesis, TU Darmstadt.

Horcicka, M., Meyer, C., Buschbacher, A., Durante, M., and Krämer, M. (2012). Algorithms for the optimization of RBE-weighted dose in particle therapy. *Phys. Med. Biol.*, 58(2):275.

Hüfner, J. (1985). Heavy fragments produced in proton-nucleus and nucleus-nucleus collisions at relativistic energies. *Phys. Rep.*, 125(4):129–185.

ICRU (1993). Prescribing, recording and reporting photon beam therapy. ICRU report no. 50.

ICRU (1999). Prescribing, recording and reporting photon beam therapy, supplement to ICRU report 50. ICRU report no. 62.

Iyengar, P., Kavanagh, B. D., Wardak, Z., Smith, I., Ahn, C., Gerber, D. E., Dowell, J., Hughes, R., Camidge, D. R., Gaspar, L. E., Doebele, R. C., Bunn, P. A., Choy, H., and Timmerman, R. (2014). Phase II trial of stereotactic body radiation therapy combined with erlotinib for patients with limited but progressive metastatic non-small-cell lung cancer. *J. Clin. Oncol.*, 32(34):3824–3854.

Jongen, Y., Abs, M., Blondin, A., Kleeven, W., Zaremba, S., Vandeplassche, D., Aleksandrov, V., Gursky, S., Karamyshev, O., Karamysheva, G., et al. (2010). Compact superconducting cyclotron C400 for hadron therapy. *Nucl. Instrum. Methods Phys. Res., Sect. A*, 624(1):47–53.

Kaatsch, P., Spix, C., Katalinic, A., Hentschel, S., Luttmann, S., Waldeyer-Sauerland, C. S. M., Waldmann, A., Caspritza, S., Christ, M., Ernst, A., Folkerts, J., Hansmann, J., Klein, S., Kranzhöfer, K., Kunz, B., Manegold, K., Penzkofer, A., Treml, K., Weg-Remers, S., Wittenberg, K., Barnes, B., Bertz, J., Buttmann-Schweiger, N., Dahm, S., Fiebig, J., Haberland, J., Kraywinkel, K., Wienecke, A., and Wolf, U. (2017). *Krebs in Deutschland für 2013/2014*, volume 11. Robert-Koch-Institut and Gesellschaft der epidemiologischen Krebsregister in Deutschland e.V., Berlin, Germany.

Kanai, T., Kawachi, K., Matsuzawa, H., and Inada, T. (1983). Three-dimensional beam scanning for proton therapy. *Nucl. Instrum. Methods Phys. Res.*, 214(2-3):491–496.

Kang, J., Hong, B. H., An, D. H., Jung, I. S., and Kang, K. U. (2012). Magnet design of the superconducting cyclotron for carbon therapy. *IEEE Trans. Appl. Supercond.*, 22(3):4401104–4401104.

Katz, R. and Cucinotta, F. (1999). Tracks to therapy. *Radiat. Meas.*, 31(1-6):379–388.

Keall, P., Siebers, J., Joshi, S., and Mohan, R. (2004). Monte Carlo as a four-dimensional radiotherapy treatment-planning tool to account for respiratory motion. *Phys. Med. Biol.*, 49(16):3639.

Keall, P. J., Kini, V. R., Vedam, S. S., and Mohan, R. (2001). Motion adaptive X-ray therapy: a feasibility study. *Phys. Med. Biol.*, 46(1):1–10.

Kenfield, S. A., Wei, E. K., Stampfer, M. J., Rosner, B. A., and Colditz, G. A. (2008). Comparison of aspects of smoking among four histologic types of lung cancer. *Tobacco control*, pages tc–2007.

Kerst, D. W. (1940). Acceleration of electrons by magnetic induction. *Phys. Rev.*, 58:841–841.

Kilby, W., Dooley, J. R., Kuduvalli, G., Sayeh, S., and C. R. Maurer, J. (2010). The cyberknife robotic radiosurgery system in 2010. *Technol. Cancer Res. Treat.*, 9(5):433–452.

Koehler, A., Schneider, R., and Sisterson, J. (1975). Range modulators for protons and heavy ions. *Nucl. Instrum. Methods*, 131(3):437–440.

Koehler, A., Schneider, R., and Sisterson, J. (1977). Flattening of proton dose distributions for large-field radiotherapy. *Med. Phys.*, 4(4):297–301.

Kong, F.-M., Ten Haken, R. K., Schipper, M. J., Sullivan, M. A., Chen, M., Lopez, C., Kalemkerian, G. P., and Hayman, J. A. (2005). High-dose radiation improved local tumor control and overall survival in patients with inoperable/unresectable non–small-cell lung cancer: long-term results of a radiation dose escalation study. *Int. J. Radiat. Oncol. Biol. Phys.*, 63(2):324–333.

Kraft, G. (2000). Tumor therapy with heavy charged particles. *Prog. Part. Nucl. Phys.*, 45(Supplement 2):S473–S544.

Kraft, G. and Krämer, M. (1993). Linear energy transfer and track structure. In *Advances in Radidation Biology*, volume 17, chapter 1, pages 1–52. Elsevier.

Krämer, M. (1995). Calculation of heavy-ion track structure. *Nucl. Instrum. Meth. B*, 105(1-4):14–20.

Krämer, M. and Durante, M. (2010). Ion beam transport calculations and treatment plans in particle therapy. *Eur. Phys. J. D*, 60(1):195–202.

Krämer, M., Jäkel, O., Haberer, T., Kraft, G., Schardt, D., and Weber, U. (2000). Treatment planning for heavy-ion radiotherapy: physical beam model and dose optimization. *Phys. Med. Biol.*, 45(11):3299–3317.

Krämer, M. and Scholz, M. (2000). Treatment planning for heavy-ion radiotherapy: calculation and optimization of biologically effective dose. *Phys. Med. Biol.*, 45(11):3319–3330.

Krämer, M. and Scholz, M. (2006). Rapid calculation of biological effects in ion radiotherapy. *Phys. Med. Biol.*, 51(8):1959–1970.

Kumar, V., Abbas, A. K., Fausto, N., Cotran, R. S., and Robbins, S. L. (2004). *Robbins and Cotran pathologic basis of disease*. Elsevier/Saunders, 7th edition.

Langen, K. M. and Jones, D. T. L. (2001). Organ motion and its management. *Int. J. Radiat. Oncol. Biol. Phys.*, 50(1):265–278.

Liu, H. H., Balter, P., Tutt, T., Choi, B., Zhang, J., Wang, C., Chi, M., Luo, D., Pan, T., Hunjan, S., Starkschall, G., Rosen, I., Prado, K., Liao, Z., Chang, J., Komaki, R., Cox, J. D., Mohan, R., and Dong, L. (2007). Assessing respiration-induced tumor motion and internal target volume using four-dimensional computed tomography for radiotherapy of lung cancer. *Int. J. Radiat. Oncol. Biol. Phys.*, 68(2):531–540.

Liu, W., Zhang, X., Li, Y., and Mohan, R. (2012). Robust optimization of intensity modulated proton therapy. *Med. Phys.*, 39(2):1079–1091.

Llacer, J., Schmidt, J., and Tobias, C. (1990). Characterization of fragmented heavy-ion beams using a three-stage telescope detector: Measurements of 670-MeV/amu 20Ne beams. *Med. Phys.*, 17(2):151–157.

Lomax, A. (1999). Intensity modulation methods for proton radiotherapy. *Phys. Med. Biol.*, 44(1):185.

Lu, H. M., Safai, S., Schneider, R., Adams, J. A., Chen, Y. L., Wolfgang, J. A., Sharp, G. C., Brett, R. C., Kirch, D. G., Hong, T. S., Delaney, T. F., Jiang, S. B., Kooy, H. M., and Chen, G. T. Y. (2006). Respiratory-gated proton therapy treatment. In *Abstract Book PTCOG 44*.

Lujan, A. E., Larsen, E. W., Balter, J. M., and Haken, R. K. T. (1999). A method for incorporating organ motion due to breathing into 3D dose calculations. *Med. Phys.*, 26(5):715–720.

Lynch, W. (1987). Nuclear fragmentation in proton-and heavy-ion-induced reactions. *Annu. Rev. Nucl. Part. Sci.*, 37(1):493–535.

Maccabee, H. and Ritter, M. (1974). Fragmentation of high-energy oxygen-ion beams in water. *Radiat. Res.*, 60(3):409–421.

McMillan, E. M. (1945). The synchrotron—a proposed high energy particle accelerator. *Phys. Rev.*, 68:143–144.

Meschede, D. (2015). *Gerthsen Physik*. Springer-Lehrbuch. Springer Berlin Heidelberg.

Minohara, S., Kanai, T., Endo, M., Noda, K., and Kanazawa, M. (2000). Respiratory gated irradiation system for heavy-ion radiotherapy. *Int. J. Radiat. Oncol. Biol. Phys.*, 47(4):1097–1103.

Mizushima, K., Furukawa, T., Iwata, Y., Hara, Y., Saotome, N., Saraya, Y., Tansho, R., Sato, S., Fujimoto, T., Shirai, T., et al. (2017). Performance of the HIMAC beam control system using multiple-energy synchrotron operation. *Nucl. Instrum. Methods Phys. Res., Sect. B*, 406:347–351.

MMWR (2005). Achievements in public health, 1900–1999: tobacco use in the united states. *Morbidity and Mortality Weekly Report*, 48(43):986–993.

Molière, G. (1948). Theorie der Streuung schneller geladener Teilchen II, Mehrfach- und Vielfachstreuung. *Z. Naturforsch.*, 3a:78–97.

Mori, S., Lu, H., Wolfgang, J. A., Choi, N. C., and Chen, G. T. Y. (2009). Effects of interfractional anatomical changes on water-equivalent pathlength in charged-particle radiotherapy of lung cancer. *J. Radiat. Res.*, 50(6):513–519.

Nikjoo, H., O'Neill, P., Terrissol, M., and Goodhead, D. (1999). Quantitative modelling of DNA damage using Monte Carlo track structure method. *Radiat. Environ. Biophys.*, 38(1):31–38.

Paganetti, H. (2018). SP-0209: Should proton therapy clinical practice move away from a constant RBE of 1.1? *Radiother. Oncol.*, 127:S114–S115.

Paganetti, H., Jiang, H., Adams, J. A., Chen, G. T., and Rietzel, E. (2004). Monte carlo simulations with time-dependent geometries to investigate effects of organ motion with high temporal resolution. *Int. J. Radiat. Oncol. Biol. Phys.*, 60(3):942–950.

Paretzke, H. G. (1986). Physical events of heavy ion interactions with matter. *Adv. Space Res.*, 6(11):67–73.

Pedroni, E., Bacher, R., Blattmann, H., Böhringer, T., Coray, A., Lomax, A., Lin, S., Munkel, G., Scheib, S., Schneider, U., and Tourovsky, A. (1995). The 200-MeV proton therapy project at the Paul Scherrer Institute: conceptual design and practical realization. *Med. Phys.*, 22(1):37–53.

Pflugfelder, D., Wilkens, J. J., and Oelfke, U. (2008). Worst case optimization: a method to account for uncertainties in the optimization of intensity modulated proton therapy. *Phys. Med. Biol.*, 53(6):1689–1700.

Phillips, M. H., Pedroni, E., Blattmann, H., Boehringer, T., Coray, A., and Scheib, S. (1992). Effects of respiratory motion on dose uniformity with a charged particle scanning method. *Phys. Med. Biol.*, 37(1):223–233.

Puck, T. T. and Marcus, P. I. (1956). Action of X-rays on mammalian cells. *J. Exp. Med.*, 103(5):653–666.

Ramalingam, S. and Belani, C. (2008). Systemic chemotherapy for advanced non-small cell lung cancer: Recent advances and future directions. *The Oncologist*, 13(suppl 1):5–13.

RaySearch (2013). Raysearch licences technology from GSI. www.raysearchlabs.com/media/press/?year=2013&cisionid=1301095, accessed: 2018/08/23.

Renz-Polster, H. and Krautzig, S. (2008). *Basislehrbuch Innere Medizin*, chapter 5 - Lung, pages 424–531. Urban & Fischer, 4th edition.

Richter, D. (2012). *Treatment planning for tumors with residual motion in scanned ion beam therapys*. PhD thesis, TU Darmstadt.

Richter, D., Schwarzkopf, A., Trautmann, J., Krämer, M., Durante, M., Jäkel, O., and Bert, C. (2013). Upgrade and benchmarking of a 4D treatment planning system for scanned ion beam therapy. *Med. Phys.*, 40(5):051722.

Rietzel, E. and Bert, C. (2010). Respiratory motion management in particle therapy. *Med. Phys.*, 37(2):449–460.

Rietzel, E. and Chen, G. T. Y. (2006). Deformable registration of 4D computed tomography data. *Med. Phys.*, 33(11):4423–4430.

Röntgen, W. C. (1898). Über eine neue Art von Strahlen. *Ann. Phys.*, 300(1):1–11.

Rosenzweig, K. E., Fox, J. L., Yorke, E., Amols, H., Jackson, A., Rusch, V., Kris, M. G., Ling, C. C., and Leibel, S. A. (2005). Results of a phase I dose-escalation study using three-dimensional conformal radiotherapy in the treatment of inoperable nonsmall cell lung carcinoma. *Cancer*, 103(10):2118–2127.

Saito, N., Bert, C., Chaudhri, N., Durante, M., Gemmel, A., Lüchtenborg, R., Schardt, D., and Rietzel, E. (2009). Technical status of the real-time beam tracking system. Report.

Schall, I., Münzenberg, G., Kraft, G., Schwab, W., Schardt, D., Scheidenberger, C., Magel, A., Irnich, H., Nickel, F., Mohar, M., et al. (1996). Charge-changing nuclear reactions of relativistic light-ion beams ($5 \leq z \leq 10$) passing through thick absorbers. *Nucl. Instr. Meth. Phys. Res. B*, 117:221–234.

Schardt, D., Elsaesser, T., and Schulz-Ertner, D. (2010). Heavy-ion tumor therapy: Physical and radiobiological benefits. *Rev. Mod. Phys.*, 82(1):383.

Schimmerling, W., Miller, J., Wong, M., Rapkin, M., Howard, J., Spieler, H. G., and Jarret, B. V. (1989). The fragmentation of 670A MeV Neon-20 as a function of depth in water: I. experiment. *Radiat. Res.*, 120(1):36–71.

Scholz, M., Kellerer, A., Kraft-Weyrather, W., and Kraft, G. (1997). Computation of cell survival in heavy ion beams for therapy. *Radiat. Environ. Biophys.*, 36(1):59–66.

Schömers, C., Feldmeier, E., Haberer, T., Naumann, J., Panse, R., Peters, A., et al. (2011). Implementation of an intensity feedback loop for an ion therapy synchtrotron. In *2nd International Conference, IPAC*, pages 4–9.

Seco, J., Robertson, D., Trofimov, A., and Paganetti, H. (2009). Breathing interplay effects during proton beam scanning: simulation and statistical analysis. *Phys. Med. Biol.*, 54(14):N283.

Seppenwoolde, Y., Shirato, H., Kitamura, K., Shimizu, S., Lebesque, J. V., and Miyasaka, K. (2002). Precise and real-time measurement of 3D tumor motion in lung due to breathing and heartbeat, measured during radiotherapy. *Int. J. Radiat. Oncol. Biol. Phys.*, 53(4):822–834.

Serber, R. (1947). Nuclear reactions at high energies. *Phys. Rev.*, 72:1114–1115.

Sgantzos, M., Tsoucalas, G., Laios, K., and Androutsos, G. (2014). The physician who first applied radiotherapy, Victor Despeignes, on 1896. *Hell. J. Nucl. Med.*, 17(1):45–46.

Shirato, H., Seppenwoolde, Y., Kitamura, K., Onimura, R., and Shimizu, S. (2004). Intrafractional tumor motion: Lung and liver. *Semin. Radiat. Oncol.*, 14(1):10–18.

Sonke, J. J., Lebesque, J., and van, H. M. (2008). Variability of four-dimensional computed tomography patient models. *Int. J. Radiat. Oncol. Biol. Phys.*, 70(2):590–598.

Tobias, C. and Todd, P. (1967). Heavy charged particles in cancer therapy, radiobiology and radiotherapy. *Nat. Cancer Inst. Monogr.*, 24:1–21.

Tsunashima, Y., Vedam, S., Dong, L., Umezawa, M., Sakae, T., Bues, M., Balter, P., Smith, A., and Mohan, R. (2008). Efficiency of respiratory-gated delivery of synchrotron-based pulsed proton irradiation. *Phys. Med. Biol.*, 53(7):1947–1959.

Underwood, T., Grassberger, C., Bass, R., Jimenez, R., Meyersohn, N., Yeap, B., MacDonald, S., and Paganetti, H. (2017). OC-0245: Clinical evidence that end-of-range proton RBE exceeds 1.1: lung density changes following chest RT. *Radiother. Oncol.*, 123:S123–S124.

Unkelbach, J., Bortfeld, T., Martin, B. C., and Soukup, M. (2009). Reducing the sensitivity of IMPT treatment plans to setup errors and range uncertainties via probabilistic treatment planning. *Med. Phys.*, 36(1):149–163. 074812MPH[PII].

Unkelbach, J., Chan, T. C. Y., and Bortfeld, T. (2007). Accounting for range uncertainties in the optimization of intensity modulated proton therapy. *Phys. Med. Biol.*, 52(10):2755–2774.

Varma, M. N., Baum, J. W., and Kuehner, A. V. (1977). Radial dose, LET and W for 160 ions in N2 and tissue-equivalent gases. *Radiat. Res.*, 70(3):511–518.

Warner, K. and Goldenhar, L. (1989). The cigarette advertising broadcast ban and magazine coverage of smoking and health. *J. Public Health Policy*, 10(1):32–42.

Weber, U., Becher, W., and Kraft, G. (2000). Depth scanning for a conformal ion beam treatment of deep seated tumours. *Phys. Med. Biol.*, 45(12):3627–3641.

Weber, U. and Kraft, G. (1999). Design and construction of a ripple filter for a smoothed depth dose distribution in conformal particle therapy. *Phys. Med. Biol.*, 44(11):2765–2775.

Weber, U. and Kraft, G. (2009). Comparison of carbon ions versus protons. *The Cancer Journal*, 15(4):325–332.

Wilson, R. R. (1946). Radiological use of fast protons. *Radiology*, 47:487–491.

Lebenslauf

Persönliche Daten

Name	Moritz Ernst Wolf
Geburtstag	11.10.1986
Geburtsort	Dieburg, Deutschland

Universitäre Ausbildung

07/2015 – 12/2018	**Technische Universität Darmstadt** Promotion in Kooperation mit dem GSI Helmholtzzentrum für Schwerionenforschung
10/2011 – 05/2014	**Technische Universität Darmstadt** Master of Science in Physik Titel der Masterarbeit: *“Studies on nonlinear microscopy involving chromatic depth-resolved imaging”*
09/2007 – 09/2011	**Technische Universität Darmstadt** Bachelor of Science in Physik Titel der Bachelorarbeit: *“Development of a calibration- and adjustment-program for acousto-optical modulators”*

Militär-Ersatzdienst

08/2006 – 05/2007	**Johanniter-Unfall-Hilfe, Dieburg** Assistent der Fahrdienstleitung

Schulische Ausbildung

08/1999 – 07/2006	**Max-Planck-Gymnasium, Groß-Umstadt**
09/1993 – 09/1999	**Otzberg-Schule, Lengfeld**

Nebentätigkeiten

04/2009 – 03/2012	**Technische Universität Darmstadt** Leiter von Übungsgruppen für Experimentalphysik, Physik für Chemiker und Biologen und Naturwissenschaften für Ingenieure

Pulications and conference contributions related to this work

Pulications

Wolf, M., Anderle, K., Durante, M., and Graeff, C. (2019). Robust 4D particle therapy planning for multiple targets in lung cancer. *Phys. Med. Biol.* (in preparation)

Wolf, M., Hild, S., Anderle, K., Prall, M., Durante, M., and Graeff, C. (2019). Random voxel subsampling enabling large scale particle therapy optimization. *Phys. Med.* (in preparation)

Conference contributions

05/2018 **Oral presentation at PTCOG 57, Cincinnati, USA**
Title: *"Robust treatment planning with 4D intensity modulated particle therapy for multiple targets in stage IV non-small cell lung cancer"*

10/2018 **Oral and poster presentation at GIERSCH International Symposium, Frankfurt, Germany**
Title: *"Nonlinear robust optimization methods for 4D treatment planning in carbon ion therapy"*

09/2017 **Poster presentation at DGMP, Dresden, Germany**
Title: *"Nonlinear robust optimization methods for (4D) treatment planning in carbon ion therapy"*

05/2017 **Oral presentation at PTCOG 56, Yokohama, Japan**
Title: *"Nonlinear robust optimization methods for 4D treatment planning in carbon ion therapy"*

11/2016 **Poster presentation at 4D Workshop, Groningen, Netherlands**
Title: *"Nonlinear robust optimization methods for (4D) treatment planning in carbon ion therapy"*

Acknowledgements

To begin with, I would like to thank all the people who contributed to the success of this work. A special thank goes to Marco Durante for raising my interest in this topic with his exciting lecture about radiation biophysics and enabling my position as a doctoral student at GSI. Further on, I want to thank Christian Graeff for the warm welcoming in the "motion group" and the general supervision of my thesis. Being such a smart and knowledgeable programmer, he was always having a good advice. I really liked the given freedom to steer the direction of my research.

I want to thank Sebastian Hild for bearing all my questions about all theses specific quirks of the TRiP4D code during the time, when I started to getting into the subject and the support to not get lost in all that multi threading. In addition, I want to thank Sebastian for all the fun climbing sessions we had in our leisure time. I want to thank Kristjan Anderle for providing me all the data of the patient study he started during his PhD thesis. With patience you answered all my questions and I always could seek advice about treatment planning and image registration. Your support helped me to not get lost in this jungle of patients, plans and CT images. I want to tank Anna Eichhorn for proof reading my thesis and for being such a kind coworker and office mate. Fortunately to me, you were one of the last experts on the LMDout tool, after Sebastian did leave GSI. I want to thank Michelle Lis for proof reading and gratuitously improving my English without even noticing during numerous good conversations. I really enjoyed sharing the office with you. Further on, I want to thank Christoph Schuy for giving input from outside the box and for his huge knowledge about the biophysics at GSI in general (somehow, he seems to be a walking encyclopedia). Since doing sports helps to keep the mind focused, I also want to thank Christoph for being a motivating climbing partner.

A very special thanks goes to my wife Stephie for bearing all my strange behaviors in the last months and for always supporting me without questioning anything, not even strange working hours. Without you, I barely would have succeeded in writing this thesis. I want to thank my parents Norbert and Beate, who encouraged me in studying physics and whoe provided me with lots of support during the time of my studies. Loosing my dad to cancer in 2013 was tragically one of the reasons, why I was looking for a PhD topic in cancer research and why I am now, where I am. Last but not least, I want to thank Ingrid and Gerhard Theis for patiently answering all the curious questions which I posed as a child, and thus raising my interest in science and music.

Erklärung zur Dissertation

Hiermit versichere ich, die vorliegende Dissertation ohne Hilfe Dritter nur mit den angegebenen Quellen und Hilfsmitteln angefertigt zu haben. Alle Stellen, die aus Quellen entnommen wurden, sind als solche kenntlich gemacht. Diese Arbeit hat in gleicher oder ähnlicher Form noch keiner Prüfungsbehörde vorgelegen.

Darmstadt, den 13. November 2018

(Moritz Wolf)